Design, Fabrication, and Characterization of a Compact Deep Reactive Ion Etching System for MEMS Processing

by

Parker Andrew Gould

B.Eng. Electrical Engineering, Vanderbilt University, 2011
M.Phil. Micro- and Nanotechnology Enterprise, University of Cambridge, 2012

AND

Mitchell David Hsing

B.S. Electrical Engineering, University of California Irvine, 2012
B.S. Physics, University of California Irvine, 2012

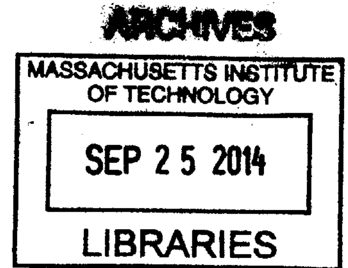

Submitted to the Department of Electrical Engineering and Computer Science in Partial Fulfillment of the Requirements for the Degree of

MASTER OF SCIENCE IN ELECTRICAL ENGINEERING
AT THE
MASSACHUSETTS INSTITUTE OF TECHNOLOGY

September 2014

© Massachusetts Institute of Technology 2014. All rights reserved.

Signature of Authors.. Signature redacted
Department of Electrical Engineering and Computer Science
August 29, 2014

Certified by............................... Signature redacted
Martin A. Schmidt
Professor of Electrical Engineering
Thesis Supervisor

Accepted by............................... Signature redacted
Leslie A. Kolodziejski
Chairman, Committee for Graduate Students

Design, Fabrication, and Characterization of a Compact Deep Reactive Ion Etching System for MEMS Processing

by

Parker Andrew Gould

AND

Mitchell David Hsing

Submitted to the Department of Electrical Engineering and Computer Science
on August 29, 2014 in Partial Fulfillment of the
Requirements for the Degree of Master of Science in
Electrical Engineering

ABSTRACT

A general rule of thumb for new semiconductor fabrication facilities (Fabs) is that revenues from the first year of production must match the capital cost of building the fab itself. With modern Fabs routinely exceeding $1 billion to build, this rule serves as a significant barrier to entry for groups seeking to commercialize new semiconductor devices aimed at smaller market segments which require a dedicated process. To eliminate this cost barrier we are working to create a small-scale production suite of tools that will processes small (~1") substrates and cost less than $1 million. By shrinking the size of the substrate, substantial savings can be realized in material usage, energy consumption, and, most importantly, capital costs.

In this thesis, we present the development of the first tool in this suite of small substrate processing equipment, a deep reactive ion etcher (DRIE). DRIE tools are used to create highly anisotropic, high aspect-ratio trenches in silicon—a crucial element in the production of many microelectromechanical systems (MEMS) devices. We are targeting the Bosch Process method of DRIE, which is a time multiplexed process that rapidly alternates between an SF_6-based reactive ion etching (RIE) step that isotropically etches silicon and a C_4F_8-based plasma-enhanced chemical vapor deposition (PECVD) step that passivates the sidewalls of the etched features. The rapid alternation between the RIE and PECVD steps allows highly anisotropic features to be etched in silicon. The DRIE system developed in this thesis is roughly the size of a microwave oven and costs just a fraction of commercial etching systems. The test results presented herein characterize the stability and operating limits of the vacuum and plasma generation systems, and demonstrate the system's raw etching capability using a mix of SF_6 and O_2 process gases. Etch rates exceeding 4 μm/min with control of the etched profile are reported, with models fitted to the data indicating increased capabilities with optimized process conditions.

Thesis Supervisor: Martin A. Schmidt
Title: Professor of Electrical Engineering

Design, Fabrication, and Characterization of a Compact Deep Reactive Ion Etching System for MEMS Processing

by

Mitchell David Hsing

B.S. Electrical Engineering, University of California Irvine, 2012
B.S. Physics, University of California Irvine, 2012

AND

Parker Andrew Gould

B.Eng. Electrical Engineering, Vanderbilt University, 2011
M.Phil. Micro- and Nanotechnology Enterprise, University of Cambridge, 2012

Submitted to the Department of Electrical Engineering and Computer Science
in Partial Fulfillment of the Requirements for the Degree of

MASTER OF SCIENCE IN ELECTRICAL ENGINEERING
AT THE
MASSACHUSETTS INSTITUTE OF TECHNOLOGY

September 2014

© Massachusetts Institute of Technology 2014. All rights reserved.

Signature of Authors............Signature redacted..........
Department of Electrical Engineering and Computer Science
August 29, 2014

Certified by............Signature redacted
Martin A. Schmidt
Professor of Electrical Engineering
Thesis Supervisor

Accepted by............Signature redacted.........
Leslie A. Kolodziejski
Chairman, Committee for Graduate Students

Design, Fabrication, and Characterization of a Compact Deep Reactive Ion Etching System for MEMS Processing

by

Mitchell David Hsing

AND

Parker Andrew Gould

Submitted to the Department of Electrical Engineering and Computer Science
on August 29, 2014 in Partial Fulfillment of the
Requirements for the Degree of Master of Science in
Electrical Engineering

ABSTRACT

A general rule of thumb for new semiconductor fabrication facilities (Fabs) is that revenues from the first year of production must match the capital cost of building the fab itself. With modern Fabs routinely exceeding $1 billion to build, this rule serves as a significant barrier to entry for groups seeking to commercialize new semiconductor devices aimed at smaller market segments which require a dedicated process. To eliminate this cost barrier we are working to create a small-scale production suite of tools that will processes small (~1") substrates and cost less than $1 million. By shrinking the size of the substrate, substantial savings can be realized in material usage, energy consumption, and, most importantly, capital costs.

In this thesis, we present the development of the first tool in this suite of small substrate processing equipment, a deep reactive ion etcher (DRIE). DRIE tools are used to create highly anisotropic, high aspect-ratio trenches in silicon—a crucial element in the production of many microelectromechanical systems (MEMS) devices. We are targeting the Bosch Process method of DRIE, which is a time multiplexed process that rapidly alternates between an SF_6-based reactive ion etching (RIE) step that isotropically etches silicon and a C_4F_8-based plasma-enhanced chemical vapor deposition (PECVD) step that passivates the sidewalls of the etched features. The rapid alternation between the RIE and PECVD steps allows highly anisotropic features to be etched in silicon. The DRIE system developed in this thesis is roughly the size of a microwave oven and costs just a fraction of commercial etching systems. The test results presented herein characterize the stability and operating limits of the vacuum and plasma generation systems, and demonstrate the system's raw etching capability using a mix of SF_6 and O_2 process gases. Etch rates exceeding 4 μm/min with control of the etched profile are reported, with models fitted to the data indicating increased capabilities with optimized process conditions.

Thesis Supervisor: Martin A. Schmidt
Title: Professor of Electrical Engineering

Table of Contents

Table of Figures i

Acknowledgements v

Foreword vii

List of Abbreviations ix

Chapter 1: The 1" Fab Platform 1

1.1 The Problem 1

1.2 The Proposed Solution 3

1.3 The Vision for a 1" Fab Platform 4

Chapter 2: Overview of Plasma Etching 7

2.1 Common Dry Etching Characteristics and Terms 7

2.1.1 Etch Profiles 7

2.1.2 Mask Erosion and Etch Selectivity 8

2.1.3 Etch Uniformity 9

2.2 Plasma Basics 10

2.3 Plasma Generation and Etching Techniques 12

2.3.1 Capacitively Coupled Plasmas 13

2.3.2 Inductively Coupled Plasmas 15

2.4 Etching Mechanics and Chemistry 18

2.4.1 Halogen-based silicon etching 18

2.4.2 Silicon etching with SF_6 19

2.4.3 SF_6+O_2 Etching 21

2.4.4 Bosch Process Etching 22

Chapter 3: Design of the 1" Fab DRIE 25

3.1 Design Overview 25

3.1.1 System Basics 26

3.1.2 Chamber Assembly Design 31

3.1.3 Chuck Design 34

3.1.4 RF Components 38

3.1.5 Gas Distribution System 40

3.1.6 1" Fab DRIE Control System 47

3.2 Component Selection and Scalability 55

3.2.1 RF Generators 55

3.2.2 Matching Networks 58

3.2.3 Vacuum Pumps 62

3.2.4 Mass Flow Controllers 67

Chapter 4: Characterization of the 1" Fab DRIE 71

4.1 Vacuum and Plasma Characterization 71

4.1.1 Pump Rate and Leak Rate 71

4.1.2 Plasma Characterization - Langmuir Probe 73

4.2 Experimental Design 79

4.2.1 Response Surface Methodology 80

4.2.2 Experimental Protocol 85

4.2.3 Sample Analysis Procedures 87

4.2.4 Test Wafer Design 91

4.3 SF_6 Etching Characterization 93

4.3.1 RSM Data Analysis 93

4.3.2 Vertical Etch Rate 94

4.3.3 Spatial Uniformity of Etch Rate 100

4.3.4 Etch Profile 104

4.3.5 Center Point Repeatability 109

Chapter 5: Conclusions and Future Directions 113

5.1 Summary of Performance 113

5.2 Follow Up Tests 116

5.3 Future Improvements 117

5.3.1 Conductance Control Valve 117

5.3.2 Turbo Pump 118

5.3.3 Helium Backside Wafer Cooling 119

5.3.4 Process Monitoring - Substrate Temperature and Bias Voltage 120

5.4 Looking Forward 121

References 123

Appendix A: 1" Fab DRIE Bill of Materials A-1

Appendix B: Gas Flow Equations A-5

Appendix C: 1" Fab DRIE Operation Protocol A-9

Appendix D: Control System Circuit Diagram A-11

Appendix E: Langmuir Probe Theory and Analysis A-13

Appendix F: Full RSM Data Set A-17

Table of Figures

Figure 1.1 5

Figure 2.1 8

Figure 2.2 10

Figure 2.3 11

Figure 2.4 13

Figure 2.5 14

Figure 2.6 15

Figure 2.7 16

Figure 2.8 17

Figure 2.9 18

Figure 2.10 19

Figure 2.11 24

Figure 3.1 26

Figure 3.2 27

Figure 3.3 28

Figure 3.4 30

Figure 3.5 31

Figure 3.6 33

Figure 3.7 34

Figure 3.8 35

Figure 3.9 36

Figure 3.10 37

Figure 3.11 39

Figure 3.12 40
Figure 3.13 42
Figure 3.14 43
Figure 3.15 46
Figure 3.16 48
Figure 3.17 50
Figure 3.18 54
Figure 3.19 59
Figure 3.20 60
Figure 3.21 64
Figure 3.22 65
Figure 4.1 72
Figure 4.2 73
Figure 4.3 75
Figure 4.4 77
Figure 4.5 78
Figure 4.6 79
Figure 4.7 81
Figure 4.8 83
Figure 4.9 88
Figure 4.10 88
Figure 4.11 90
Figure 4.12 92
Figure 4.13 95
Figure 4.14 96
Figure 4.15 97

Figure 4.16 98
Figure 4.17 99
Figure 4.18 101
Figure 4.19 103
Figure 4.20 105
Figure 4.21 106
Figure 4.22 107
Figure 4.23 109
Figure 4.24 110
Figure 4.25 111
Figure 4.26 112
Figure 5.1 119
Figure 5.2 120

Acknowledgements

This thesis would not have been possible without the support of many people. First, we would both like to thank our families for their support and continuing pledge to do anything to help short of actually writing the text included here. Second, we would like to thank Prof. Karen K. Gleason of Chemical Engineering, who has shared her wisdom and resources with us over the past two years, helping jumpstart the 1" Fab project. Third, we would like to thank all of the MTL staff, in particular Bob Bicchieri, Kurt Broderick, Donal Jamieson, Eric Lim, Gary Riggott, and Dennis Ward, for putting up with our questions and helping us troubleshoot system problems. Fourth, we would not be nearly as far along as we are today without Mark Belanger of the Edgerton Student Shop, who routinely let us exceed our three questions per day quota, and made the construction of the 1" Fab DRIE a much simpler process. Lastly, we would like to thank the other members of the Schmidt Research Group, Eric Newton, Eric Lam, Hanqing Li, and Prof. Martin A. Schmidt, who have listened to our problems and successes each week, helping fix the former and deserving a good deal of credit for the latter.

Foreword

The following thesis details the design, construction, and initial testing of an inexpensive deep reactive ion etching system for small substrates. This work was conducted jointly between Parker Gould and Mitchell Hsing. The following list delineates which tasks were performed jointly and which tasks were performed independently.

Parker Gould:

- Gas distribution system
- Automated process controller design - Etch Recipe and Controller (ERAC) software
- Response surface experiment design

Mitchell Hsing:

- Plasma generation system design
- Substrate chuck assembly design
- Plasma characterization experiment design and analysis

Jointly Performed Work:

- Structural/Mechanical design
- Component selection
- Test sample fabrication
- Response surface model data analysis
- Cost model analysis
- System troubleshooting

List of Abbreviations

Facility Abbreviations:

CMSE: Center for Material Science and Engineering

EML: Exploratory Materials Laboratory

EMSEF: Electron Microscopy Shared Equipment Facility

MTL: Microsystems Technology Lab

Technical Abbreviations:

ANOVA: Analysis of Variance

ANSI: American National Standards Institute

APDM: Average Percent Deviation from the Mean

BP: Base Power

CAGR: Compound Annual Growth Rate

CCC: Central Composite Circumscribed

CCP: Capacitively Coupled Plasma

CF Flange: Con Flat Flange

CF: Con Flat

CMOS: Complementary Metal Oxide Semiconductor

CNC: Computer Numerical Control

CP: Center Point

DOE: Design of Experiments

DPST: Double-Poles Single-Throw

DRAM: Dynamic Random Access Memory

DRIE: Deep Reactive Ion Etching

DRO: Digital Read Out

EMO: Emergency Off

ERAC: Etch Recipe and Controller

GUI: Graphical User Interface

I/O: In/Out

IC: Integrated Circuit

ICP: Inductively Coupled Plasma

ID: Inner Diameter

IDE: Integrated Design Environment
KF: Kwik Flange
LFE: Laminar Flow Element
LP: Langmuir Probe
LPVCD: Low Pressure Chemical Vapor Deposition
MEMS: Micro Electro Mechanical Systems
MFC: Mass Flow Controller
MFP: Mean Free Path
NPT: National Pipe Taper
OD: Outer Diameter
PECVD: Plasma Enhanced Chemical Vapor Deposition
PEEK: Polyetheretherketone
PFPE: Perfluoropolyether
RF: Radio Frequency
RIE: Reactive Ion Etching
RSM: Response Surface Model
SEM: Scanning Electron Microscope
SO: Standard Order
SOP: Standard Operating Procedure
TSV: Through Silicon Via
VLERR: Vertical Lateral Etch Rate Ratio

Chapter 1: The 1" Fab Platform

Year-over-year market growth has been the norm in the semiconductor industry for the past several decades. In recent years however, the fastest growing markets segments (in terms of compound annual growth rate (CAGR)) have not come from the traditional "Moore's Law"-driven CMOS, but instead from areas like MEMS-based sensors and optoelectronics [1,2] due to the rising demand for increasingly sensor-rich consumer and mobile electronic devices. Research and development efforts in these areas are also thriving. However, the equipment used to fabricate these new classes of devices still remains a major financial and technical hurdle for many small businesses and academic institutions. To address this problem, we have proposed the development of a novel, inexpensive fabrication platform for processing these innovative new semiconductor devices. In this thesis, the first piece of equipment within this platform, a deep reactive ion etcher (DRIE), is presented and its SF_6-based etching capabilities are characterized.

1.1 The Problem

Today, the primary obstacle facing groups wishing to commercialize a new product based on integrated circuit (IC) manufacturing methods is access to fabrication. A general rule of thumb for new semiconductor fabrication facilities (fabs) is that revenues from the first year of production must match the capital cost of building the fab itself. This, of course, depends on depreciation and product life cycles but is a useful role of thumb. With modern fabs routinely exceeding 1 billion USD to build and equip [3], this rule serves as a substantial barrier to entry, especially for those groups whose devices target smaller market segments or those which require a unique process incompatible with the standardized CMOS flows used by large foundries.

In response to this problem, several specialty foundries have arisen to offer more flexible and low volume processing arrangements. To maintain profitability however, these foundries can still only offer a small

number of standardized process flows, which places cumbersome constraints on the customer, as they must adapt their designs to meet the fab's design rules. The nominal diversity afforded by these specialty foundries makes some devices with smaller market sizes economically viable, but many more devices (particularly in the MEMS sector) require dedicated, fully customizable process flows. Additionally, these foundries can still only offer customers a few device turns per year, which limits their usefulness in the prototyping phase and discourages high-risk, high-reward designs.

When time constraints or a non-standard process preclude a device from using a commercial fab, only a few fabrication alternatives exist. One option is a partnership or contract with an academic institution or government laboratory. Such an agreement offers access to generally well-maintained and semi-modern tools, but the shared nature of the facilities often presents issues in process scheduling and production planning, and also creates the potential for cross-contamination and process variations due to the changing loads put on the equipment by multiple, different end users.

If device or time requirements rule out foundries and academic partnerships are not possible, assembling an in-house fabrication setup with used equipment is the only remaining option. With the vast majority of large scale fabs being outfitted with semiconductor equipment for processing the latest CMOS substrate sizes (300 mm, and now 450 nm), the used equipment market consists primarily of 100, 150, and 200 mm tools. 200 mm equipment offers the most modern processing capabilities, but is also the most expensive, making it the most difficult to recoup the capital costs. Devices with small market sizes may only need to process a few 200 mm wafers to satisfy a year's worth of demand, which means the equipment's utilization rate is very low, and the effective cost of processing is very high. This presents a major risk for the volatile world of small and early-stage businesses. Increased affordability can be found by looking to purchase older 100 and 150 mm equipment, but this equipment's advanced age greatly increases its likelihood of being beyond end-of-life support from the original equipment manufacturer. For these end-of-life tools, sourcing parts and maintenance services can become increasingly difficult and costly.

With the process limitations and delays inherent to foundries and multi-user facilities, and the uncertainties and potentially high costs associated with the used equipment market, there simply does not exist a reliable, cost-effective solution for the production of many novel semiconductor devices.

1.2 The Proposed Solution

To address this shortcoming in the semiconductor fabrication market, we are advocating a fundamental 'disruption' in the way in which products that require IC manufacturing methods are developed and ultimately produced. Rather than rely on the existing infrastructure of semiconductor fabrication facilities and equipment markets, which succeed due to the demand for high volume production of primarily silicon CMOS devices for mature market segments, we are developing an equipment platform for manufacturing semiconductor products that is three orders of magnitude less expensive than a current state-of-the-art fabrication facility (i.e. we aim to cut the capital costs from $1B to $1M). Our proposed platform fits classically with the theory of disruptive innovations developed by Clayton Christensen [4].

According to Christensen, disruptive innovations take the form of new solutions (e.g. products, techniques, processes, business models) that radically alter the time, characteristics, or cost of production within a market (even if *initially* at a slightly lower performance level). Our innovation is to flip the traditional convention of processing larger and larger wafers (the 300 mm and 450 mm nodes of today) and instead drive the development of fabrication tools and standards on small substrates, beginning with 1" (25.4 mm) wafers. This 1" substrate platform, known colloquially as the 1" Fab, bridges the gap outlined above for those looking to fabricate non-traditional semiconductor devices. The simple reduction of substrate size has a profound impact on the cost of the manufacturing tools, and enables some novel new fabrication methods that are simply not feasible at larger scales. Access to inexpensive fabrication equipment and infrastructure will help expedite the development process for new micro/nano devices by reducing or eliminating the "turn time" waiting period associated with foundries and allowing higher levels of control over the processing sequence. In a production context, the availability of low-cost

fabrication tools will help bridge the gap between development and full scale production by providing a low-volume manufacturing solution as market sizes expand. In addition, the increased availability of these inexpensive fabrication resources will make experimentation, prototyping, and production at the micro/nano scale possible to many more people, providing a conduit to innovation in much the same way that breakthrough products like economical 3D printers have done for macro-scale fabrication in recent years.

An inexpensive toolset for small substrates can also provide significant advantages to the non-silicon device community, where substrate sizes are generally smaller to begin with. These non-silicon materials typically encounter many restrictions in primarily-silicon fabs due to cross-contamination and fouling concerns.

1.3 The Vision for a 1" Fab Platform

We envision the 1" Fab as containing a localized, stand-alone set of tools capable of producing most semiconductor devices. The basic set of tools needed includes a deep reactive ion etcher (DRIE), a plasma-enhanced chemical vapor deposition tool (PECVD), a high temperature processing tool (for oxidation, annealing, and low-pressure chemical vapor deposition (LPCVD) processes), a wet etch/wet process station, a maskless lithography system[1], a wafer bonder, a sputtering tool, and a characterization station (to include both visual inspection and surface profiling capabilities). Just this set of tools includes nearly everything needed[2] to make many common MEMS devices, like the pressure sensor outlined in the following section. The full set of tools could be contained on a single platform (with an estimated size of 40 ft^2 (4 feet wide × 10 wide)), which would then be housed within a large laminar flow hood to provide a cleanroom-like environment for processing. This localization of tools drastically reduces the cost of

[1] The recent advent of maskless lithography systems is one of the major enabling technologies that makes the 1" Fab platform viable. Eliminating the need for photomasks greatly reduces the time between development cycles, and the small area of the substrates used in a 1" Fab makes the speed of maskless systems (their biggest disadvantage in a production sense) much less of a factor.

[2] An ion implantation tool would be needed for most devices, but for most processes excluding large scale production, ion implantation has become a highly efficient third-party service that would be difficult to replicate on a 1" Fab scale.

maintaining a clean processing environment and also allows tools to share certain common peripherals like roughing pumps, which further reduces costs. A scale rendering of the proposed toolset is shown in **Figure 1.1**.

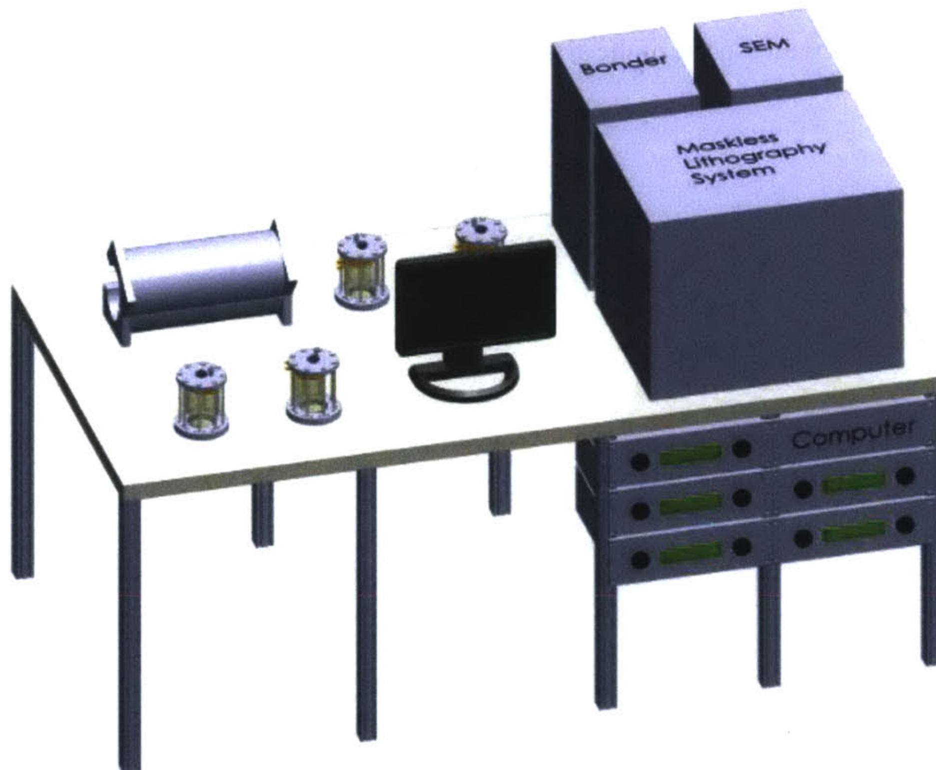

Figure 1.1: The components of a basic 1" Fab platform, arranged on a 4 foot wide × 10 foot long table.

Creating this set of tools is no small challenge, and to demonstrate the feasibility of achieving a robust and reliable 1" Fab platform, this thesis targets the most complex and arguably the most important tool for MEMS manufacturing, the deep reactive ion etcher (DRIE). DRIE tools are used to create highly anisotropic, high aspect-ratio trenches in silicon—a crucial element in many MEMS processes and an increasingly important process in CMOS processes like DRAM. The specific type of DRIE being targeted is the heralded Bosch Process, which uses a carefully constructed sequence of etching and deposition steps to achieve high aspect-ratio features. The mechanics of the Bosch Process, as well as the mechanics of two of its more basic components, plasma generation and reactive ion etching are described in more detail in **Chapter 2**. **Chapter 3** describes the design criteria and design choices made for the 1"

Fab DRIE and **Chapter 4** presents and analyzes the initial characterization tests of the etching performance of the system. **Chapter 5** provides conclusions based on the observations made during the design and testing of the etcher, outlines areas for future testing, and provides several design revisions to increase the performance and reliability of the system. Several appendices also follow the text with additional details on certain aspects of the system.

Chapter 2: Overview of Plasma Etching

Plasma-based silicon etching (often known as "dry" etching) is a staple of modern semiconductor processing. Plasma etching techniques are crucial in realizing MEMS devices and are also becoming increasingly important in CMOS fabrication for devices like 3D memory stacks which utilize through silicon vias (TSVs) to make electrical connections to multiple wafers. Nearly all plasma etching systems rely on the same basic principles; process gas is introduced into an evacuated chamber and a plasma of that gas is generated. This plasma creates ions and radicals which act via chemical or physical mechanisms to remove material from a substrate. Many different variations on this basic sequence have been developed and optimized to achieve desirable etch speeds and etch profiles. This chapter will provide a brief overview on etching terminology, a look at the physics of plasma generation, a summary of some of the most common etch procedures, and a more detailed look at silicon etch processes using fluorine-based process gases, which are used by the 1" Fab DRIE.

2.1 Common Dry Etching Characteristics and Terms

Like many technical fields, dry etching has its own set of terminology that is widely used when discussing the properties of etched samples and whole etching systems. Several of the most common terms from this lexicon are defined and explained in the following section.

2.1.1 Etch Profiles

The profile of an etch refers to the cross-sectional geometry of that etch, including the relative lateral and vertical components, as well as any curvature for both the sidewalls and the base. For most applications, the ideal etch is one that produces a cavity with sidewalls extending vertically downward from the edges of the masked region and a depth that is perfectly consistent across the entire substrate (a representation is shown in **Figure 2.1a**). This ideal etch profile however is very difficult to achieve. In practice, there are two primary categories for etch profiles: isotropic and anisotropic. Isotropic etches, like the one seen in

Figure 2.1b, have curved sidewalls that extend under the mask (known as "mask undercut") and may also show some curvature in the base region. As the name implies, the profile of an isotropic etch comes about when the substrate is etched in all directions from the exposed profile. The directional etch depths need not be equal for a profile to be classified as isotropic, but they are generally of the same order of magnitude. Anisotropic profiles (like the one shown in **Figure 2.1c**), on the other hand, exhibit significantly more etching in the vertical direction that they do in the horizontal, or lateral direction. An anisotropic profile can still exhibit some amount of the mask undercut, but generally this undercut is minimal in comparison to the ultimate etch depth. The ideal etch profile of **Figure 2.1a** would be classified as an anisotropic etch, as would the profiles created by deep-reactive ion etching techniques like Bosch Process etching (**Section 2.4.4**).

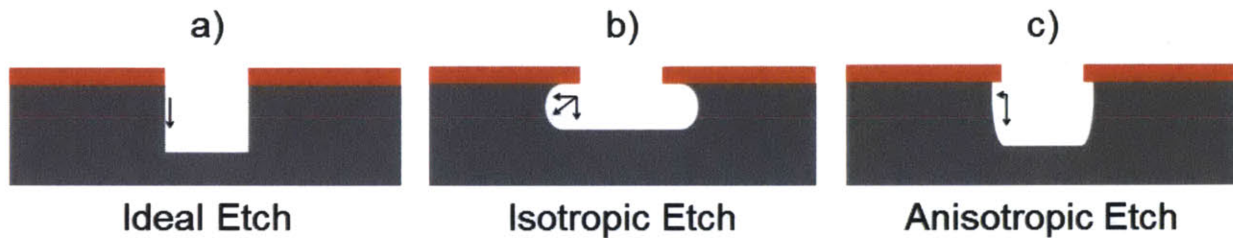

Figure 2.1: Common dry etching profiles, **a)** ideal etch profile, **b)** isotropic profile, **c)** anisotropic profile. The red layer represents the mask over the gray silicon. Arrows indicate the directionality for each type of etch.

2.1.2 Mask Erosion and Etch Selectivity

Mask erosion refers to the loss (in both the vertical and lateral directions) of mask material by physical and chemical processes that occur during an etch. Etch selectivity refers to the relative rate at which the substrate material is vertically etched versus the rate at which the masking material is vertically eroded. As the mask serves as a protective barrier against etching in unwanted regions of the substrate, knowing the selectivity of possible mask / substrate combinations in a particular etching system is very important. Photoresist is among the most common masking materials and was used for the etch mask in this work, but other options widely used in plasma etching include silicon dioxide (SiO_2) and silicon nitride (Si_3N_4), as well as metals like aluminum and titanium.

2.1.3 Etch Uniformity

Etch uniformity refers to the consistency of etch properties across a substrate, and in particular the etch depth. The uniformity of an etch is primarily governed by the transport of reactant species to the substrate and the transport of product species away from the substrate. This transport depends on the properties of the process gas distribution and ionization systems, the vacuum pumping system, and also the physical layout of the region to be etched on the substrate (known as the "load" or the "loading effect"). There are two different types of loading that affect etch uniformity, which are known as macroloading and microloading. Macroloading refers to the situation where substrates with larger total fractions of exposed area etch more slowly than substrates with less total exposed area. This occurs because the transport of reactants to the substrate is roughly equal and independent of the substrate geometry, but for substrates with more exposed area a larger portion of the total reactants is used, leading to partial depletion of the available reactants and slower etching. On the other hand, microloading occurs when features of different sizes are being etched on the same portion of a substrate. Here, localized depletion of reactants caused by differences in transport times leads to larger features etching at a faster rate than smaller features. This is particularly noticeable when high aspect ratio features are being etched as it becomes increasingly difficult for reactants to reach the bottom of small features and also increasingly difficult for reaction products to be removed from the small features. The microloading effect is commonly referred to as aspect ratio dependent etching (ARDE) or RIE-lag. **Figure 2.2** shows a cross-sectional image of a Bosch Process etch displaying the effect of micro loading.

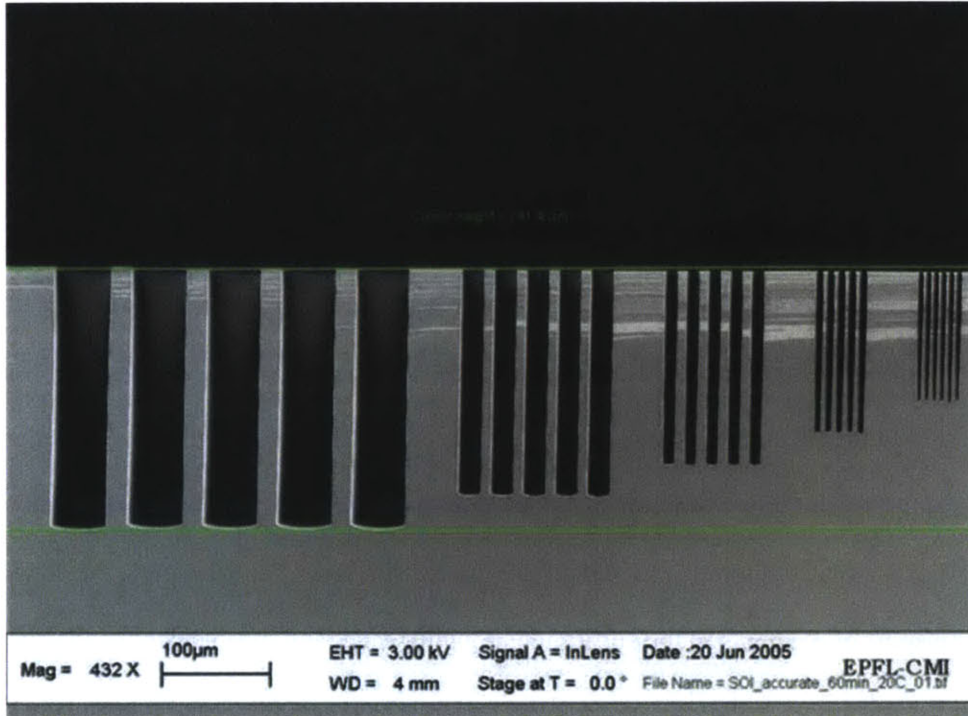

Figure 2.2: Example of microloading, or aspect-ratio dependent etching (ARDE). The narrower features etch slower than the wider features. Image courtesy of EPFL [5].

2.2 Plasma Basics

Plasma etching processes use a combination of a chemical reactions and physical sputtering to remove material from a substrate. To create the necessary conditions for these processes to occur, low pressure and high density plasma discharges are required. High density plasmas are needed to create an abundance of ions and radicals by dissociation of a process gas species. Low pressures are needed to increase the mean free path of the process molecules and dissociation products, which helps in the transport of the ions and radicals to the substrate. The simplest plasmas are formed by applying a large DC voltage across two electrodes. When the bias is large enough, electrons gain enough energy (energies higher than the ionization energy of the process gas molecules) such that they are able to ionize the process gas molecules and ignite a plasma. For a given plasma type there exists an optimal pressure for ignition, which can be shown through Paschen's Law (**Eqn. 2.1**). Paschen's Law states that the voltage required to strike a plasma is proportional to the pressure distance product ($p \times d$) and the properties intrinsic to the process gas being ionized (constants a and b). As the pressure distance product decreases below the optimal

value, the magnitude of the voltage needed to ionize the molecules increases substantially because the mean free path (MFP) increases to the point where collisions between electrons and molecules become rare. Above the optimal value, higher voltages are also required because of reductions in the mean free path, which increases the collision frequency for electrons, making it difficult for them to accumulate enough energy to ionize a process gas molecule. An example of a Paschen curve is shown in **Figure 2.3**. For most plasma etching systems, the pressure range of 10-100 mTorr is ideal for striking and sustaining a plasma discharge. Although Paschen's Law was formulated during the study of glow discharge and parallel plate plasma systems, the same phenomenon applies to capacitively coupled plasmas (CCP) and inductively coupled plasmas (ICP), which are two of the most common types of plasma discharges, and also the types utilized in the 1" Fab DRIE. Both CCP and ICP generation methods are described below in **Section 2.3**.

$$V = \frac{apd}{\ln(pd) + b} \tag{2.1}$$

where:
V: dissociation voltage
a & b: gas specific constants
p: pressure
d: plate separation

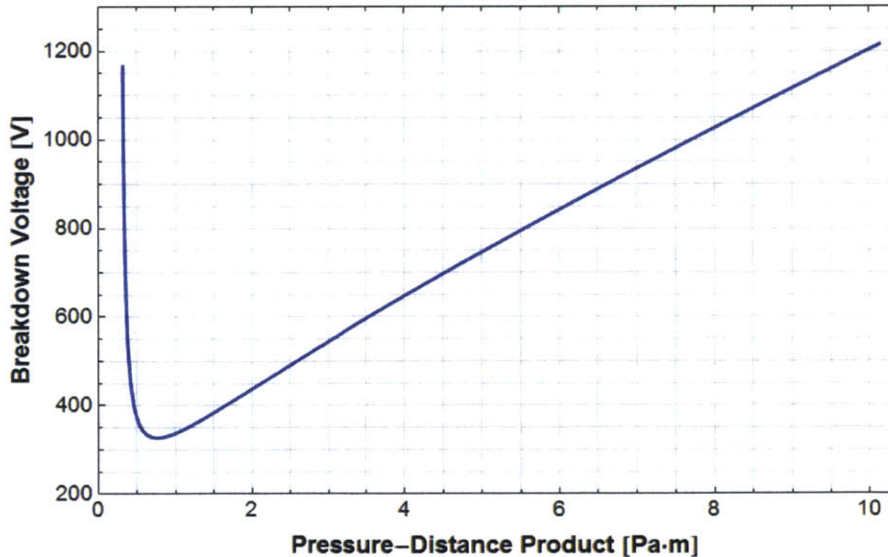

Figure 2.3: Paschen's Law plotted for air in a DC glow discharge plasma. The minimum voltage required to strike the plasma is ~325V at a $\boldsymbol{pd}$ product of 0.75 Pa·m.

Plasma discharges are sustained through the continual generation of ions by collisions between highly energetic electrons and process gas molecules. For the following reasons, this process is very difficult.

First, the disparity between the masses of electrons and gas molecules means that electrons only impart a limited amount of energy during a collision. Secondly, given a Maxwellian distribution of electron energies, only a small portion of the electrons have accumulated enough energy to ionize the process gas molecules (electron-process gas molecule collisions can also generate free radicals). These obstacles to ionization are why, even in very dense plasmas (excepting fusion-based or stellar-based plasmas), just 1% of the gas molecules may be ionized. In response to these difficulties, much effort has been spent to develop plasma generation methods that improve the electron-molecule energy transfer efficiency and generate higher density plasmas.

2.3 Plasma Generation and Etching Techniques

Two of the most widespread etching technologies used in MEMS are reactive ion etching (RIE) and deep reactive ion etching (DRIE), a variant of RIE specifically aimed at creating anisotropic, high aspect ratio features. RIE processes have been developed to etch a variety of materials including silicon, III-V semiconductors, silicon carbide, and insulating oxides [6]. Depending on the process parameters, RIE processes can produce isotropic or anisotropic profiles in many materials, but for devices that need large aspect ratios with vertical or near vertical sidewalls, DRIE is the most common process choice. One of the most common forms of DRIE, the Bosch Process, has been the enabling processing technique for many MEMS devices, and is ultimately the target technique for the etching system characterized in this thesis. **Section 2.4.4** provides an explanation of the Bosch Process.

Two of the most common types of plasma discharges used in RIE and DRIE equipment are capacitively coupled plasmas (CCP) and inductively coupled plasmas (ICP). CCP discharges are commonly used in parallel plate RIE reactors, and ICP discharges are utilized on most modern DRIE systems. The primary difference between CCP and ICP lies in the way they couple energy into the chamber to produce plasma. A detailed explanation of ICP and CCP operation is discussed in the following sections.

2.3.1 Capacitively Coupled Plasmas

In capacitively coupled plasmas (CCP), gas molecules within the chamber are excited by an RF generator coupled in series with a blocking capacitor, (as seen in **Figure 2.4**). As the molecules are excited by the oscillating electric field, electrons begin to get stripped from the process gas molecules producing free radicals and ions which are used for etching.

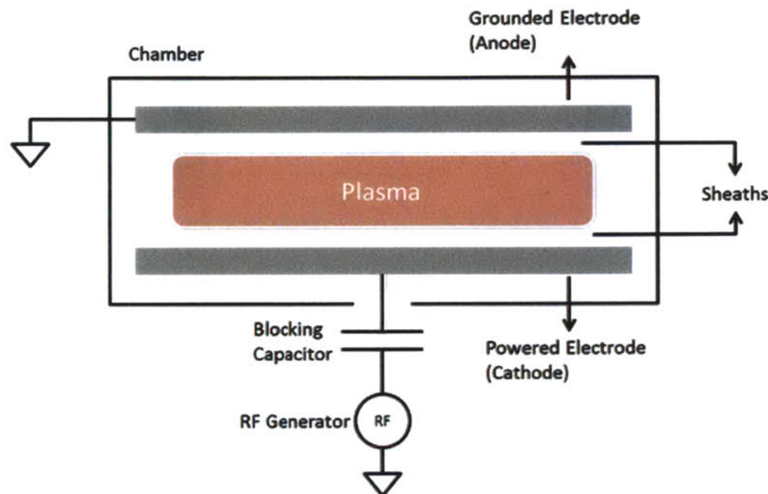

Figure 2.4: Diagram of a reactive ion etching (RIE) system utilizing capacitively coupled plasma (CCP).

In this configuration, the energy required to generate the discharge is transmitted through plasma sheaths which act like the dielectric portion of a capacitor, hence the name "capacitively coupled". These sheath regions are commonly referred to as dark regions, as they have a low plasma density and emit no light. Plasmas are quasineutral, and therefore sheaths are formed along the chamber walls and electrodes to maintain this quasineutrality as RF power is applied. When power is applied to the cathode the lighter electrons are able to follow the quickly alternating field better than the heavier ions, leading to a buildup of negative charge on the powered electrode (V_{bias}). The rate at which the electrons are lost is unsustainable and thus the plasma gains a slightly positive potential (V_p). The relationship between V_{bias} and V_p is shown in **Eqn. 2.2** and also graphically in **Figure 2.5**. The difference between the bias voltage and the plasma voltage is defined as the "sheath voltage" ($V_{sheath} = V_p - V_{bias}$) and it is this voltage that attracts ions to the substrate.

$$V_p = \frac{V_{RF} + V_{bias}}{2} \tag{2.2}$$

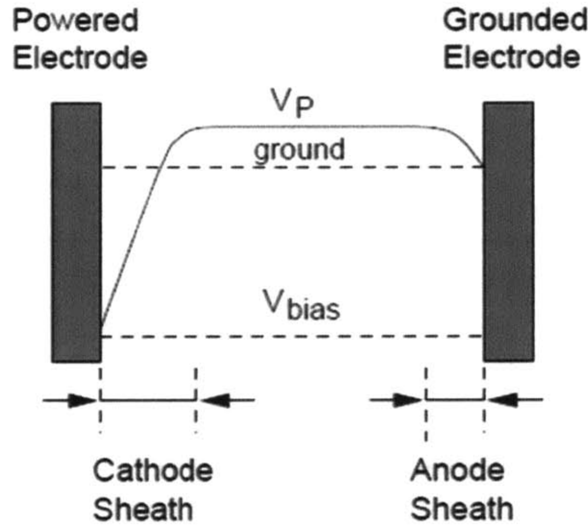

Figure 2.5: Plasma sheath voltages as seen in a CCP system with two electrodes of the same area. The powered electrode (cathode) shows a more negative sheath voltage than the grounded electrode sheath voltage. The plasma potential is slightly positive. Figure courtesy of H. N. Park, et al [7].

$$\varepsilon_{Ion} = q * (V_p - V_{bias}) \tag{2.3}$$

Given this sheath voltage, the average ion energy (ε_{Ion}) can be expressed using **Eqn. 2.3**, where q is the charge of the ion. This equation shows that the sheath voltage is very important in CCP-based etching as it directly affects the energy of the ions. As a result, many methods have been developed to control the bias voltage [7]. One method used to change the sheath voltage is to change the relative areas of the electrodes. The relationship between electrode area and sheath voltage is shown in **Eqn. 2.4**. The fourth power dependence makes using different size electrodes a very powerful method for controlling the voltages across each sheath region.

$$\frac{V_a}{V_b} = \left[\frac{A_b}{A_a}\right]^4 \tag{2.4}$$

where:
V_a: Sheath voltage of smaller electrode
V_b: Sheath voltage of larger electrode
A_a: Area of smaller electrode
A_b: Area of larger electrode

Depending on the application, CCPs come in two configurations: substrate powered or substrate grounded. In the RIE configuration (shown in **Figure 2.6a**), the chamber remains grounded and the substrate platen is powered. In this configuration the powered electrode has a much smaller area, and therefore generates a large sheath voltage (**Eqn. 2.4**) and large ion energies (**Eqn. 2.3**), which are advantageous for etching. In the opposite configuration (shown in **Figure 2.6b**), the substrate is held on the grounded electrode, which has the smaller sheath voltage is lower, which decreases the directionality of ions and radicals thus decreasing etch rates. This configuration is known simply (and confusingly) as "plasma etching". This latter configuration can be useful however in processes like plasma-enhanced chemical vapor deposition (PECVD) where the low sheath voltage limits the amount of ion bombardment, and enhances deposition via free radical reaction and decomposition on the substrate surface.

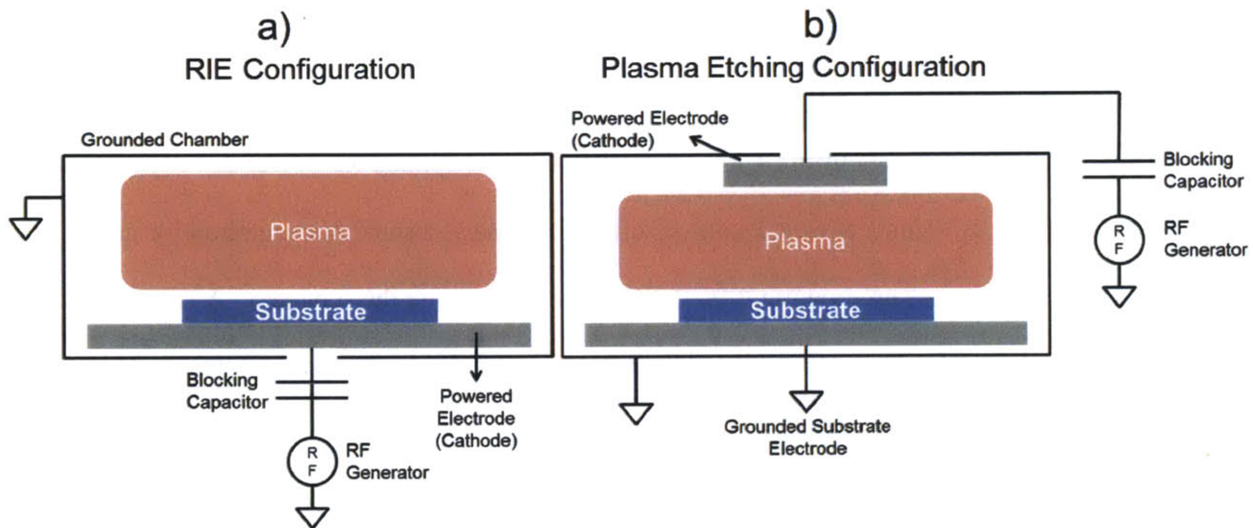

Figure 2.6: The two types of CCP etchers, known as **a)** reactive ion etchers (RIE) and **b)** plasma etchers. **Part a)** shows the standard RIE configuration in which the substrate electrode is powered and the chamber is grounded. **Part b)** shows the standard plasma etching configuration in which the substrate is grounded with either the chamber or an electrode within the chamber being powered.

2.3.2 Inductively Coupled Plasmas

Inductively coupled plasmas (ICP) can be generated by passing RF current through a helical coil wound around a cylindrical vacuum chamber. By way of Ampere's law, the RF voltage applied to the coil generates a time varying axial magnetic field **B(z)** which then via Faraday's law (**Eqn. 2.5**) creates an

azimuthal electric field **E** within the chamber. This electric field induces circulating currents within the chamber causing the electrons to gain enough energy to ionize the process gas molecules and ignite a plasma. A graphical representation of circulating currents and the electric and magnetic fields are shown in **Figure 2.7**.

$$\nabla \cdot E = -\frac{\partial B}{\partial t} \tag{2.5}$$

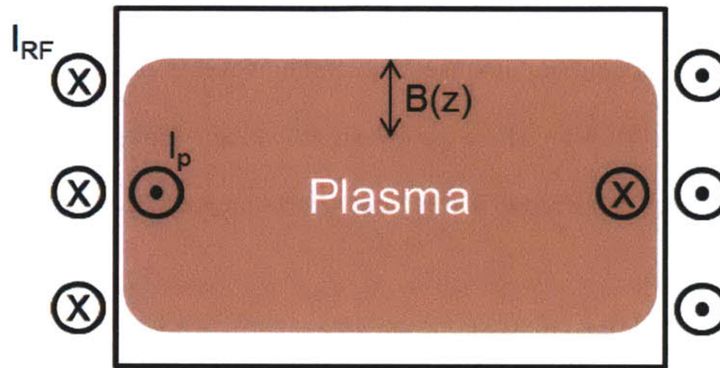

Figure 2.7: Depiction of the applied ($\boldsymbol{I_{RF}}$) and induced ($\boldsymbol{I_P}$) currents in ICP used for plasma generation.

When the RF power applied to an ICP discharge is increased, the plasma density increases, but the sheath voltage is unaffected. This differs from CCP discharges, where the applied RF power directly affects the sheath voltage (**Eqn. 2.2**). This makes ICP sources difficult to use as a standalone method for dry etching, as the sheath voltages are important for driving ion migration to the substrate. As a result, ICPs are commonly coupled with a CCP electrode configuration to provide sheath voltage control. This configuration, commonly known as ICP-RIE, is very powerful as it provides for independent control of the plasma density and sheath voltage (and thus the ion energy). A diagram of this type of system, which is used in many modern etchers including the 1" Fab DRIE, is shown in **Figure 2.8**.

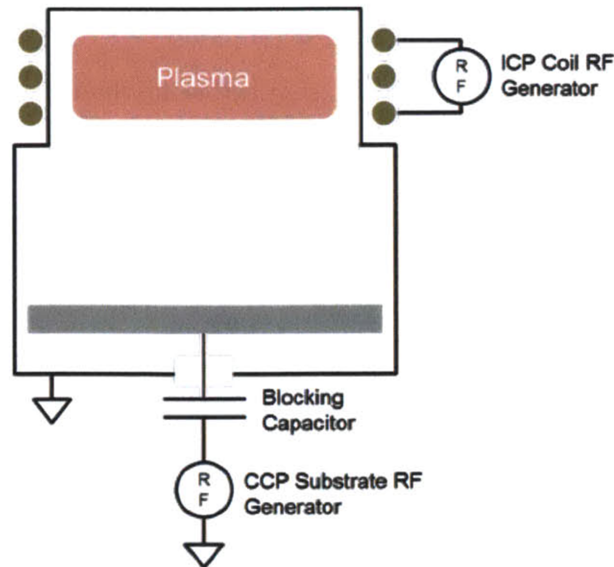

Figure 2.8: An illustration of an ICP-RIE system. The plasma is generated using an ICP coil, and the substrate sits on a powered, RIE-style electrode which controls the incoming ion energies.

ICP plasmas have two characteristic operating regions. At low RF powers, high voltages between the ends of the coil initiate a capacitively coupled discharge. This region is known as E-discharge and exhibits low luminosity and low plasma densities. As the RF power is increased, the second region, known as the H-mode discharge, is reached when the nonlinearities of the absorbed power require the establishment of a new power equilibrium point. The transition to the H-mode can be observed by an abrupt change in luminosity and an increase in plasma density. A more detailed explanation of the E→H transition can be found in **Section 4.1.2**.

Two main coil geometries exist for ICP sources, helical coils and planar coils. Helical coils produce highly dense plasmas, however due to circumferential electron currents the plasmas display ring shape density profiles, with the center exhibiting the least dense plasma. To account for this nonuniformity, helical ICP coils are generally placed far away from the substrate to allow space for diffusion to homogenize the plasma density and thus the etch rate across the wafer. Planar ICP coils on the other hand create much more uniform plasmas, but with smaller overall densities. Planar ICPs also use oscillating magnetic fields to induce circulating electric fields within the plasma. **Figure 2.9** shows an illustration of a planar ICP-RIE system and a diagram of the fields induced by the planar coil. Many patents have been

filed that attempt to combine the best properties of the two coil geometries to obtain to an ideal mix of uniformity and etch rate [8]. The 1" Fab DRIE described in this thesis uses a helical coil type ICP for its ability to produce large plasma densities and provides several inches of spacing between the coil and substrate chuck to ensure the distribution of ions and radicals is uniform for the etching process.

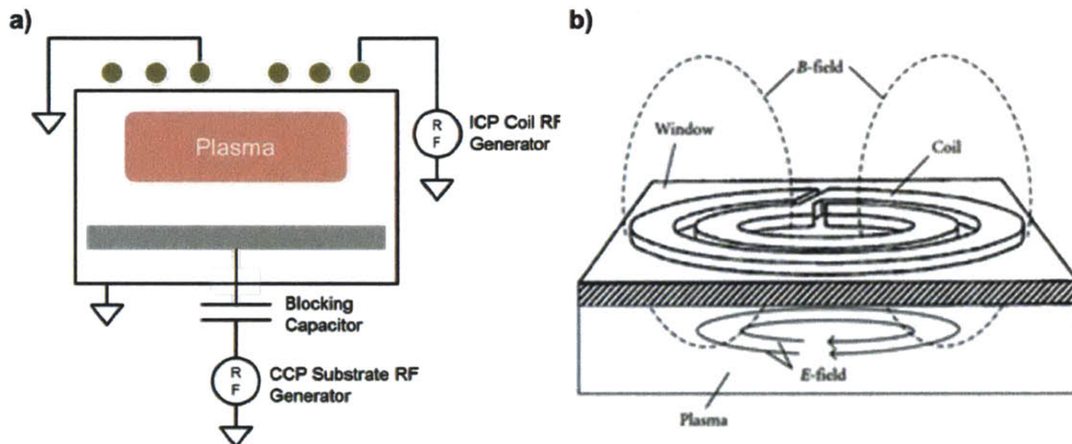

Figure 2.9: Planar ICP configurations. **Part a)** shows a planar ICP-RIE configuration very similar to Figure 2.8. **Part b)** shows the induced magnetic and electric fields that are used for plasma generation.

2.4 Etching Mechanics and Chemistry

Plasmas are useful for semiconductor processing because they contain relatively high densities of ions and radicals. Ions can be accelerated by externally applied electric fields and have increased chemical reactivity. The radicals generated in plasmas are usually electrically neutral (the fluorine radicals discussed below are neutral) and are very reactive due to their incomplete valence electron shell.

2.4.1 Halogen-based silicon etching

Paired with a compatible substrate material, ions and radicals by a plasma discharge will react with and (with sufficient energy) sputter away atoms from the substrate surface. For silicon substrates, the most common plasma etch gases contain halogens like fluorine, chlorine and bromine [9]. This is due to halogens' large affinity for reacting with silicon atoms to form tetrahalosilane compounds like silicon tetrafluoride (SiF_4) or silicon tetrachloride ($SiCl_4$). These new compounds are then either removed from the silicon surface spontaneously because of high volatility (SiF_4, and in many processing conditions

$SiCl_4$), or by ion bombardment ($SiBr_4$). Fluorine was the halogen chosen for etching in this thesis because it has the highest reactivity with silicon and generally produces the largest etch rates. The specific process gas used is sulfur hexafluoride (SF_6), which has the advantages of being nontoxic, relatively inexpensive, and incredibly well studied. SF_6 is also one of the primary process gases used in the Bosch Process.

2.4.2 Silicon etching with SF_6

Fluorine-based silicon etching via SF_6 fits nicely into the sequential step interpretation of plasma etching concisely articulated by H. Jansen, et al [9]. This sequence of mechanisms for the SF_6-silicon etching system is explained below and also shown graphically in **Figure 2.10**.

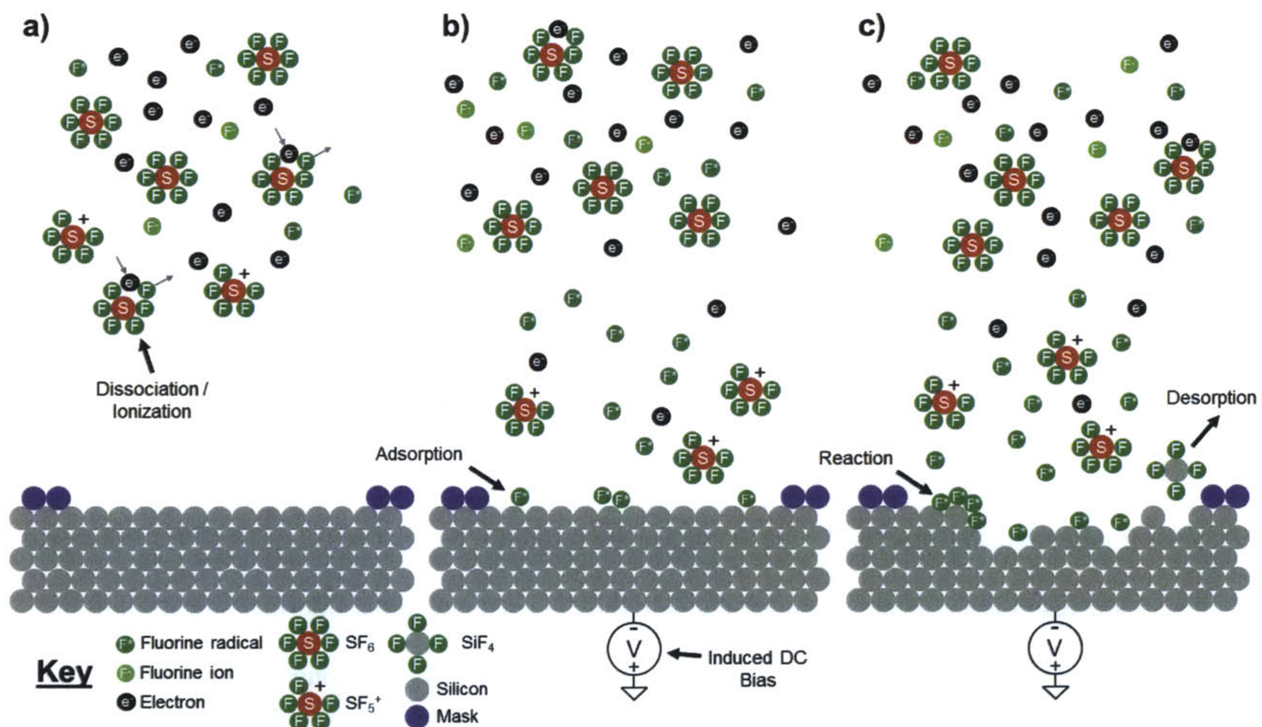

Figure 2.10: Sequence of steps in an SF_6 etch process. In **Part a)** the energy from the plasma causes the SF_6 molecules to dissociate and ionize, creating ions and radicals. In **b)** the fluorine radicals adsorb to the silicon surface. In **c)** the radicals react with the exposed silicon atoms to form SiF_4, which is volatile and desorbs from the surface.

When SF_6 is first injected into the evacuated process chamber, it is a stable molecule that is nonreactive with the silicon substrate. When RF energy is coupled into the system to form a plasma, the SF_6 molecule

is dissociated and/or ionized to yield many different particles including cations (SF_5^+), anions (F^-), radicals (F*), and other neutral species (**Figure 2.10a**). In CCP and ICP-RIE systems, the ions among these will be influenced by the electric fields created by the RF power applied on the substrate electrode, and in particular will be affected by the induced DC bias (negative) that forms on the substrate electrode (see **Section 2.3** for more details).

Neutral particles like the fluorine radicals are not directly affected by the electric fields from the applied RF power and the substrate DC bias, but through a combination of diffusion, forced convection from the vacuum pump, and collisions with charged particles that have been accelerated by the electric fields, neutral particles are transferred from the bulk plasma generation region to the substrate. Upon reaching the silicon substrate, fluorine radicals will adsorb to the surface and spontaneously react with the exposed silicon (**Figure 2.10b**). This spontaneous reaction is an important difference between fluorine-based etch chemistry and the chemistries of other halogen-based silicon etching systems like chlorine and bromine. In chlorine and bromine-based systems, the spontaneous reaction rate with silicon is near zero, and external energy in the form of ion bombardment is required to initiate the chemical reactions (this is commonly referred to as chemical sputtering)[3]. Ion bombardment (from the relatively heavy SF_5+ ions (molecular mass: 127)) also occurs in SF_6-based etching, providing extra energy for chemical reactions and also physically sputtering atoms and molecules from the substrate surface.

When the fluorine radicals react with silicon atoms they form SiF_x compounds ($1 \leq x \leq 4$). When x is less than 4, the result is a radical compound that will look to react with other fluorine radicals until the inert SiF_4 is formed (the net reaction is written as $Si + 4F \rightarrow SiF_4$). As mentioned earlier, SiF_4 is very volatile and, once formed, will easily desorb from the substrate (**Figure 2.10c**). Other silicon atoms and SiF_x compounds may be dislodged from the substrate by ion-induced physical sputtering, but

[3] This can be advantageous in certain circumstances, as the directionality of the ions can be controlled using the substrate electrode (through the applied RF power and DC bias), which in turn creates directionality (anisotropy) in the etch profile. This process is known as "ion-induced RIE" [9].

investigations have suggested that a large majority of silicon atoms leave the bulk substrate in the form of SiF_4 molecules [10].

2.4.3 SF_6+O_2 Etching

One common variation on the standard SF_6 etching system (and one employed in this thesis) is the introduction of small amounts of oxygen into process chambers along with the SF_6. This added oxygen has two primary effects on the system. First, oxygen is catalytic in increasing the concentration of fluorine radicals generated by the plasma [11,12]. Since fluorine radicals are the main actors in the SF_6 etch process, this increase leads to faster etch rates. Second, oxygen reacts with free fluorine radicals and the silicon surface to form polymeric $Si_xO_yF_z$ compounds that effectively passivate the silicon surface. If the growth of these compounds is left unchecked, it will retard the etch rate by blocking fluorine radicals' access to the bare silicon surface. However, the $Si_xO_yF_z$ molecules can be removed via the normal ion bombardment that occurs during etching. The directionality of this ion bombardment means that the polymer forming on the sidewalls of the etched features is removed at a lower rate than the bottom of the features. This phenomenon, if balanced properly with the etch rate from the fluorine radicals, can be used to create anisotropic etch profiles. If unbalanced, an etched feature may show increased lateral etching and an isotropic profile (not enough passivation), or it may begin to exhibit increased roughness (too much passivation) in the form of "black silicon" or "silicon grass" [13]. Silicon grass is an interesting phenomenon that comes about when the surface of an etch accumulates micro-scale deposits of materials that act as a mask against further etching below the region of the deposit. This occurrence is known as micromasking, and can be caused by sputtering and redeposition of mask materials during the etch process or by the formation of small islands of the passivating $Si_xO_yF_z$ molecules (or simply a dirty substrate surface).

The literature provides a variety of accounts of the ideal percentage of oxygen in an SF_6-based etching system, but most fall between 25% and 35% of the total gas flow [11,12,14]. This percentage, as it

applies to the performance of the 1" Fab DRIE, will be revisited several times in **Chapter 4**. Significant research has also been carried out on adding tertiary gases like trifluoromethane (CHF_3) to the SF_6/O_2 mixture with the aim of better controlling the amount of $Si_xO_yF_z$ passivation that forms on the silicon surface[15]. The widely known "black silicon method" for etch parameter determination in etching equipment uses this $SF_6/O_2/CHF_3$ gas mixture [13].

2.4.4 Bosch Process Etching

In the mid-1990s, the $SF_6/O_2/CHF_3$ RIE etching system developed at the MESA Research Institute (University of Twente, The Netherlands) was one of the most popular choices for the anisotropic etching of silicon [15]. By the early 2000s however, this popularity had been largely mitigated by a new "deep" reactive ion etching (DRIE) technique developed by Franz Laermer and Andrea Schilp of Robert Bosch GmbH [16]. This technique, known primarily as the Bosch Process (BP), steps between an SF_6-based RIE etching process (like the one described above in **Section 2.4.2**) and a C_4F_8-based plasma-enhanced chemical vapor deposition (PECVD) process for passivating the etched surfaces. By alternating rapidly between the RIE step and the PECVD step, features with vertical sidewalls and aspect ratios exceeding 50:1 can be formed [17]. Very fast etch rates can also be achieved using this technique, with modern BP equipment offering etch rates exceeding 30 μm/minute [18].

In the standard implementation of the Bosch Process (shown as a step-by-step process in **Figure 2.11**), the RIE step is performed using SF_6 as the only process gas. This means that no passivation film is formed during the etch, and the etch profile is largely isotropic. This may seem counter-intuitive for a process designed to produce highly anisotropic features, but the short duration of each RIE step (step times range from hundreds of milliseconds to tens of seconds depending on equipment capabilities)[4] means that lateral etching (as well as vertical etching) is limited. Individual RIE steps within a BP run may only etch a few hundred nanometers. Immediately after this short RIE step (**Figure 2.11b**) is completed, the PECVD second step begins. This step involves isotropically depositing a thin, conformal

[4] See **Section 3.2.4** on mass flow controllers for more information on the limits of individual step times.

layer of a fluorocarbon polymer using octofluorocyclobutane (C_4F_8) as the process gas (**Figure 2.11c**). The PECVD process operates in much the same way as plasma etching process. RF energy is used to create a plasma which generates ions and radicals, and these radicals are then transported to the substrate where they adsorb to the surface. The difference lies in the chemistry of reactive species, which instead of etching the substrate, prefers to generate nonvolatile compounds that stick to the substrate. Just like the passivating $Si_xO_yF_z$ films mentioned in **Section 2.4.3**, these nonvolatile compounds inhibit etching by the fluorine radicals by covering the exposed silicon reaction sites. Unlike the RIE step, there is generally very little RF power applied to the substrate electrode during the PECVD step, which helps to insure isotropy of deposition by limiting the directionality of the ions generated in the plasma. An isotropic deposition is very important, especially as the etched features deepen and the aspect ratios increase, because it prevents further lateral etching during the SF_6 steps.

After the fluorocarbon layer is deposited, the SF_6 step begins again. RF power is reapplied to the substrate electrode and the induced DC bias reappears, providing the vertical directionality for the ions produced in the ICP region of the plasma. The directionally accelerated ions physically sputter away the fluorocarbon layer on the bottom surfaces of the substrates (**Figure 2.11d**), while only mildly sputtering the passivation of the sidewalls. Once the fluorocarbon layer covering an area of the silicon is exposed the fluorine radical mechanism of etching can resume (**Figure 2.11e**). This process is repeated many times until the desired etch depth is reached (**Figure 2.11h**). After this point, the passivation layer and mask are generally removed using oxygen ashing or an appropriate chemical treatment, and processing of the device can continue (**Figure 2.11i**).

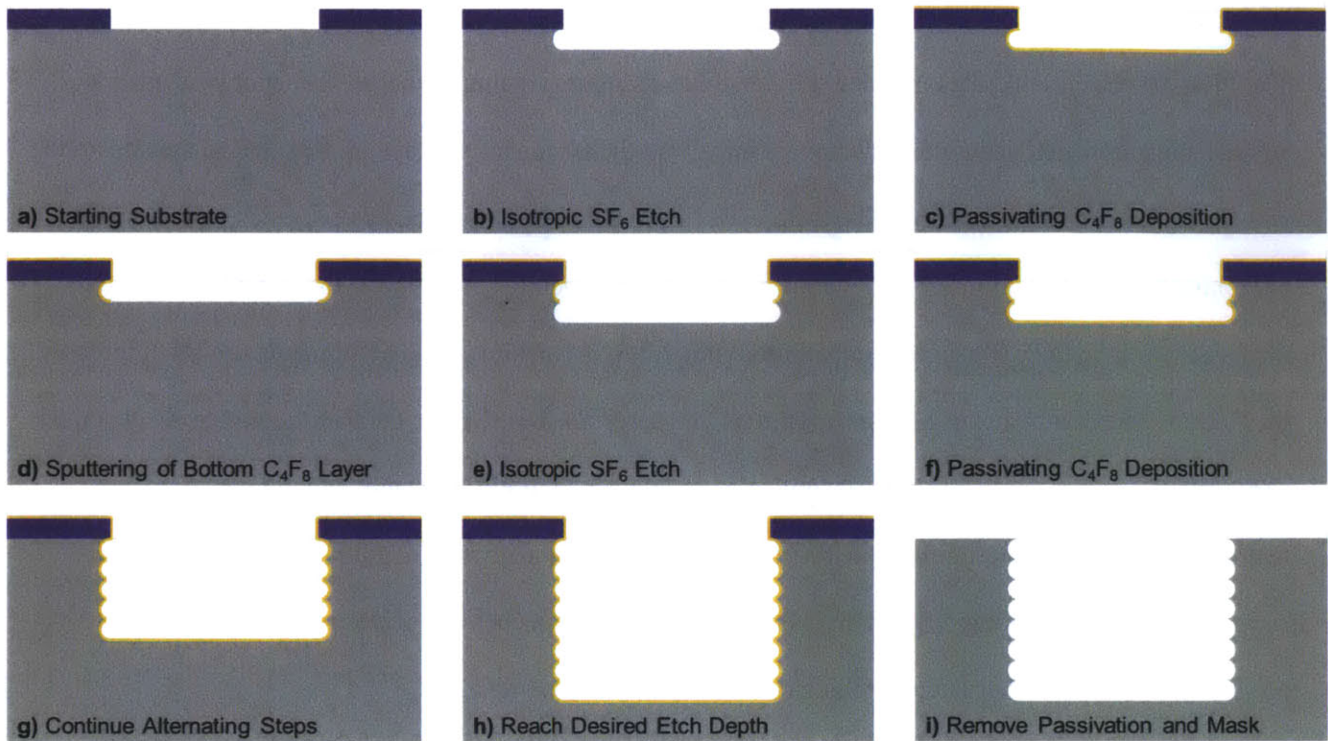

Figure 2.11: The Bosch Process sequence. The process alternates between steps of SF_6-based etching and C_4F_8 deposition to achieve high aspect ratio features in silicon.

By repeatedly cycling through these two steps (SF_6 etching and C_4F_8 passivation), very anisotropic, high aspect ratio etches are achieved. It is important to note however, that unlike continuous processes for anisotropic etching, the sidewalls of features etched using the Bosch Process are not locally straight, due to the isotropic nature of each SF_6 etch step. Instead the features from BP etching have "scallops", or small indentations corresponding to each iteration of the isotropic SF_6 step. The size of these scallops can be modulated by the changing the length of the SF_6 steps, where longer steps introduce larger scallops but also enable faster etch rates. Most BP tools have multiple process recipes optimized to offer either etch profiles with very flat sidewalls or overall faster etch rates.

Chapter 3: Design of the 1" Fab DRIE

3.1 Design Overview

The 1" Fab DRIE system was designed around the goals of functionality, ease of fabrication, and low cost. The functionality goal means that the 1" Fab DRIE should perform all the same physical and chemical processes of commercial DRIE systems, just at a smaller scale. The ease of fabrication goal means that efforts were made wherever possible to use standard, off-the-shelf parts, and where this was not possible, to avoid part designs that are overly time-consuming or require advanced or obscure machining techniques. Lastly, one of the inherent advantages of the 1" Fab platform is its low cost, and design decisions were always made with an eye toward minimizing costs wherever reasonable. A full spreadsheet breaking out the costs (both materials and labor) of the 1" Fab DRIE as described in this thesis is included in **Appendix A**. The current iteration of the 1" Fab DRIE can be built for under $32,000, broken up into ~$5,800 for the materials and labor to build the full chamber assembly and ~$25,800 for all of the associated peripherals like RF generators and mass flow controllers. A system block diagram is included below (**Figure 3.1**), with locations of the descriptions for each component noted.

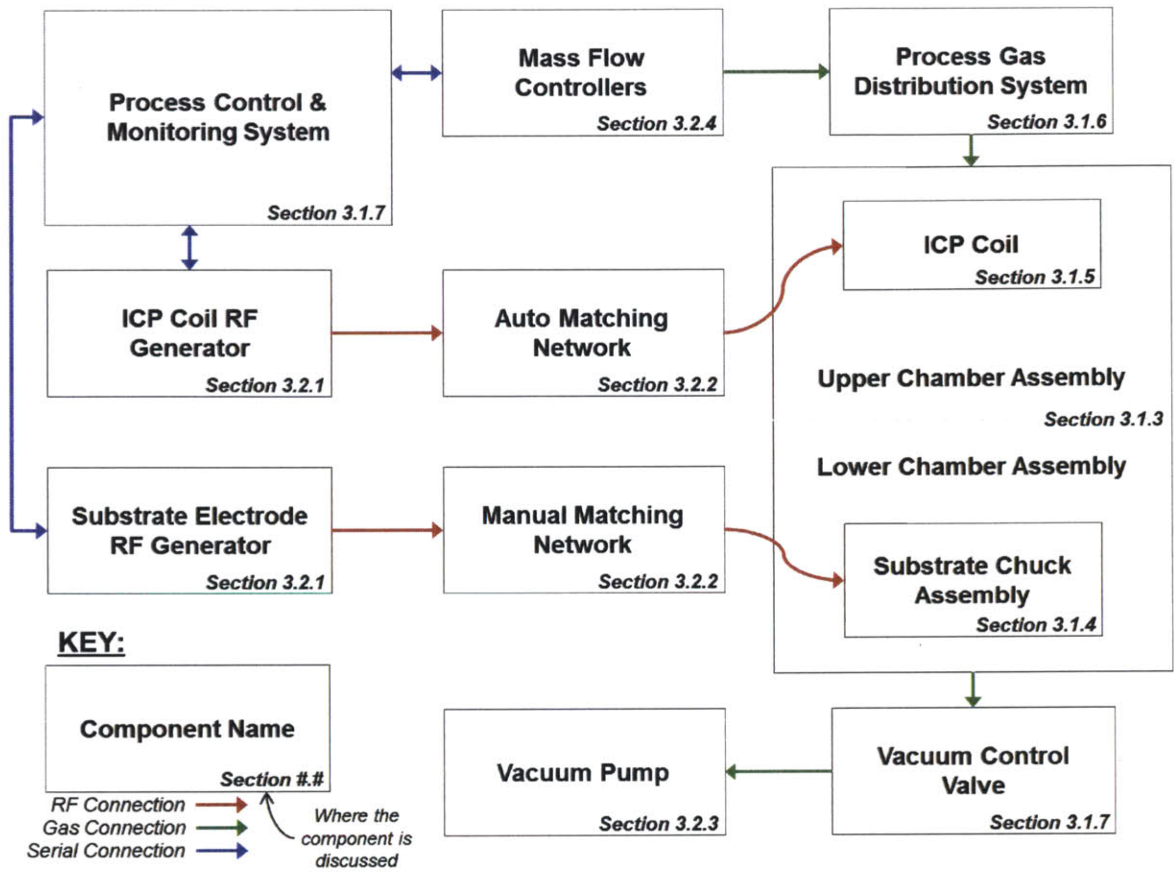

Figure 3.1: Block Diagram of the 1" Fab DRIE system. Each component is discussed in the section listed at the bottom right of the block.

3.1.1 System Basics

As its name suggests, the 1" Fab DRIE is designed to etch substrates with a characteristic dimension on the order of 1". Round, square, and irregular substrate geometries of this size range are all compatible with the system (for example, 1.18" x 1.18" (30 mm x 30 mm) wafer pieces prepared from 6" (150 mm) wafers were used in the testing and characterization portions of this thesis). The etcher itself (depicted in **Figure 3.2**) is modelled after a traditional ICP-RIE system. The etching chamber consists of a cylindrical alumina (Al_2O_3) tube capped with aluminum flanges and O-ring seals. This chamber mates via an additional O-ring to another flanged cylinder assembly containing the substrate chuck and vacuum port. Like a bell jar-style vacuum chamber, the upper chamber assembly is removed to load a sample, and replaced to begin pumping down to vacuum. The detailed descriptions and justifications for each of the components in the system follow in the sections below.

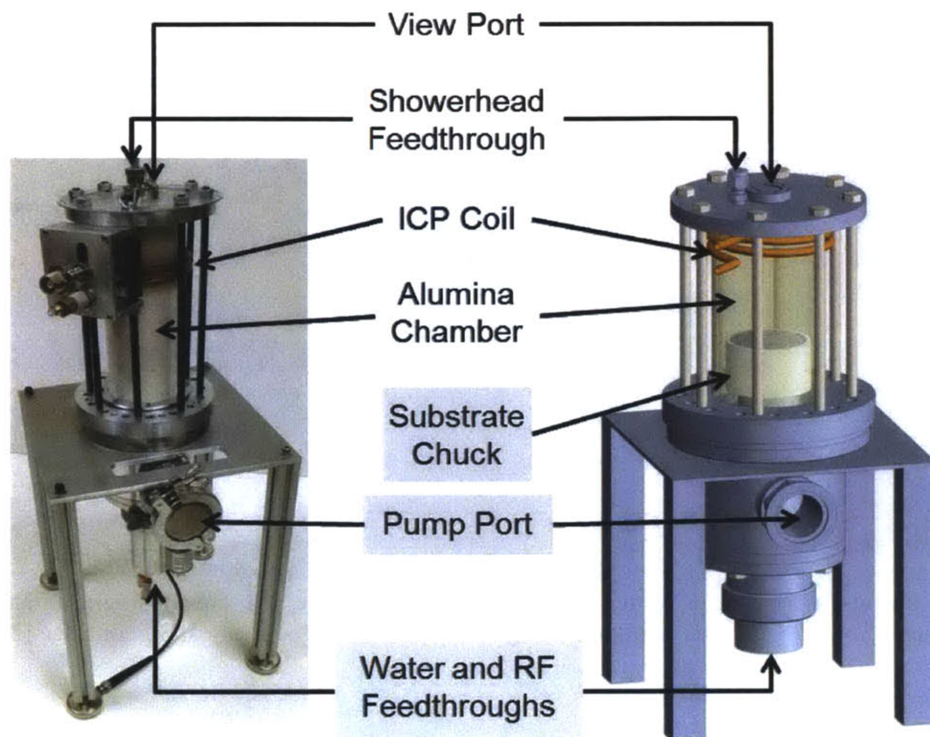

Figure 3.2: The full 1" Fab DRIE chamber assembly.

3.1.1.1 Substrate Sizing

The choice to use 1" substrates was motivated by several factors. Nearly all MEMS devices, which are the initial target of the 1" Fab platform, have die sizes less than 1 in^2 (645 mm^2). Most CMOS dies also fall into the sub-1 in^2 category. In fact, the exposure field of a standard i-line stepper for 8" (200 mm) wafers is 0.87" x 0.87" (22 mm x 22 mm) [19], which fits nicely onto a 1" square wafer while still leaving a small exclusion zone around the edge.

In silicon, 1" round wafers are no longer widely produced, but 1" square dies can be easily made by dicing larger wafers. For this thesis, 6" (150 mm) wafers were patterned with photoresist using standard 6" (150 mm) lithography equipment and then diced to form the 1.18" × 1.18" (30 mm × 30 mm) dies that were used during the characterization tests of **Chapter 4**. A rectangular arrangement of 16 dies of this size can fit on a single 6" (150 mm) wafer (with small amounts of the corner dies cut off). At exactly 1" × 1" (25.4 mm × 25.4 mm), 17 dies can fit on a single 6" (150 mm) wafer with no corner cutting (similarly, 32 full 1 in^2 dies can be had from one 8" (200 mm) wafer). **Figure 3.3** contains images of a 6"

(150 mm) wafer patterned with 1.18" × 1.18" (30 mm × 30 mm) dies, an individual die after dicing, and an illustration of how 1" x 1" (25.4 mm × 25.4 mm) dies can be laid out on a 6" (150 mm) wafer.

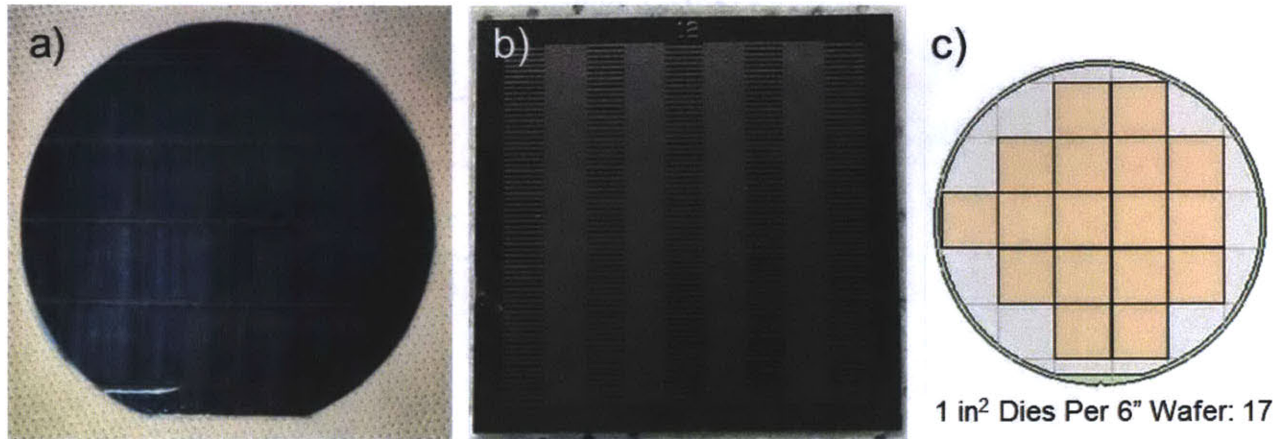

Figure 3.3: Die layouts. **a)** Shows a 6" wafer with 16 30 mm x 30 mm dies. **b)** shows a single 30 mm × 30 mm die. **c)** shows how 17 1 in^2 dies can fit on a single 6" wafer (image courtesy of SiliconEdge [20]).

3.1.1.2 Design Flexibility

The 1" Fab DRIE shown in **Figure 3.2** is designed as both a reasonable approximation to a production etching system and a prototype platform that allows adjusting as many of the parameters as possible. Some parameters, like the process gas flows and the RF powers are easy to vary. Others, like the actual geometry of the system, require some extra thought. In commercial etch system, the geometry is largely fixed, but this is only because the ideal sizes and spacings have already been determined through extensive testing and analysis. To make this same determination for the 1" Fab version of a DRIE, flexibility in the chamber geometry is needed. To this end, the current iteration of the etching system has the ability to change the spacings of the gas distribution showerhead, the ICP coil, and the substrate chuck assembly. Each of the three adjustable elements is capable of independently moving ~6" along the long axis of the cylindrical chamber. **Figure 3.4** shows how height adjustments to each of the elements are made.

The distance between the gas showerhead and the ICP coil sets the degree of process gas uniformity at the ionization height. Process gas molecules enter the chamber at six discrete points (see **Section 3.1.6** for an explanation of this configuration), and through diffusion form a (radially) uniform distribution, but this

diffusion process is not instantaneous. Thus using larger distances between the showerhead and ICP coil helps ensure more homogeneity at the ionization height, but also reduces the distance between the coil and chuck, which also has consequences.

The coil-chuck spacing affects the energies and uniformities of the ions and radicals created in the plasma. At small spacings, these particles only need to travel a small distance to reach the substrate, which increases their transport efficiency (more particles reach the substrate), but also decreases their spatial and angular uniformity. The increased ion bombardment from shorter distances may also lead to excess heating of the substrate. As the spacing between the chuck and the bulk plasma generation region increases, the ions must travel longer distances to reach the substrate, which increases their spatial and angular uniformity, but also decreases their collective energy due to an increased number of collisions with other molecules and an increased likelihood of recombination or absorption into the chamber walls.

Lastly, the spacing of the showerhead, coil, and chuck can be changed relative to the chamber itself, which allows the effective etching volume to be varied. Changing this volume affects the residence time of gas in the system, and the particular placement of the chuck assembly relative to the base plate assembly can also affect the actual chamber pressure by modifying the conductance through this flow path (and thus the pressure drop across it).

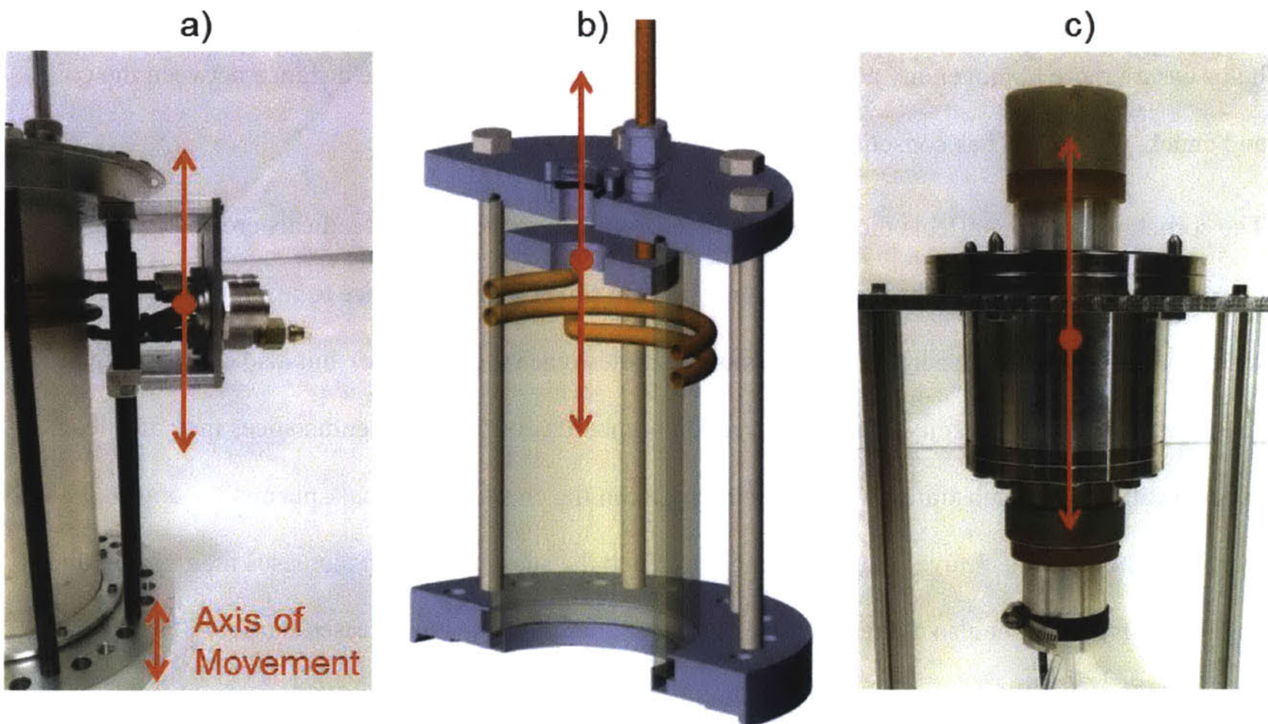

Figure 3.4: The three methods of adjusting the spacing within the chamber. **a)** The coil can be moved by adjusting the coil enclosure height. **b)** The gas showerhead can be moved up and down through a ¼" Ultra-Torr compression fitting. **c)** The chuck assembly can be moved up and down through 2" compression fitting.

3.1.1.3 Gate Valve Integration

The design as shown in **Figure 3.2** and described in detail through the remainder of this chapter requires fully venting the chamber each time a sample needs to be replaced or retrieved. While this configuration offers simple and quick access to the samples, in a production environment this is not an ideal method for maintaining process cleanliness or minimizing pump-down times. To this end, the chamber-base interface (the o-ring sealed CF6" flange) was specifically designed to allow a standard CF6" gate valve to be "dropped in" to the system with no modifications. This gate valve would allow the etch chamber to be sealed off from the substrate and chuck assembly during sample loading and unloading. A rendering of the design with a gate valve is shown in **Figure 3.5**. The procedure for its use would follow this sequence. First, while still under vacuum, the chuck assembly is lowered below the gate valve opening. Next, the gate valve is closed and the lower chamber assembly is vented. Once vented, the sealed upper chamber assembly is removed and any sample loading and unloading is carried out in the lower assembly.

While the upper chamber portion closed off by the gate valve is not actively being pumped down[5], it is certainly sealed well enough to prevent the accumulation of any contaminants for the duration of a sample load/unload process. After this is completed, the upper assembly is reattached, and the lower assembly is pumped down. Once under vacuum, the gate valve is opened and processing continues. In this configuration, the lower section of the etcher is effectively a load lock. This load-lock-style configuration also opens up the possibility of having multiple upper chamber assemblies which can be quickly swapped in depending on the particular application (e.g. distinct chambers for different substrate materials (Si, SiO_2, III-Vs) or different processes (DRIE, PECVD, ashing)).

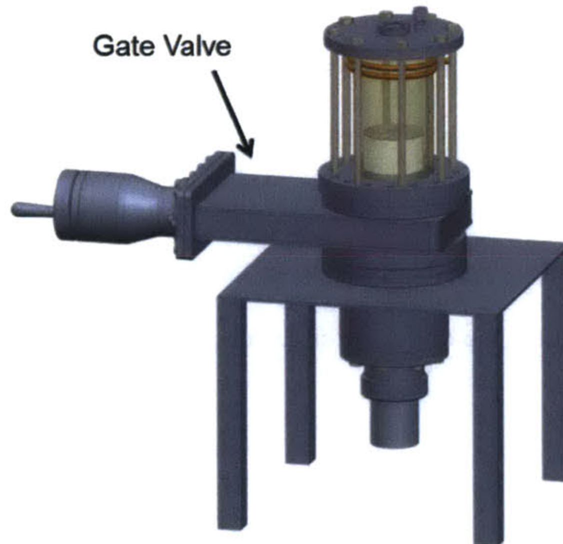

Figure 3.5: Rendering of the existing 1" Fab DRIE with a gate valve inserted between the upper and lower chamber assemblies.

3.1.2 Chamber Assembly Design

The etch chamber for the 1" Fab DRIE presented in this thesis has two main sections, referred to as the "upper chamber assembly" and the "lower chamber assembly". The upper assembly is comprised of an 8" long, (nominally) 3" ID, 3.5" OD (actual dimensions: ~2.85" ID, ~3.25" OD) 99.5% alumina cylinder compressed between two aluminum flanges with face sealing o-rings. The flanges and alumina cylinder are compressed together by screwing lengths of threaded rod into each of 8 blind tapped holes near the

[5] Although one could easily imagine a scenario where a small vacuum line is added somewhere on the topmost flange and only used while the upper chamber assembly is removed from the chamber.

perimeter of the lower flange, and then tightening nuts onto the threaded rods as it extended through the 8 corresponding through holes on the upper flange. An additional, compression-type axial-sealing o-ring is included on the lower flange for extra leak tightness on the mildly elliptical alumina cylinder. An image of the full upper assembly and a rendering of the exploded view are displayed in **Figure 3.6**. The top surface of the upper flange contains a CF1.33" knife edge at the flange center point and a ¼" Swagelok Ultra-Torr fitting 1" from the center. The CF1.33" flange can be used to hold a sapphire viewport or one of several Ultra-Torr fittings used as feedthroughs for diagnostic equipment. The eccentric Ultra-Torr fitting is the entry point for the process gas. The bottom surface of the upper flange contains a deep o-ring groove for aligning and compressing the alumina chamber.

The lower flange contains three different sealing surfaces, 8 blind tapped holes for the threaded rod compression scheme, and 16 through holes to mate with the CF6" flange that sits at the top of the lower chamber section. Two of the three sealing surfaces are standard o-ring grooves for the face and axial seals against the alumina cylinder. The third sealing surface is a CF6" knife edge that mates with the aforementioned CF6" flange at the top of the lower chamber assembly.

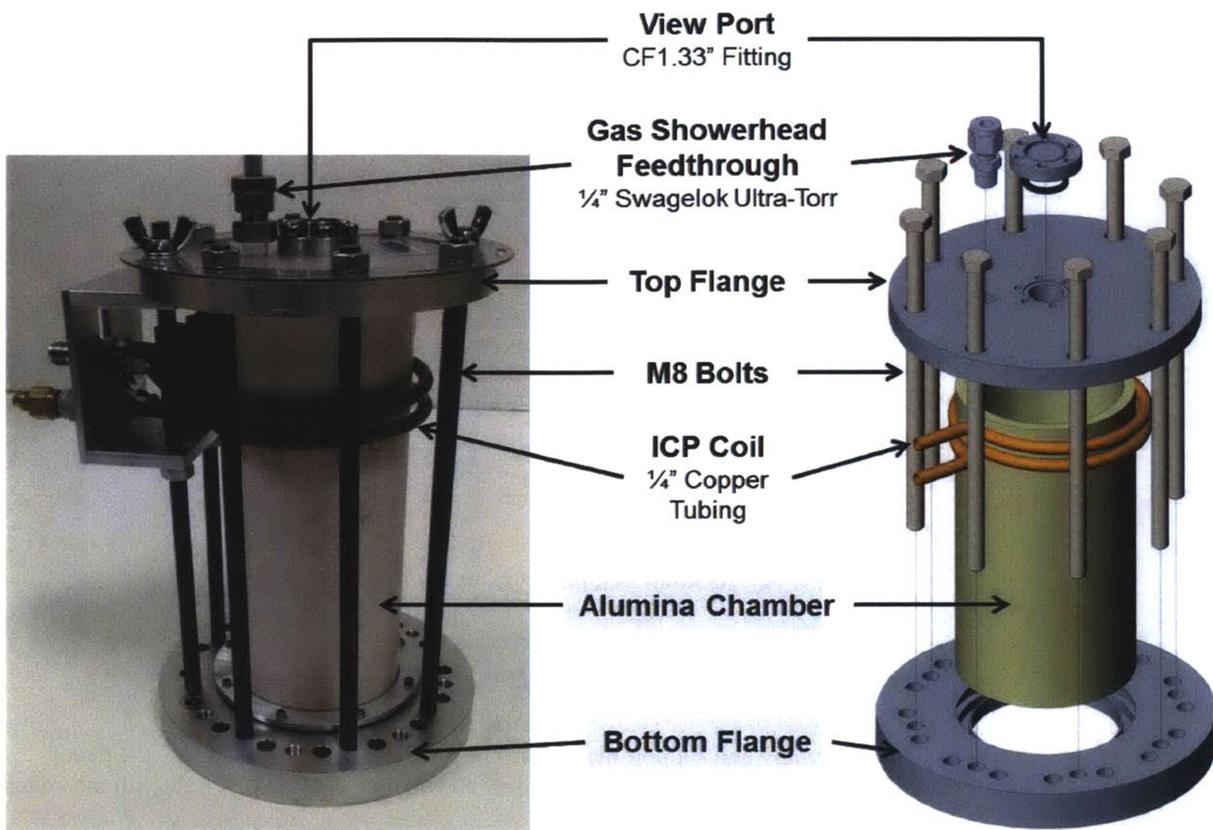

Figure 3.6: The upper chamber assembly. The entire assembly is 9" long and has an outermost diameter of 6.25".

The lower chamber assembly (shown in **Figure 3.7**) has four parts. At the top sits a CF6"-CF4.5" zero-length reducer flange, which is connected through a 3" long cylinder to a CF4.5" flange with a 2" compression port welded on for the chuck assembly feedthrough. These three components are held together by 4" long 5/16"-24 bolts that compress aluminum CF gaskets against the knife edge found on each mating surface. The fourth part of the assembly is a KF-40 to 1.5" NPT fitting for the vacuum line. The NPT end of this fitting screws into a taper-threaded hole on the side of the 3" long cylinder. This lower chamber assembly rests on a raised platform that provides stability for the full chamber and also a gap for the chuck assembly to be retracted through the 2" compression port. The raised platform also contains threaded holes that allow screws or bolts to provide axial alignment to the assembly. When the upper and lower chamber assemblies are brought together, these same alignment screws protrude through the through holes in the topmost CF6" flange of the lower assembly and provide points of axial alignment

for the upper assembly. In this way, the two parts of the chamber assembly can be separated and reconnected consistently and concentrically.

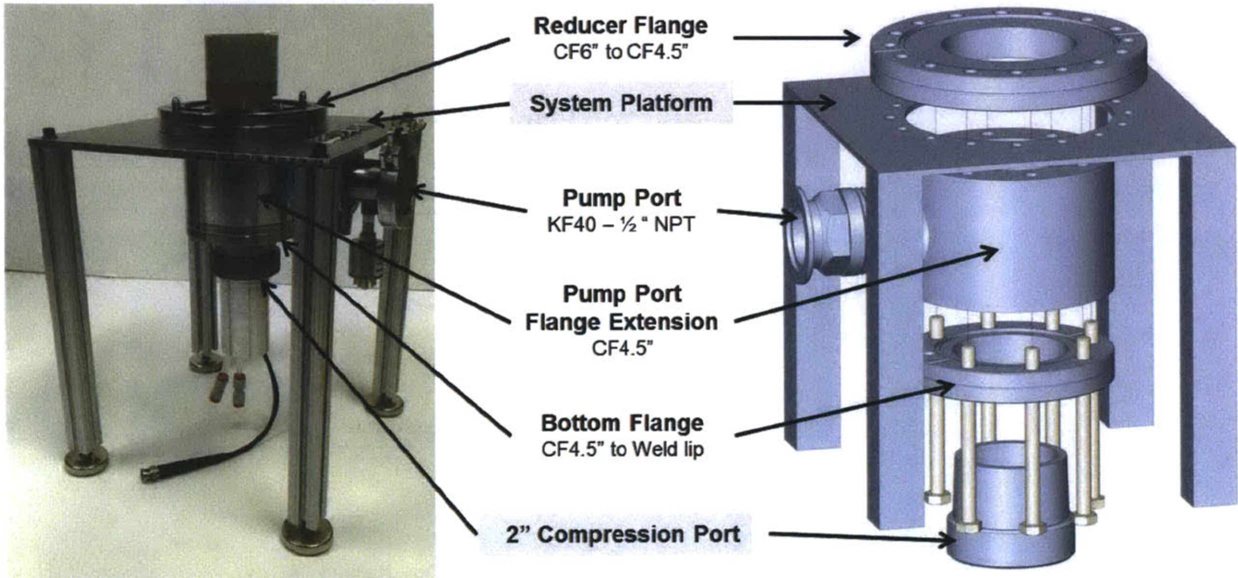

Figure 3.7: The lower chamber assembly and support platform. The platform is 14" tall to allow the chuck assembly to be raised and lowered. The actual lower chamber assembly shown on the left is pictured with the chuck assembly in place.

3.1.3 Chuck Design

The chuck assembly in the 1" Fab DRIE system was the most iterated upon piece of the design. In its final form, the assembly serves as a powered RF electrode, provides substrate registration and clamping, supplies water cooling to dissipate accumulated heat from the etching process, provides RF isolation from grounded portions of the chamber and chuck, and allows itself to be translated vertically while under vacuum via the 2" compression port. Three views of the final design are included in **Figure 3.8**. One of the capabilities missing from the design as shown is temperature sensing. This omission is discussed further in the final chapter and future revisions of the assembly will include at least one point of temperature measurement in the form of a shielded thermocouple or resistance temperature detector (RTD).

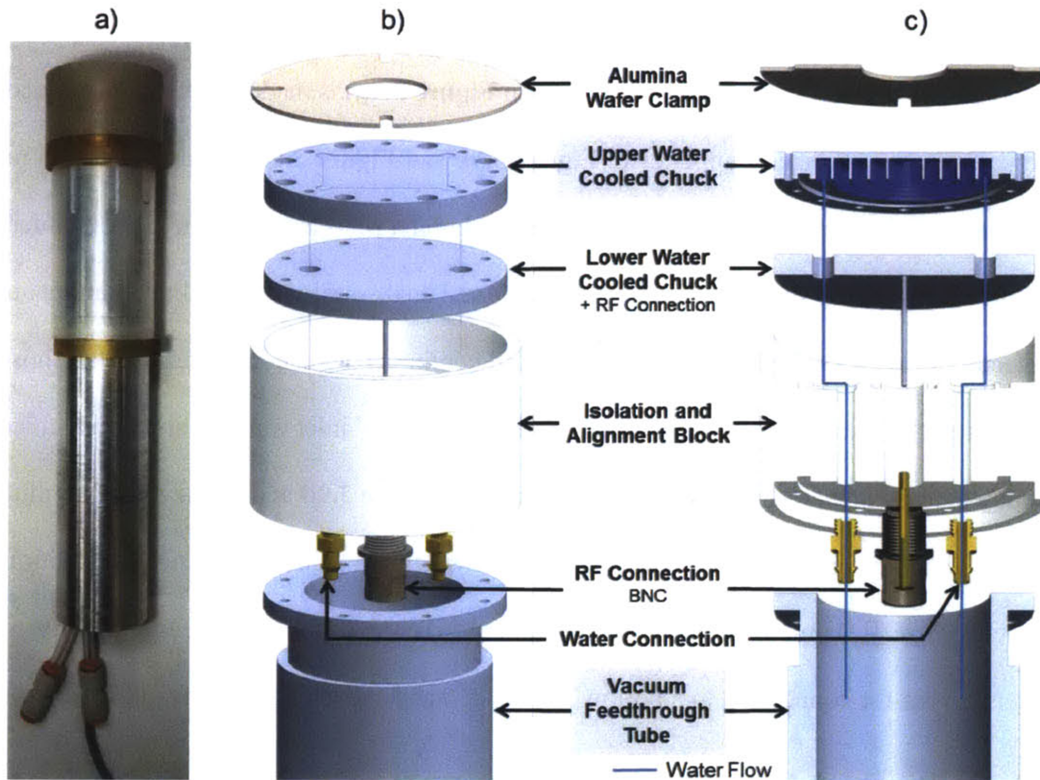

Figure 3.8: The chuck assembly. **Part a)** shows the actual assembly used the system, **b)** shows the assembly view of the components, and **c)** provides a cross-sectional view of each component. Individual components are described and shown in the text and subsequent figures.

The challenge to designing a chuck assembly that serves all of the purposes listed above is in integrating the various requirements of water-tightness, vacuum-tightness, and electrical isolation within a small form factor (the assembly diameter is 2.5" at the substrate end, and 2" at the tube end). The chosen design has three main parts: an RF-powered, water-cooled chuck and wafer registration piece, an insulating chuck alignment and isolation block, and a vacuum feedthrough tube. Special care is taken in the design to keep the water lines and RF connections isolated from vacuum and process conditions. This way, if a water leak or an accidental short circuit does occur, they happen at atmospheric pressure, which is both safer and easier to diagnose. That being said, this chuck design has not yet suffered any water or RF leaks. Each part of the chuck assembly is described in further detail below.

3.1.3.1 Water-Cooled RF Chuck

The water-cooled chuck itself (assembly view shown in **Figure 3.9a**) is made from two machined aluminum discs. The top surface of upper disc (**Figure 3.9b** and **Figure 3.9e**) has a wafer registration recess and threaded holes for the substrate clamp (a thin, alumina ring) to be attached. The underside of this disc (**Figure 3.9c** and **Figure 3.9f**) has a CNC machined dual spiral water cooling channel and o-ring groove for vacuum- and water-tightness. The dual spiral cooling channel configuration was chosen because it places each return "hot" water channel to next to a "cold" inlet water channel, which helps balance out any heat gradients. The bottom aluminum disc (**Figure 3.9d** and **Figure 3.9g**) completes the spiral cavity and contains openings for the inlet and outlet water connections. The RF connection to the chuck is made by a small stainless steel rod threaded into the center of the lower aluminum disc. This rod serves as the male pin for connection to a hollow female contact sleeve of a BNC feedthrough connector.

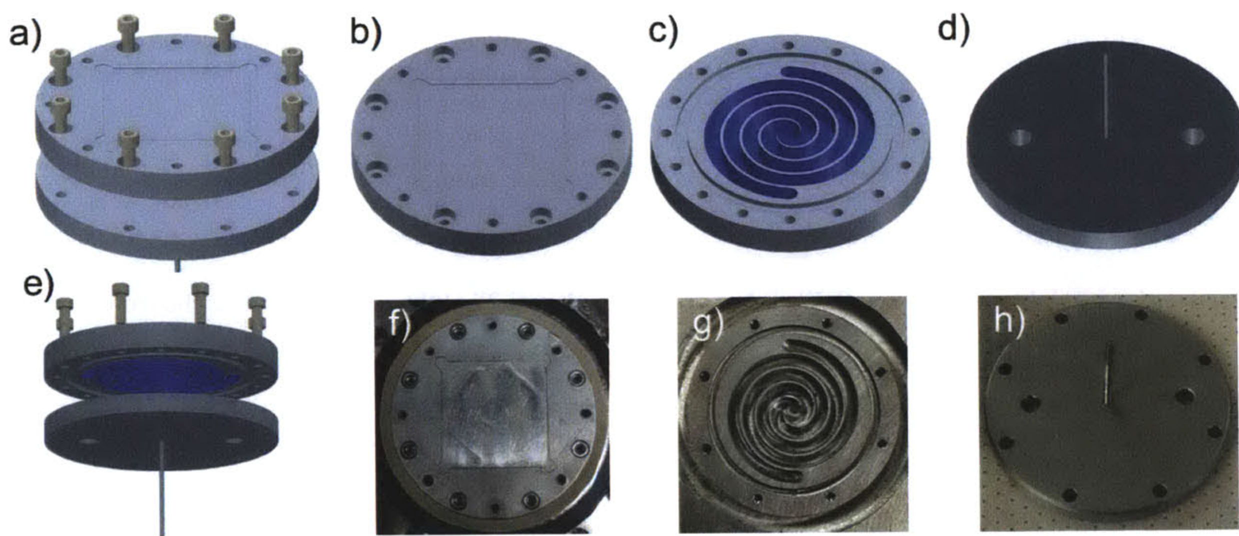

Figure 3.9: Water cooled RF chuck. **Parts a)** and **e)** show assembly views of the chuck pieces. **b)** and **f)** show the top view of the topmost piece, with the shallow recess for substrate registration. **c)** and **g)** show the underside of the topmost piece, which contains the dual spiral structure for the cooling water. Finally, **d)** and **h)** show the underside of the bottom piece, which features water entry/exit holes and the central RF connector pin.

3.1.3.2 Isolation and Alignment Block

In order to keep RF chuck electrically isolated from the other conductive (and grounded) pieces of the etcher, the structure shown in **Figure 3.10** was fabricated out of polyetheretherketone (PEEK), a high

density plastic PEEKwas the material chosen for this piece due to its combination of excellent tensile strength, high temperature resistance, good dielectric strength, and easy machinability. In addition to providing electrical isolation, this PEEK piece also has O-ring grooves (and the associated threaded holes for generating compression) to isolate the water and RF connections from the vacuum of the chamber. As mentioned earlier, this provides a safety barrier if a water leak or electrical short should occur. The bottom side of the PEEK piece has a 3/8"-24 threaded hole for the BNC feedthrough connector which attaches to the stainless steel rod of the RF chuck. The top side of this hole has a dedicated O-ring groove to prevent any water from leaking into the RF connection section. Also contained on the bottom of the PEEK piece are two 10-32 threaded holes for the water connectors, which each having their own integrated face-sealing O-rings to prevent leakage.

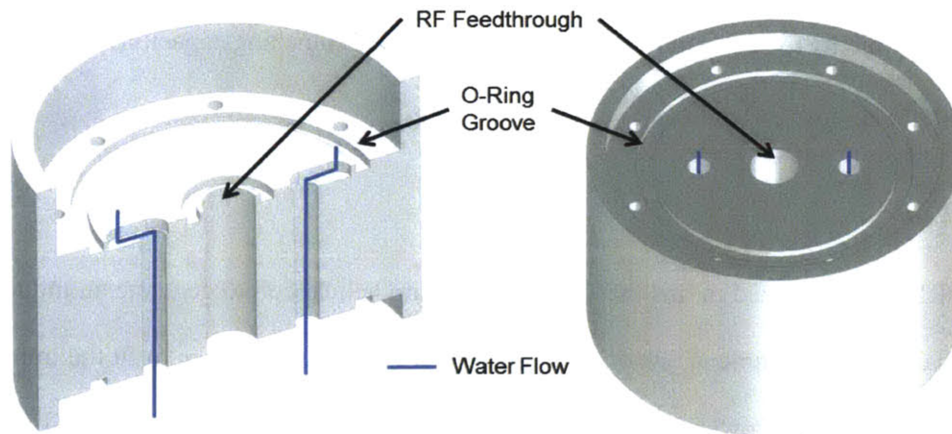

Figure 3.10: The chuck alignment and isolation block. **Part a)** shows a cut-away of the top view, with the path of the cooling water shown. **b)** shows the bottom view with the threaded holes for connecting the RF and water lines.

3.1.3.3 Vacuum Feedthrough Tube

The final piece of the chuck assembly (shown in the lower portion of **Figure 3.8a**) is an aluminum tube with an 8-hole sealing flange machined into the top end. The flange mates with the bottom side of the PEEK isolation piece and completes the vacuum seal isolating the RF and water lines by compressing an O-ring. Further electrical isolation is added to the chuck assembly by sliding a thin-wall Pyrex tube over the top portion of the aluminum tube. This Pyrex sleeve is held in place against the PEEK piece with a small spacer and a custom hose clamp. The overall length of the aluminum tube is just below 12" (300

mm), and the lower 8" (200 mm) has an outer diameter of precisely 2" (50.8 mm). This 2" OD allows the 2" compression port at the bottom of the lower chamber assembly to provide a vacuum-tight seal around the tube. The axial-sealing O-ring in the compression port allows the tube to be translated up and down without breaking vacuum. To set the desired chuck height and prevent the 14.7 psi (101 kPa / 760 torr) pressure difference between vacuum and atmospheric pressure from pulling the chuck assembly further into the chamber, two hose clamps are attached at the interface between the tube and compression port. To complete the chuck assembly, the water and RF lines extending from the bottom of the tube are connected to the chilled water supply and the substrate electrode RF generator.

3.1.4 RF Components

The 1" Fab DRIE uses an ICP-RIE configuration to generate and control the plasma used for etching. The primary components for this setup, the ICP coil and the RIE blocking capacitor, are described in the following section.

3.1.4.1 ICP Coil

The 1" Fab DRIE characterized in this thesis uses a two turn helical coil to generate an inductively coupled plasma. Given the dimensions of the chamber, two turns were chosen to fit the impedance matching range of the T&C Power Conversion AIT-600 matching network used. The coil itself was constructed from hollow copper tubing (0.25" OD, 0.18" ID) to allow for both electrical conductivity and water cooling[6]. To direct the RF power from the generator through the coil and not through the rest of the system, the electrical connections to the coil were made in an unbalanced fashion. The center pin of the Type-HN bulkhead connector used to deliver the coil power was connected to the exterior of one end of the coil tubing, while the grounded shield was connected to the protective metal enclosure surrounding the coil terminations. The "powered" end of the coil was connected to the cooling water supply with an

[6] The water is not affected by the 13.56 MHz RF power because the cutoff frequency for a circular, 0.09" (2.3 mm) radius waveguide with water as a dielectric is >10 GHz. ($f_{co} \approx \left(\frac{3\times10^8 m/s}{1.33*2\pi}\right)\left(\frac{p_{vn}}{0.0023\ m}\right) > 10\ GHz$, where p_{vn} depends on the waveguide mode and is between 1 and 10).

insulating bulkhead connector that passed through the metal enclosure. The other, "grounded" end of the coil was connected to cooling water return line with a metal bulkhead connector grounded to the protective enclosure. The use of a grounded metal enclosure and bulkhead fittings protects the user from accidental contact with the powered coil and also the cooling and power connections to be easily removed and reattached if the system is moved or peripherals are changed. A picture of the coil assembly is included in **Figure 3.11**.

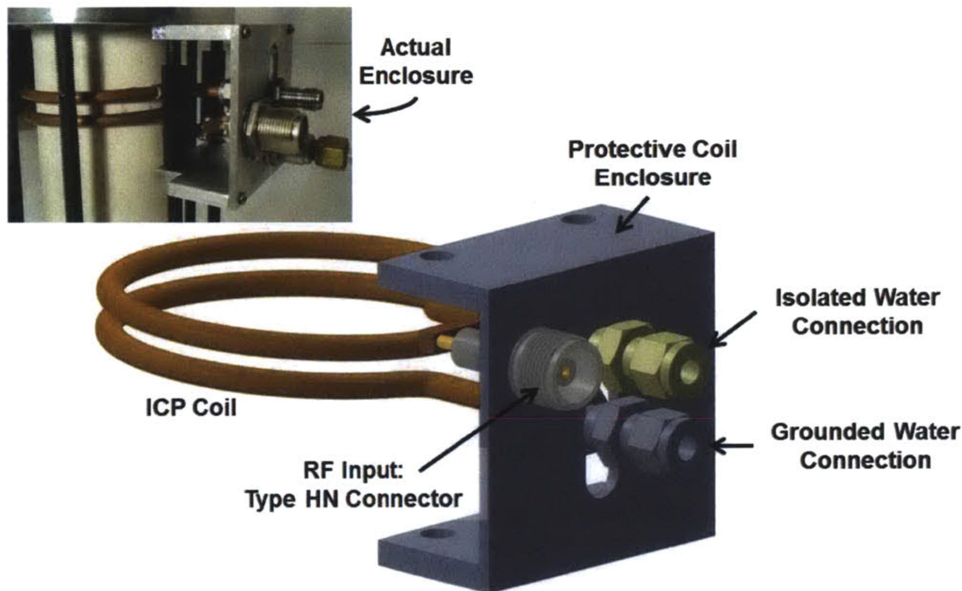

Figure 3.11: The coil assembly rendering shown with the mounting bracket. The actual coil assembly used on the etcher is shown in the upper left of the figure.

3.1.4.2 RF Capacitor for Substrate Electrode Blocking Capacitor

The RF power to the substrate electrode is coupled through a 500 pF capacitor to create the CCP-RIE configuration necessary for an accumulated DC bias to form and provide directionality to the ions within the plasma. The particular 500 pF capacitor used is a ceramic "doorknob-style" capacitor specifically designed to handle the large RF currents often encountered in plasma processing. The capacitor was fitted into a shielded aluminum housing (**Figure 3.12**) and connected in series between the substrate electrode and the corresponding RF generator.

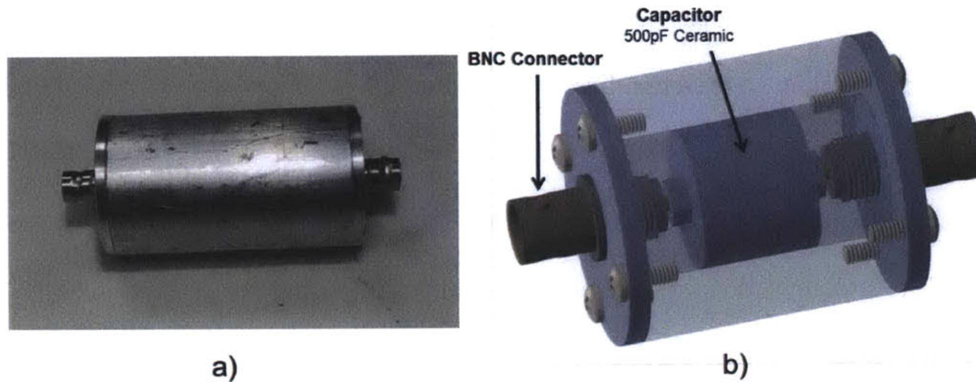

Figure 3.12: The blocking capacitor used for the substrate electrode. **Part a)** shows the actual capacitor assembly used, and **b)** shows a rendering of the assembly with the 500pF capacitor shown in the center.

3.1.5 Gas Distribution System

Uniformity is one of the primary requirements for nearly any piece of semiconductor fabrication equipment. In process gas-based equipment like the 1" Fab DRIE, uniformity is a function of several factors, including the geometry of the exposed substrate area, the localized substrate temperature, the electric fields from the applied RF bias, and the radial distribution (planes parallel to the substrate surface) of process gas in the chamber. This section is concerned with the last of these factors, the process gas distribution in the 1" Fab DRIE.

3.1.5.1 Gas Flow

In large-scale etching and deposition equipment, the distances between gas injection, plasma generation, and the substrate can be large enough to allow simple diffusion to distribute the gas radially across the process chamber. This reliance on diffusion breaks down when gas flows increase and the plasma-substrate spacing decreases, which are common processing tweaks to increase etch and deposition rates. To combat the resulting non-uniformity, equipment manufacturers employ gas distribution systems (commonly referred to as showerheads) to preemptively distribute process gases. The small length scales inherent to the 1" Fab DRIE (and the desire for high etch rates) present the same type of issues for gas distribution. The simplest gas showerhead design for a cylindrical chamber geometry like the system described here takes in process gas from an inlet at the center of the cylinder, splits it equally among

several radially extending tubes, and then dispenses it through apertures at a certain radius from the central point. Unfortunately, a central entry point is troublesome in practice, as several diagnostic and metrology tools (such as the Langmuir probe discussed in **Section 4.1.2**) also require access to the center of the top flange to make accurate measurements. This necessitates an eccentric placement of the process gas inlet. To create a radially uniform gas distribution from an off-center inlet, the principles of network analysis can be applied to a lumped element representation of the process gas delivery system [21]. From this lumped element representation, a direct analogy to an electrical circuit can be made. This analogy aids in the understanding of the underlying mechanisms and provides a simple way to diagram the elements of the system. **Table 3.1** provides a list of elements in the gas delivery system and their electrical equivalents and **Figure 3.13** shows a schematic of the effective process gas delivery system using these electrical analogs.

Gas Flow Quantity		Electrical Quantity	
Pressure	P	Voltage	V
Throughput	$\dot{Q}$	Current	I
Conductance	C	Resistance^{-1}	R^{-1} (or G)

Gas Flow Equations	Electrical Equations
$P = \dot{Q}/C$	$V = IR$ or $V = I/G$
$\sum \dot{Q} = 0$ at each junction	$\sum I = 0$ at each node

Gas Flow Element	Electrical Element
Tubing	Resistor
Regulated Gas Cylinder	Voltage Source
Mass Flow Controller	Current Source
On/Off Valve	SPST Switch
Three Way Valve	DPST Switch
Check Valve	Diode

Table 3.1: Analogs between the gas flow and electrical regimes.

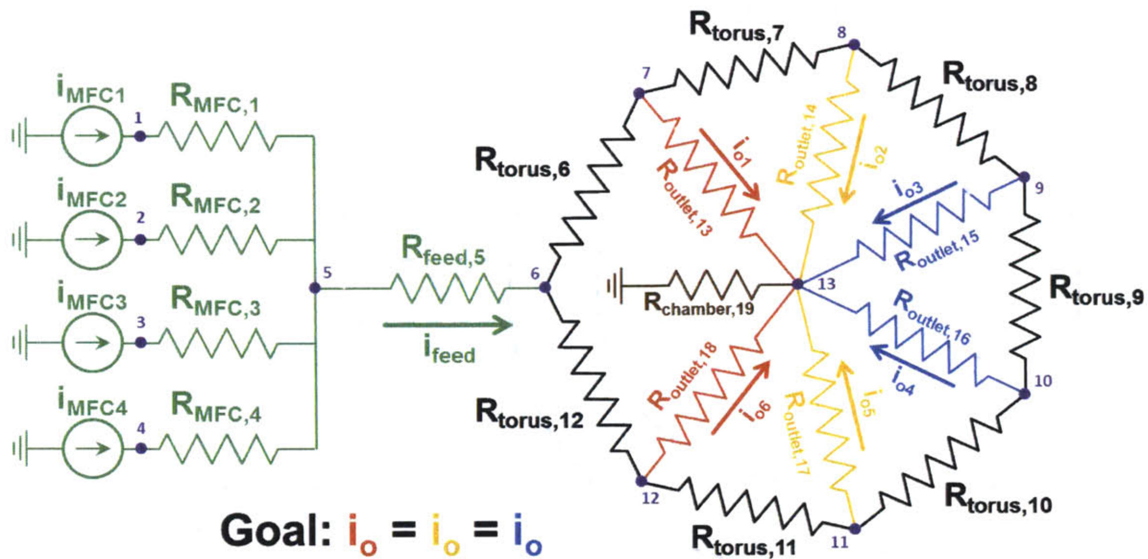

Figure 3.13: Electrical analog of the process gas delivery system. The ideal gas showerhead provides an equal amount of current through each of the six outlet resistors.

In a basic electrical circuit (i.e. only linear elements), Ohm's law and Kirchoff's current and voltage laws are all that is necessary to determine the node voltages and branch currents. Under certain conditions, gas flow systems can also be solved using linear methods. Unfortunately, the dimensions and pressures present in the 1" Fab process gas delivery system give rise to nonlinearities (with respect to pressure) in the conductance terms. These nonlinearities arise from the fact that gas molecules exhibit very different physical behavior as the pressure and geometry of their flow path changes. The different behaviors are commonly classified into one of three flow regimes (molecular, transitional, and viscous) using a dimensionless parameter known as the Knudsen number, which can be calculated using the formula below.

Flow Regime	Knudsen Number
Molecular	$Kn > 0.5$
Transitional	$0.01 < Kn < 0.5$
Viscous	$Kn < 0.01$

$$\textit{Knudsen Number} = Kn = \frac{\lambda}{d_c} = \frac{\eta}{P d_c}\sqrt{\frac{\pi R_0 T}{2 M_m}} \tag{3.1}$$

where:
λ = mean free path
d_c = characteristic dimension
η = viscosity
P = pressure
R_0 = gas constant
T = temperature
M_m = relative molecular mass

Table 3.2: Delineation of flow regimes using the Knudsen number formula.

In molecular flow, gas molecules collide with the walls of their environment more frequently than with other molecules (large mean free paths) and so the geometry of the environment becomes the most important factor in determining flow behavior. In the viscous flow regime, smaller mean free paths lead to more intermolecular collisions and thus the characteristics of the particular gas species and the total pressure become significant factors in the calculation of conductances. Transitional flow has elements of both molecular flow and viscous flow and is mostly treated with empirically derived formulas.

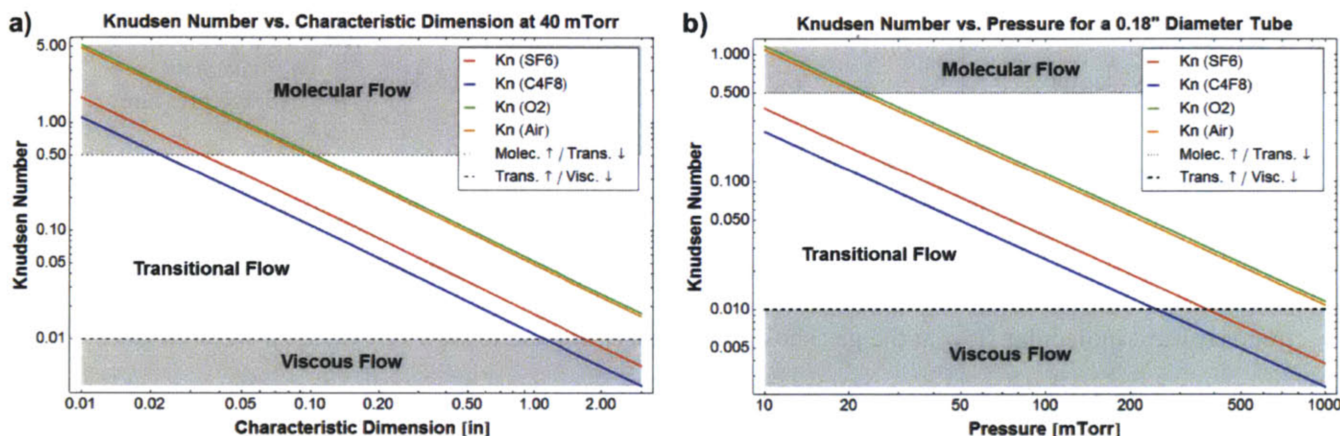

Figure 3.14: a) Kn vs. Pressure for common DRIE gases. **b)** Kn vs. Characteristic Dimension for common DRIE gases.

Figure 3.14 depicts graphically the relationship between the Knudsen number and pressure and the Knudsen number and characteristic dimension (the diameter for common flow elements like tubes and apertures) for the primary process gases used in the 1" Fab DRIE. As the plots and the Knudsen formula show, for a given tube dimension, a lower pressure pushes the flow into the molecular regime (and conversely, a higher pressure leads to a more viscous flow). Similarly, smaller tube dimensions exhibit more molecular flow behavior.

Each flow regime has its own equations for calculating the conductance of a particular tube geometry. The molecular regime generally has the most straightforward equations, as its conductances are independent of pressure. Conductances in the viscous regime depend on the average pressure (calculated as $P_{avg} = \bar{P} = \frac{1}{2}(P_{upstream} + P_{downstream})$) across the flow element. Transitional flow conductance formulas use a mix of molecular and viscous principles and often are fitted to empirical observations.

Table 3.3 shows conductance equations for long tubes in each of the three flow regimes. A complete list of flow equations used over the course of the flow system analysis can be found in **Appendix B**.

Flow Regime	Long Tube Conductance		where:
Molecular	$C_m = \frac{d^3}{3l}\sqrt{\frac{\pi R_0 T}{2M_m}}^{\dagger}$	(3.2)	d = diameter l = length R_0 = gas constant
Transitional	$C_t = C_v + \left(\frac{Kn + 1.253}{Kn + 1.548}\right) C_m$	(3.3)	T = temperature M_m = relative molecular mass Kn = Knudsen number
Viscous	$C_v = \frac{\pi d^4}{128\eta l}\bar{P}$	(3.4)	η = viscosity $\bar{P}$ = average pressure

†simplified expression valid only for l>>50d

Table 3.3: Conductance formulas for long tubes in each of the three flow regimes.

At the normal pressures and flow of the system, the transitional flow regime is the most common, with trends toward molecular flow at the gas showerhead apertures and toward viscous flow in the areas downstream of the showerhead. For the below analyses, tube conductances are calculated using the transitional formula (**Eqn. 3.3**), and aperture conductances are calculated using the molecular flow formula[7] found in **Appendix B**. These conductance expressions were then combined to form equations describing the flow in and out of each node.

3.1.5.2 Showerhead Simulation and Design

In order to solve the resulting system of nonlinear equations, a MATLAB script utilizing Newton's method for approximating roots to a function was compiled. Briefly, Newton's method consists of making an educated guess (p_k) at the root/solution (in this system, the pressures at each node, p_{actual}), and then using the Taylor series expansion about this guess to solve for an improved guess (p_{k+1}). By repeating this process with each newly calculated guess, better and better approximations to the real solution can be made. It should be noted that Newton's method is not a foolproof process, but with the

[7] While the Knudsen number suggests that the flow through the apertures falls into the transitional regime, approximations made using the empirical formula for transitional flow through apertures show deviation of less than 10% from the conductance found using the molecular formula. The exact formulas and estimations used are contained in **Appendix B**.

appropriate checks for false convergence and perturbation techniques to avoid settling in local minima or maxima, it is very efficient way to solve nonlinear systems of equations. The final solution is reached once the residual between consecutive guess falls below a preset tolerance value. The governing equations for Newton's method are included below.

$$F(p_{actual}) = 0 \tag{3.5}$$

$$Find\ the\ root\ of \quad \longrightarrow \quad F(p) \cong F(p_k) + \frac{\delta F(p_k)}{\delta p}(p - p_k) \tag{3.6}$$

$$0 = F(p_k) + \frac{\delta F(p_k)}{\delta p}(p_{k+1} - p_k) \quad \Rightarrow \quad p_{k+1} = p_k - \left[\frac{\delta F(p_k)}{\delta p}\right]^{-1} F(p_k) \tag{3.7}$$

The convergence tolerance for the flow system described here was set to 1×10^{-7} Pa (7.5×10^{-7} mTorr), which is 6-7 orders of magnitude lower than the pressures actually encountered, and provides far more precision than is easily measurable in the system. Once converged, the set of node pressures are then used along with the conductance values to find the mass flows for each branch of the system. Each run of the Newton's method solver takes ~1 second on a semi-modern laptop, and outputs the mass flow data both graphically and to a database of conditions and results.

The ultimate goal for this modeling effort is to produce a system where the mass flow dispensed from each of the showerhead outlets was equal, and the primary variable modified to achieve this goal were the diameters of the outlet apertures themselves[8]. For ease of fabrication, the possible sizes of outlets were restricted to standard drill bit sizes (#80 to #30 (including fractional sizes) from the ANSI drill bit sequence, and 1mm to 3.2mm (in 0.1mm and 0.25mm intervals) from the ISO Metric drill bit sequence). This provides 86 possible choices for outlet sizes. To assess the strength of a particular size combination, the variation amongst the outlet holes was tested over mass flows of 0.25 to 10 sccm, and with each of the common process gases deployed into the etch chamber. Considerations are also given to choosing sizes

[8] In order to validate the assumption that the showerhead outlets can indeed be treated as apertures, the median length (the apertures are drilled into a curved torus structure) of the outlets was kept to 25% of the outlet diameter. For example, the 0.055" (#54 drill) wide aperture was carefully countersunk until the median length was ~0.014".

that are large enough to avoid a significant pressure drop across the showerhead, yet not so large as to diminish the assumptions made about apertures leaving a cylindrical tube.

The final set of parameters chosen and implemented in the 1" Fab DRIE is included in **Figure 3.15**, as well as a plot of their performance for common process gases and potential gas flows.

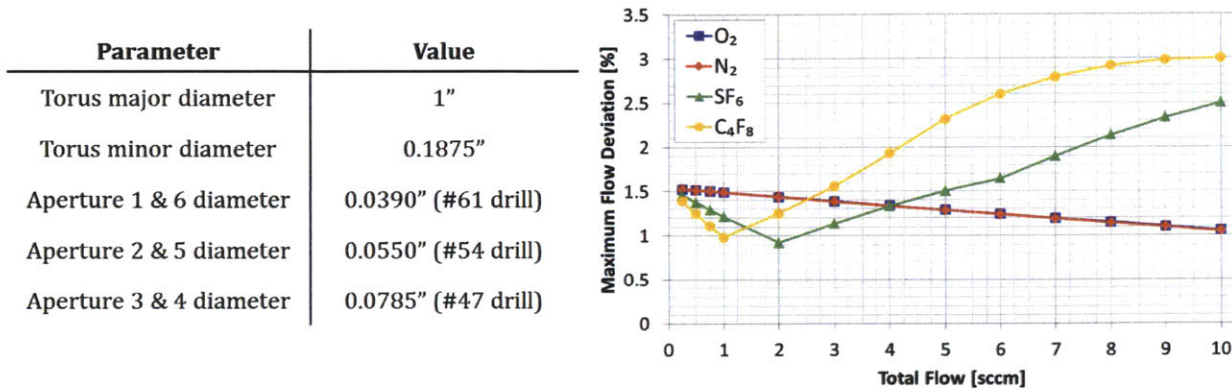

Parameter	Value
Torus major diameter	1"
Torus minor diameter	0.1875"
Aperture 1 & 6 diameter	0.0390" (#61 drill)
Aperture 2 & 5 diameter	0.0550" (#54 drill)
Aperture 3 & 4 diameter	0.0785" (#47 drill)

Figure 3.15: The parameters chosen for use in the gas showerhead and the maximum percent deviation between the flow from the six apertures for these parameter selections for several common process gases.

As the data shows, the selected outlet diameters perform quite well across the standard range of flows and process gases, with a maximum flow deviation of just ~3% at large flows of C_4F_8. This data however is just the deviation between the 6 outlet points within the etch chamber. To achieve a uniform radial distribution across the chamber, the 6 gas streams must diffuse outward. At normal processing pressures and gas flows, the diffusion coefficient for the process gases can be estimated from the mean free path and mean thermal speed of the gas molecules. In equation form, this approximation takes the form of:

$$\textbf{Diffusion Coefficient} = D = \frac{1}{3}(\lambda)(v_T) = \frac{1}{3}\left(\frac{k_B T}{\sqrt{2}\pi d_m^2 P}\right)\left(\sqrt{{8k_B T}/{\pi m}}\right)$$
$$= \boxed{\frac{2T^{3/2}}{3Pd^2}\sqrt{\frac{k_B^3}{\pi^3 m}}} \tag{3.8}$$

where:
λ = mean free path
v_T = mean thermal speed
k_B = Boltzmann constant
T = temperature
d_m = molecular diameter
P = pressure
m = absolute molecular mass

Evaluating this expression using a worst case estimate for pressure (100 mTorr) and gas type (C_4F_8, mass: 200 g/mol, diameter: 0.63 nm) gives a diffusion coefficient of ~0.01 m^2/s. This diffusion coefficient can then be combined with a residence time calculation to yield an approximate diffusion length within that residence. Again taking a worst case scenario and assuming a large flow rate of 5 sccm, the residence time for process gas in the chamber is 158 ms per 1 inch of chamber height ($t_{Residence} = PV/\dot{Q}$)[9]. In 158 ms, gas with a diffusion constant of 0.01 m^2/s travels on average $2\sqrt{Dt}$ in any given direction. This gives a diffusion length of 8.1 cm (3.2") per vertical inch of travel in the chamber. Since the chamber is only 2.85" wide and the 6 outlet points are spaced just over 1" apart ($2" \times \pi/6 = 1.047"$), it can safely be assumed that the gas flows will diffuse together to form a radially uniform distribution before they reach even the ICP coil (which for the characterization performed in **Chapter 4**, sat ~1" away from the gas showerhead).

3.1.6 1" Fab DRIE Control System

To operate modern fabrication equipment in a reliable and repeatable manner, automated, real-time control of many different types of systems is required. In addition, fabrication systems generally have ancillary and auxiliary systems that do not need automated control (or specifically should not be hooked into an automation system). For example, control of gas flow during a Bosch Process DRIE experiment needs automated control due to the short time scales and impracticality of a user switching the gas flows every few seconds. On the other hand, simple and infrequent tasks like adjusting a regulator on a process gas cylinder or safety measures like emergency stop switches do not need to be centrally controlled.

3.1.6.1 Manual Control Elements

The full 1" Fab DRIE system as characterized in this thesis has a combination of automated, real-time control and manual control of its equipment set. The automated elements are the mass flow controllers, the process gas manifolds, the RF generators for the ICP coil and the substrate electrode, and the

[9] The pressure dependencies of the diffusion coefficient and the residence time (Dt) actually cancel each other out (diffusion occurs faster at lower pressure, but lower pressures → faster residence times (for a given gas flow)).

matching network for the ICP coil. The manual elements are the process gas cylinders and regulators, the chilled water for the ICP coil and substrate chuck, the matching network for the substrate electrode, the vacuum isolation valve to the chamber, and the vent valve on the chamber. With the exception of the substrate electrode matching network, these manual elements do not have time-sensitive control requirements, which is the reasoning behind leaving them manually controlled. The substrate electrode matching network (described further in **Section 3.2.2**) occasionally needs a 5-10 second tuning at the beginning of a process. Future iterations of the 1" Fab DRIE may incorporate some of these manual elements into the automated section, but for the purposes of the prototype system being examined, nonessential items were not included.

To begin operating the 1" Fab DRIE, a user must perform several manual steps (basically turning on each of subsystems). A detailed standard operating procedure (SOP) can be found in **Appendix C**. Once a substrate is loaded into the etching chamber, the vacuum isolation switch (a physical double-pole, single-throw (DPST) switch) can be toggled on to begin pumping down the system.

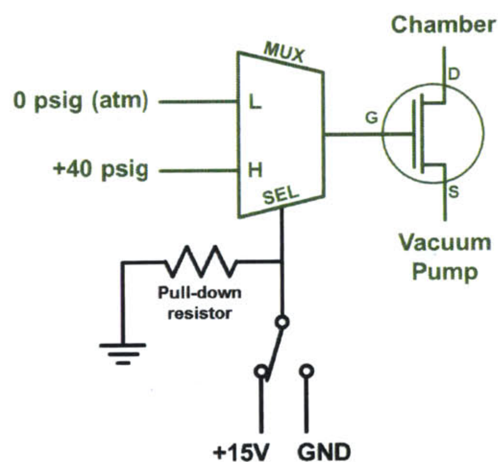

Figure 3.16: Electrical analog representation of the vacuum actuation scheme. Pneumatic components are shown in green, and electrical components are shown in black.

When the switch is turned on, a 15V voltage difference is created across the terminals of a normally-closed, three-way electronic solenoid valve (Clippard Instruments part #ET-3M-12, http://www.clippard.com/), causing it to open and allow 40 psig of clean nitrogen to flow to a normally-closed, pneumatically actuated vacuum isolation valve (GNB Corp. part #AN40,

http://www.gnbvalves.com/) separating the rotary vane pump and the etch chamber. The 40 psig of pressure causes the spring-loaded actuator in the isolation valve to open, and the pump begins to evacuate the chamber. When the chamber is to be vented, the vacuum isolation switch is turned off, eliminating the voltage difference at the three-way electronic valve. With no voltage difference across its terminals, the valve reverts to its default state of connecting the control line of the pneumatic isolation valve to atmosphere (0 psig). This causes the actuator of the isolation valve to spring closed, and the chamber is separated from the vacuum pump. The electrical analog representation of this vacuum actuation scheme is depicted in **Figure 3.16**. This physical, hard-wired approach to controlling the evacuation of the chamber is inexpensive (~$30 in total parts plus the isolation valve), prevents any unintentional venting or evacuation from software glitches, reverts to a safe operational state (the vacuum is isolated from the chamber) in the event of a power failure within the switch or electronic valve, and allows the user to quickly and conveniently toggle the vacuum state of the chamber.

3.1.6.2 Automated Process Control

With the chamber evacuated, control of the 1" Fab DRIE switches to the *Etch Recipe and Controller (ERAC)* software. This graphically-based software controls the state of the process gas manifold, the mass flow from each of the mass flow controllers, and the RF power delivered to the ICP coil and substrate electrode. The ERAC software also monitors the state of the mass flows and RF powers, allowing the user to monitor each of the current operating conditions from a central location. Screenshots of the software are shown in **Figure 3.17**.

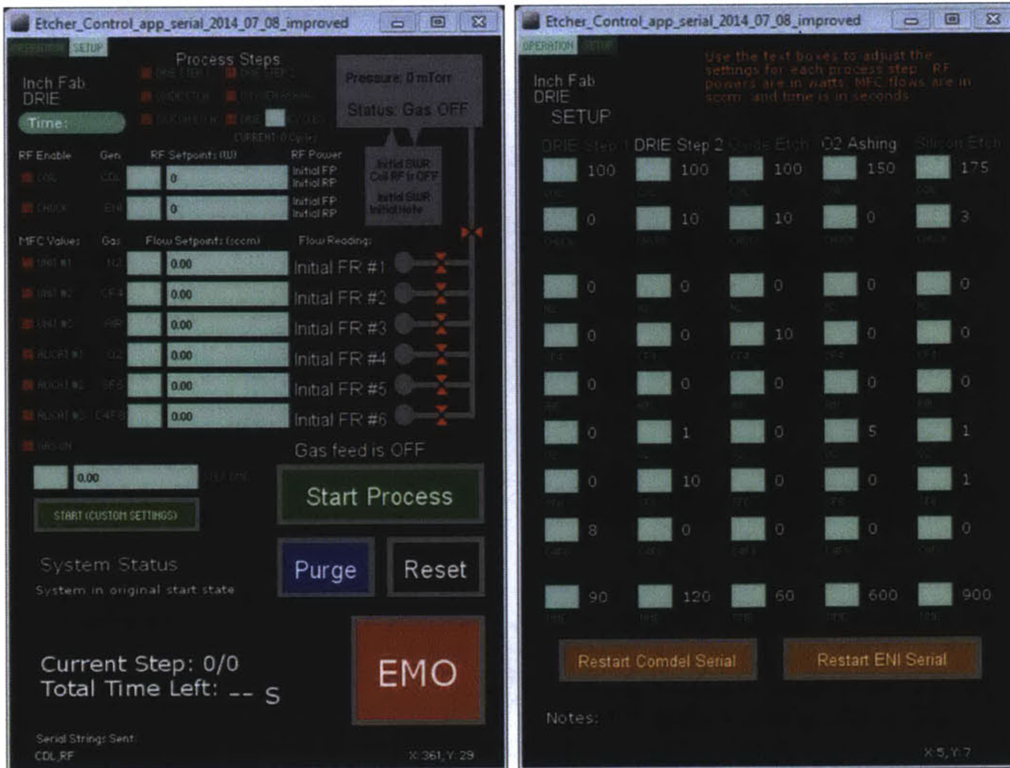

Figure 3.17: Screenshots of the Operation and Setup tabs of the ERAC software.

The graphical interface of the software is split into two pages or tabs. The "Operation" tab shows the status of the system and allows changes in parameters through a series of text boxes and sliders. Software-defined limits prevent a user from choosing values beyond the capabilities of the system. At the top of the tab one of the five user-defined recipes or a sequence of DRIE cycles can be selected. Selecting one of the recipes loads in the RF and gas flow setpoints, and then turns on the appropriate valves to allow the process gas flow to enter the chamber. The RF Generators are not enabled until the "Start Process" button is pressed. The "Start Process" button also begins the process timer, which displays the current process step (for multistep processes) and the time remaining. The "System Status" message box provides information about recent process or parameter changes. Several common functions are included as large buttons near the bottom right quadrant of the tab. The "Purge" button turns off all RF power, zeroes any RF power setpoints, zeroes all the MFC setpoints, and begins a two step gas purge process.

1. (20 seconds) Evacuate the chamber with the manifold exit valve and the manifold valve of any MFC used in previous processing open.
2. (20 seconds) Close any open MFC manifold valves and evacuate with just the manifold exit valve open.

After the 40 seconds have elapsed, the manifold exit valve is closed and the system returns to its default "off" state.

The "Reset" button turns off all RF power, closes all manifold valves, and then zeroes all RF and MFC setpoints. This is useful when a user wishes to "reset" all of the settings for the system, but it should be noted that if any MFCs were delivering gas to the chamber when the "Reset" button is pushed, some amount of process gas will remain trapped between the near-instantly closed manifold valves (actuation times of 5-10 ms) and the slower MFCs (zeroing times on the order of 1 second). This excess gas will be delivered to the chamber the next time the MFC valve is opened, leading to temporary pressure bumps. If gas is being flown and a user wishes to reset all of the current setpoints, the "Purge" button is a better, albeit slower option.

The "EMO" button includes all of the function of the "Reset" button, but additionally it severs the serial connection to the RF generators, which, through internal interlocks on each RF generator, ceases any RF output and zeroes all setpoints. The most potentially damaging and dangerous accidents or miscues in the 1" Fab DRIE deal with inadvertent emission of or exposure to RF radiation, and so this button, as the name indicates, serves as the software-level emergency stop. The serial connections to the RF generators can be reestablished through buttons on the "Setup" tab. Hardware-level emergency stops exist for each RF generator.

The "Setup" tab is where processing recipes are crafted. There are five recipe slots, and while they each have names describing their general purpose, there are no restrictions on the setpoints for any of the recipes. The DRIE Step 1 and DRIE Step 2 columns can be run sequentially multiple times (i.e. Step 1,

Step 2, 1, 2, etc.) using the cycles text box in the "Process Recipes" section of the "Operation" tab. Again, software-defined limits prevent a user from choosing values beyond the capabilities of the system. Also found in the setup tab are buttons that allow the restarting of the serial link to each of the RF generators, which are halted if the system has undergone an emergency stop sequence.

The software for the ERAC GUI is written using the Processing language and programming environment and makes use of the Serial library (a stock Processing library) for communication to the microcontroller and the ControlP5 library (GNU licensed by "sojamo") for the graphical control elements. Processing code, known as "sketches", contain two primary functions, setup() and loop(). The setup() function runs once at the beginning of a sketch's execution, and then the draw() function loops continually until the application is closed or stopped. In the ERAC software, the setup() function initializes all of the graphical and UI elements, and the draw() function handles all of the process timing and status updates from the RF generators and MFCs. User interaction is handled through "ControlEvents", which serve basically as interrupts that are triggered on changes from any of the buttons, text boxes, sliders, or virtually any other UI element. Each element has a unique identifier that allows the controlEvent() function (the "interrupt service routine") to respond properly to the change. ControlEvents can trigger other ControlEvents, allowing a single user action to cause a series of changes to the etching system, such as loading an etch recipe (from the radio buttons in the "Process Recipe" section described above) or quickly shutting down the system (the "Reset" or "EMO" buttons). The code is written in a modular fashion and oriented around the end actions rather than device-specific sequences, which provides flexibility and extensibility if there are changes or additions in the equipment used.

The ERAC software is contained wholly on the host computer, and so to interface with the components in the 1" Fab DRIE, a microcontroller is used. The microcontroller chosen for this task was a Teensy 3.1 (https://www.pjrc.com/). The Teensy 3.1 was chosen over other microcontrollers and single-board computers like the Arduino, BeagleBone, or Raspberry Pi because of its combination of performance (a 32-bit ARM Cortex-M4 running at 72 MHz with 64 kB of RAM), features (three hardware serial ports

and 34 general purpose I/O pins), cost (less than $20), and usability (it can be programmed using the Arduino integrated design environment (IDE)). The ERAC software communicates over a USB serial link to the Teensy, which parses and interprets the serial commands and sends them to the appropriate hardware serial ports (one port is reserved for the ICP coil RF generator, the second is assigned to the substrate electrode RF generator, and the third is used for the MFCs). Serial communication was chosen over analog communication to minimize the effect of noise, which can be a significant factor when the control signal connections to components require several feet of cable, and are being run through an environment that includes two high power RF generators and two RF matching networks.

The serial interfaces for the RF generators and the mass flow controllers used in this thesis employ the RS232/EIA232 communication standard [10]. RS232 is very common, but it requires both positive and negative voltage levels for its serial transmit (TX) and receive (RX) lines (per the specification, +3 V to +15 V for high levels and -3 V to -15 V for low levels), meaning that level shifting from the Teensy's 3.3 V logic levels is necessary. This shifting is accomplished using MAX3232 ICs, which feature internal charge pumps (driven from small externally connected capacitors) to achieve the necessary voltage levels (typically about -8 V to +8 V). The typical use case for RS232-based serial communication involves two devices, a piece of Data Terminal Equipment (DTE) and one piece of Data Circuit-terminating Equipment (DCE). These distinctions deal mainly with the pinout of the serial connector, such that a DTE device can connect to a DCE device with a standard, straight-though cable (typically terminated with DE-9 or DB-25 connectors). Serial ports on a computer are typically DTE and serial ports on peripheral devices are often DCE[11]. Sharing an RS232 serial line between multiple devices (known as "multi-drop") is not possible without extra hardware. Commercial solutions for multi-drop RS232 generally add extra hardware in the form of converters that translate the RS232 signal levels and pinouts to a protocol geared

[10] RS232 is an aged, but ubiquitous communication standard. Nearly all semiconductor peripherals sold have at least the option to use RS232 for communication of control and readback signals.
[11] Instances where 2 DTE or 2 DCE devices wish to connect are common enough that cables and adapters that natively cross the appropriate signal lines are readily available. These are known as null modem cables or adapters.

toward multiple device communication like RS485 or DeviceNet[12]. However, since the Alicat MFCs can be configured with different serial identifiers, a more elegant and far less expensive technique can be used to share the Teensy's third serial port (the schematic of the solution is shown in **Figure 3.18**).

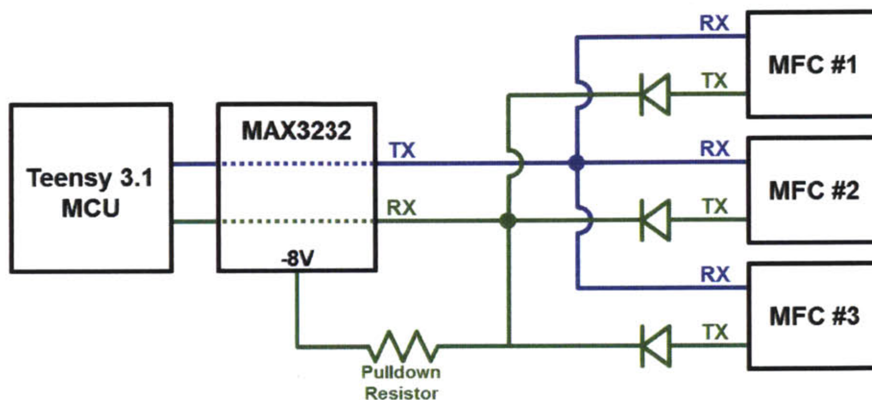

Figure 3.18: Schematic of diode auctioneering circuit used to control three RS232 MFCs using a single RS232 TX/RX pair.

Alicat MFCs are programmed to listen only for commands beginning with the specific identifier assigned to them. Other commands are simply ignored. This makes the transmit (RX from the MFCs) side of the communication very simple, as a single RS232 TX line can be connected directly to the RX lines of all the MFCs. The receive (TX from the MFCs) side is slightly more complicated. RS232 TX lines are held at the low (negative) voltage level when not in use, and so if the TX lines from each of the Alicat MFCs are connected together, when one attempts to transmit a message, it will be competing against the TX lines from the other MFCs, which are still trying to maintain the low voltage level. To get around this, a technique called diode auctioneering is employed. By connecting a simple diode (the archetypal 1N4148 small signal diode works well) between the TX line of each MFC and a common RX line on one of the MAX3232 converters, whenever one MFC attempts to transmit a message, the diode will let the high signals through to the MAX3232, and the other diodes will protect the other MFC TX lines. A 10 kΩ pull-down resistor (pulled down to the negative RS232 voltage level) is connected to the MAX3232 RX line to keep its value low when not being asserted high by an MFC TX line. As long as only one MFC

---

[12] The semiconductor industry uses a variety of industrial communication protocols for controlling multiple pieces of equipment, including the CAN-based DeviceNet and the RS-485-based Profibus and Modbus. However, all of these protocols generally require more expensive hardware to implement and add additional complexity on the software.

attempts to transmit at a time (which can be controlled via software, as the MFCs only transmit when told to so to), this diode auctioneering technique is an effective way to share an RS232 line.

The final piece of work done by the microcontroller is the control of the gas manifolds. The two-way valves (Clippard Instruments part #EC-2M-12) on the gas manifolds require at least 12 V and ~50 mA of power to actuate. This is more power than the Teensy can handle on its own (Teensy pins are capable of sourcing 9 mA recommended and 25 mA at absolute maximum, and at just 3.3 V), and so a Darlington transistor array (ULN2803) is employed. The ULN2803 has 8 Darlington drivers that each can supply up to 500 mA at 50 V (collector-emitter voltage) and can be switched easily by the 3.3 V logic of the Teensy. This allows each Clippard valve to be controlled by a single I/O pin on the Teensy, which is very simple to implement and provides an easy path to expansion as additional valves are added to the system.

A full circuit diagram for the control hardware can be found in **Appendix D** and the ERAC source code is available upon request.

3.2 Component Selection and Scalability

In addition to be being smaller and mechanically simpler than large etching equipment, one of the advantages of the 1" Fab DRIE is that it requires smaller input quantities to function. The basis for these savings and their effect on the selection of external peripherals and components are discussed in the following sections.

3.2.1 RF Generators

The first of the major external components required for the 1" Fab DRIE are the two RF generators for powering the ICP coil and the RIE substrate electrode. These generators are basically large power supplies that supply a user-selectable amount of RF power to a load. The most common RF frequency used for these generators (and the one used herein) is 13.56 MHz, which is a reserved industrial, scientific, and medical (ISM) radio band frequency. At this high frequency, as mentioned in **Chapter 2**, only the lightweight electrons can respond quickly enough to follow the oscillating electric field, whereas

the more massive ions only follow the accumulated DC bias on the substrate electrode. Once these accelerated electrons have initiated a plasma discharge, the power required to sustain the discharge scales with the surface area of the chamber. To sustain a discharge, the RF power absorbed by the plasma **(Eqn. 3.9)** must equal the power dissipated by the electrons **(Eqn. 3.10)**. This can be explained as follows: when electrons collide with process gas molecules, ions are generated. The energy associated with these ions is lost when they collide with the walls of the chamber. The power dissipated by the electrons is therefore directly proportional to the energy loss of the ions to the walls of the chamber which is directly proportional to the surface area of the chamber.

$$P_{abs} = \frac{1}{2} A_{plasma} Re(E * \mathcal{J}) \tag{3.9}$$

$$P_{dis} = n * u_B * A_{eff} * \epsilon_{T_e} \tag{3.10}$$

$$P_{dis} = P_{abs} \tag{3.11}$$

where:
E = Complex amplitude of RF Electric Field at Surface of Plasma
$\mathcal{J}$ = Amplitude of Surface current
n = plasma density
P_{diss} = power dissipated by electrons
u_B = Bohm Velocity (rate of electron-ion pairs lost in plasma sheath)
A_{eff} = Effective Surface Area of Plasma
ϵ_{T_e} = Energy loss per electron-ion pair created

The surface area of the commercial STS Multiplex ICP DRIE (which processes single substrates up to 6" (150 mm)) is roughly 630 in^2 and uses a 2 kW RF generator to power its inductive coil . The surface area of the 1" Fab DRIE chamber is approximately 6 times smaller at 95 in^2, and as a result, the ideal peak power for the coil generator falls around the 300 W range. Unfortunately, the large RF power requirements for most commercial plasma generation equipment have disincentivized the manufacture of low power RF generators. In the MHz range, 600 W is the lowest power RF generator that is still widely available. A few options at the 300 W range exist, but these offer no significant price break from the 600 W models.

As outlined in **Section 2.3,** the ICP-RIE system of plasma generation and control employed in the 1" Fab DRIE requires two separate RF power sources (one for the ICP coil and one for the RIE substrate electrode). The two generators used during this thesis work were both 600 W models: a Comdel CX600AS (Comdel, http://comdel.com/) for the coil and an ENI OEM-6B (MKS Instruments, http://www.mksinst.com/) for the substrate electrode. Despite their 600 W capabilities, the actual powers employed though never surpassed 250 W for the coil generator and 25 W for the substrate generator. Its unnecessary power output capability notwithstanding, the Comdel generator has several favorable attributes that made it a good fit for the 1" Fab DRIE. First, the Comdel has both analog and serial remote interfacing capabilities. This allows for easy control and monitoring of the generator's status from a central command location like the ERAC software described in **Section 3.1.6**. Secondly, the Comdel is air-cooled rather than water-cooled, which eases facilities requirements. Air-cooling is an advantage exclusive to low power generators, with water-cooling a requirement for nearly all generators larger than 1 kW. The last advantage of the Comdel generator concerns a nuance in the way it handles power setpoints. When the Comdel is given a setpoint for the power to deliver into its load, it maintains that power (known generally as "forward" power) regardless of the state of the load. In RF power delivery, impedance matching between the source and the load is crucial (the following section deals with this very issue). Impedance mismatches lead to some of the delivered power being reflected back from the load into the source (This is known as "reflected" or "reverse" power and can be severely damaging to the generator). If 100 W is supplied from the generator to the load and an impedance mismatch causes 20% (20 W) of this power to be reflected back, the load only receives 80 W of power. To get around this, the Comdel measures and compensates for any power reflected back by increasing its power output. In the previous example, the Comdel would increase its power output to 125 W, so that when 20% (25 W) is reflected back, 100 W is still delivered to the load. To avoid having to generate this extra power, impedance matching circuits are used to minimize mismatches between the source impedance (50 Ω in standard RF generators) and the load impedance. Impedance matching however is not a perfect or an

instantaneous process, and so the Comdel's ability to maintain a constant forward power to the load despite any small or temporary mismatches is very useful.

Unfortunately, the ENI OEM-6B generator used for the substrate electrode does not share all of the advantages of the Comdel CX600AS. It is twice the weight of the Comdel generator, takes up ~50% more space, is not rackmountable, requires at least 0.8 gallons per minute of water-cooling, and does not compensate for reflected power. It does however have analog and serial remote interfacing options, making it simple to integrate with the ERAC software. The OEM-6B generator was used for this iteration of the 1" Fab DRIE primarily because it was available, but in a commercial system, it would be replaced with a smaller, more modern generator.

While the ENI generator functions just fine for supplying power to the substrate electrode in the current iteration of the 1" Fab DRIE, it is worth noting that the lack of availability of low power or low cost RF generators appears to be a market problem and not a technological one. Given the mature state of solid-state power semiconductor technology, the design and construction of a simple, inexpensive transistor amplifier that could provide, at the very least, the tens of watts required by the substrate electrode is a very reasonable proposition. In addition to the cost savings over a traditional RF generator, these power supplies would certainly be air-cooled and could be powered through standard 110 V outlets (rather than the 220 V/20 A outlets required by normal 600 W generators) and exist in a substantially smaller form factor than higher power generators. Other features found in today's higher end (and thus higher power) RF generators like impedance matching via operating frequency modulation could potentially also be implemented.

3.2.2 Matching Networks

The RF generators described above have output impedances of 50 Ω, and thus transfer power at maximum efficiency when connected to a 50 Ω load. While in use, the ICP coil, substrate electrode, and chamber environment (including the generated plasma) have reactive (both capacitive and inductive)

impedance elements that must be negated in order to reach a fully real 50 Ω load impedance. This negation occurs through the use of impedance transformation circuits known commonly referred to as matching networks (as they "match" the load impedance to the source). Because the load impedance is a function of the chamber environment, which is not static, active impedance matching is required. This is achieved by monitoring the relative phases of the forward and reflected powers and then adjusting variable capacitors and inductors within the matching network to minimize any impedance mismatch.

The most important variable in impedance matching is the impedance of the plasma itself. The plasma impedance depends on process conditions such as pressure, process gas composition, chamber geometry, and the state of the substrate being etched. For systems generating plasma using an ICP coil (like the 1" Fab DRIE), the load impedance (Z_S) is often modeled as a transformer [22]. **Figure 3.19a** displays this model. For the purposes of analysis, the transformer model can be simplified into the model shown in **Figure 3.19b**. This reduced model and its relevant equations, **Eqn. 3.12-3.14**, show that the load impedance is heavily dependent on the chamber configuration and the plasma conductivity (which itself is dependent on the plasma density and process gas mass).

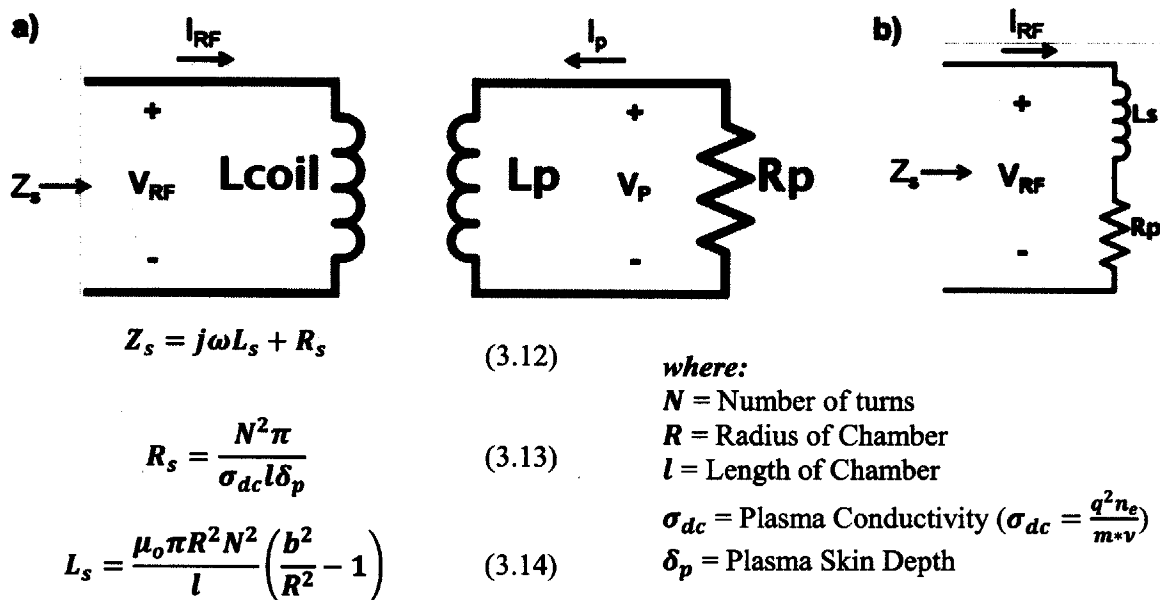

$$Z_s = j\omega L_s + R_s \quad (3.12)$$

$$R_s = \frac{N^2\pi}{\sigma_{dc} l \delta_p} \quad (3.13)$$

$$L_s = \frac{\mu_o \pi R^2 N^2}{l}\left(\frac{b^2}{R^2} - 1\right) \quad (3.14)$$

where:
N = Number of turns
R = Radius of Chamber
l = Length of Chamber
σ_{dc} = Plasma Conductivity ($\sigma_{dc} = \frac{q^2 n_e}{m*v}$)
δ_p = Plasma Skin Depth

Figure 3.19: The transformer model for modeling plasma impedance. The circuit in **a)** can be simplified to **b)**, which can then be analyzed using **Equations 3.12-3.14.**

In order to match the impedances in the model of **Figure 3.19b**, several different circuit topologies have been developed [23]. Three of the most common topologies are, L, Pi, and T which are shown in **Figure 3.20**. L networks are the most commonly used networks because they require the least amount of components and subsequently the simplest control algorithms. In L networks however, impedances can only be tuned in one direction. In the L network shown in **Figure 3.20a**, the network can only match loads greater than 50 Ω and if the L network is flipped the network can only tune impedances less than 50 Ω. Pi and T networks on the other hand can match impedances both ways as they are combinations of two L networks. Pi and T networks however require more components and thus more complex tuning algorithms.

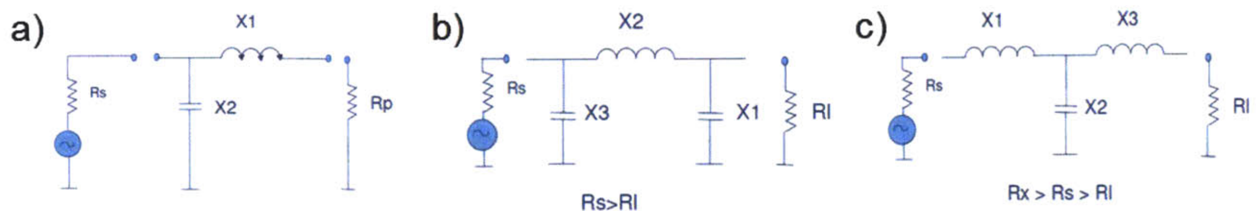

Figure 3.20: Matching network topologies. **Part a)** shows an L matching network circuit topology, **b)** shows a Pi matching network circuit topology, and **c)** shows a T matching network circuit topology. Circuit diagrams courtesy of Applied Materials [23].

Each of the two RF sources in the 1" Fab DRIE requires a matching network. The Comdel CX600AS generator used to power the ICP coil uses a T&C Power Conversion AIT-600 L-type auto-matching network (T&C Power, http://www.tcpowerconversion.com/). The AIT-600 was chosen because it is specifically designed for impedance matching in ICP systems. As mentioned in **Section 2.3**, ICP plasmas have two distinct regions of operation: E-mode (low plasma density, low power) and H-mode (high plasma density, high power) subsequently the matching network must be able to match the impedances both of these regions. In order to deal with this combination of requirements, a matching network for ICP systems must use very robust components like variable vacuum capacitors and Type HN or 7/16" DIN connectors (the AIT-600 uses HN connectors). The abrupt change between the two operating modes also adds the necessity of auto matching to keep the impedance tuned between the two operating modes.

To provide impedance matching for the ENI OEM-6B generator powering the substrate electrode, a manual Heathkit SA-2060 antenna tuner was used. This Heathkit tuner was originally manufactured for tuning ham radio antennas, but the same principles apply to CCP-RIE electrodes (which are, in essence, just a different type of antenna). The Heathkit has the advantages of being very inexpensive (less than 10% of the cost of the AIT-600), yet still using quality components[13]. The Heathkit supports powers up to 1 kW, which more than qualifies it for use with the substrate electrodes powers of up to 25 W. A T-network topology is used in the Heathkit, which allow it to tune a large range of impedances, including those found in the 1" Fab DRIE. The range of substrate electrode impedances encountered during operation was quite small, and near perfect matching could generally be achieved in just a few seconds with small adjustments to the components values. Unlike the ICP coil, once matched, the substrate electrode impedance was reasonably insensitive to changes in the etching environment, like the process gas switching that occurs in Bosch Process etching. This ease of matching was an important factor in deciding to use the cheaper, but manually tuned Heathkit.

The rapid gas switching of Bosch Process DRIE poses an additional challenge for matching networks. As alluded to above, different process gases result in different plasma impedances, and the transition between gases can also produce a unique impedance. Typical Bosch Process step times are on the order of 5-15 s, meaning that any impedance matching must be performed very quickly to avoid a significant loss of energy transfer to the chamber. In order for the standard impedance matching procedure (using servo or stepper motors to adjust variable capacitors) to keep up with these fast switching demands, advanced control algorithms and predictive tuning[14] must be employed. For high-speed Bosch Process recipes (step times from 100s of milliseconds to a few seconds), other methods of impedance matching have been developed. One of these new methods involves using large arrays of capacitors and relays to achieve a near continuous range of tuning values, but still have the ability to quickly switch between high and low

[13] The adage of "they don't make them like they used to" definitely applies to Heathkit antenna tuners.
[14] Predictive tuning methods include presetting the capacitor positions based on previous match conditions and then refining the tuning based on the actual impedance, and also storing particular impedance patterns and the resulting matching settings for quick recall and adjustment.

capacitance values. Combined with predictive tuning methods, these capacitor/relay arrays can tune varying load impedances very quickly [24]. A second tuning method eliminates a matching network altogether and instead matches the load impedance by varying the frequency of the RF output signal. This feature is available on newer, high-end RF generators and works because the reactive components of the load impedance are frequency dependent. By shifting the frequency of operation, these reactive elements can be effectively transformed into real elements and thus eliminate any reflected power from an impedance mismatch. This method can lead to ultra-fast matching times, but often limited frequency tuning ranges limit the range of tunable impedance to less than tuning ranges achievable with conventional matching networks [25,26].

3.2.3 Vacuum Pumps

As mentioned during the discussion of Paschen's Law in **Section 2.2**, the millitorr range of pressures (1-1000 mTorr) are optimal for striking and sustaining a plasma. Lower pressures reduce the number of collisions that ionize the process gas molecules and higher pressures make it difficult for electrons to gain enough to ionize a gas molecule upon collision.

Fortunately, this pressure range is easy to achieve for a number of different types of vacuum pumps. The most common vacuum pumping system found in commercial plasma etching systems is the turbo pump. While there are a variety of sub-classes with the turbo pump family, their primary mechanism for pumping is a high speed motor (50,000 to 100,000 RPM is common), which uses either a collection of rotors containing angled blades (turbomolecular pumps) or a flat tube rotor positioned closely to a helically spiraled wall (turbo drag wall). The rapidly spinning rotors impart a net momentum to gas molecules away from the pump inlet and toward the pump exhaust. An illustration of a turbomolecular pumps is shown in **Figure 3.21b**. Once started, they are capable of achieving pressures down to 10^{-10} or 10^{-11} Torr, but they cannot begin pumping down from atmosphere. At atmospheric pressures, the mean free path of a gas molecule is ~100 nm, which is much smaller than any gap that can be reasonably maintained between the spinning rotors and the stators or walls. Therefore, any momentum transfer to a

gas particle imparted by these rotors will be largely negated by collisions with other molecules before a second rotor collision can occur. For this reason, turbo pumps require a small "backing" or "roughing" pump that provides a low enough base pressure (requirements range from tens of millitorr to tens of torr, depending on the specific turbo pump) to increase the mean free path enough for effective momentum transfer. **Figure 3.22b** shows the relative pumping speed of a turbo pump versus the inlet pressure. The large pumping speeds (even at low pressure) offered by a turbo pump allows it to maintain low pressures even when large amounts of process gas are injected. For commercial plasma etching systems that require these large gas flows, a turbo pump is essential. The smallest (and least inexpensive) turbo pumps sold by most manufacturers offer rated pumping speeds on the order of 60 L/s (127 ft^3/min). For the small volumes and process gas flows inherent to the 1" Fab DRIE, these pumping speeds are more than adequate to reach and maintain process pressures in the range of 1-100 mTorr[15]. Unfortunately, like RF generators, the prices of small turbo pump systems are not appreciably cheaper than their larger counterparts. However, the complexity of a turbo pump and the precision required to manufacture it does not diminish with decreasing size, and therefore it is very difficult to imagine a scenario like the RF generator where this price disparity could be overcome by simply making a smaller turbo pump.

[15] In fact, even the smallest turbo pump systems will likely need to be throttled to raise the operating pressure to the millitorr range.

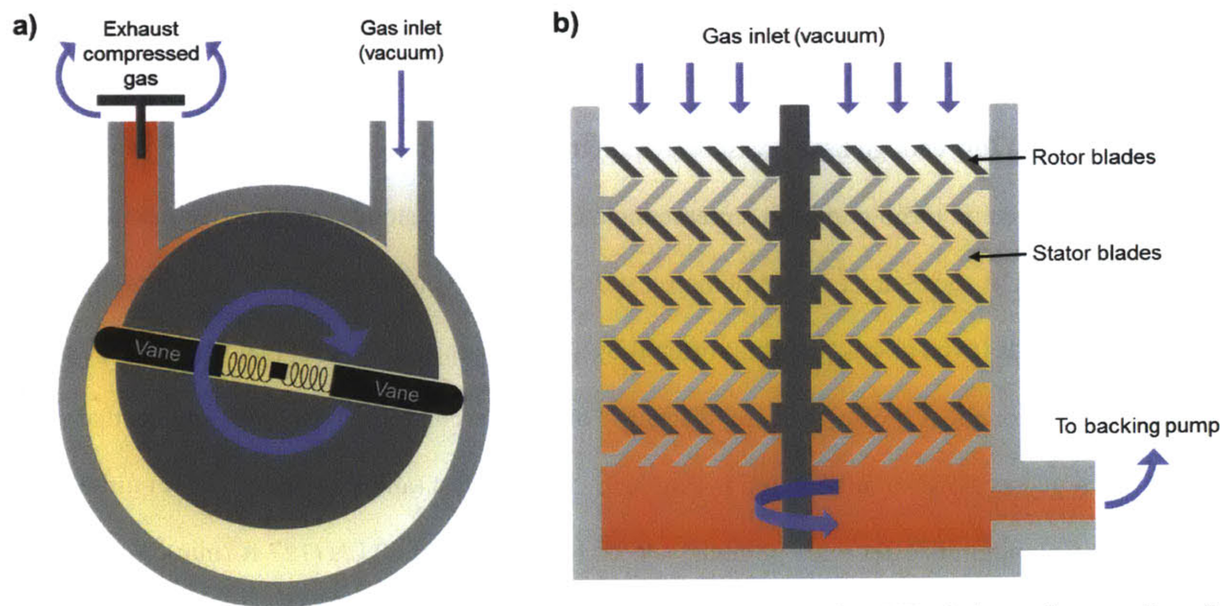

Figure 3.21: The two primary pump technologies considered for the 1" Fab DRIE. **a)** shows the operation of a single-stage rotary vane pump, and **b)** shows the configuration of a turbomolecular pump. Increasing levels of red indicate higher levels of gas compression.

A second type of vacuum pump that can achieve millitorr pressure levels is the rotary vane pump (shown graphically in **Figure 3.21a**). This type of pump, which can be used as the backing pump for a turbo system, operates by spinning a circular, but eccentrically placed rotor through a larger cavity. Spring-loaded vanes extending from the rotor are constantly pushing against the walls of the cavity, and thus create a sealed volume within the cavity that is compressed as the rotor turns (clockwise in **Figure 3.21a**). Once the pressure in the compressed volume exceeds the pressure at the outlet, a valve at the outlet is forced open and the compressed gas is expelled. As the rotor continues to turn, a new volume of gas is taken in from the inlet and the compression process begins again. In rotary vane pumps, oil is used as a lubricant for the rotor and vanes, as well as a sealant to help prevent gas from leaking between the wall and the vanes (and also to prevent leakage between the wall and rotor between the inlet and outlet ports). Rotary vane pumps can achieve pressures as low as 1 mTorr, but their pumping speed falls off quickly beginning approximately at 1 Torr (see **Figure 3.22a**). Rotary vane pumps are extremely robust and can handle exposure to atmospheric pressure and also large pressure fluctuations. They are made to run continuously for months at a time, with shutdowns required only to change the oil. The actual use of oil is one of the disadvantages of rotary pumps, as it precludes the use of certain gases which can form

flammable or explosive compounds with the oil. To get around this problem, specialized, highly inert perfluoropolyther (PFPE) oil can be used instead of the standard hydrocarbon-based oil, but this oil is quite expensive (~$1500 per gallon compared to $50-$100 per gallon for hydrocarbon oil).

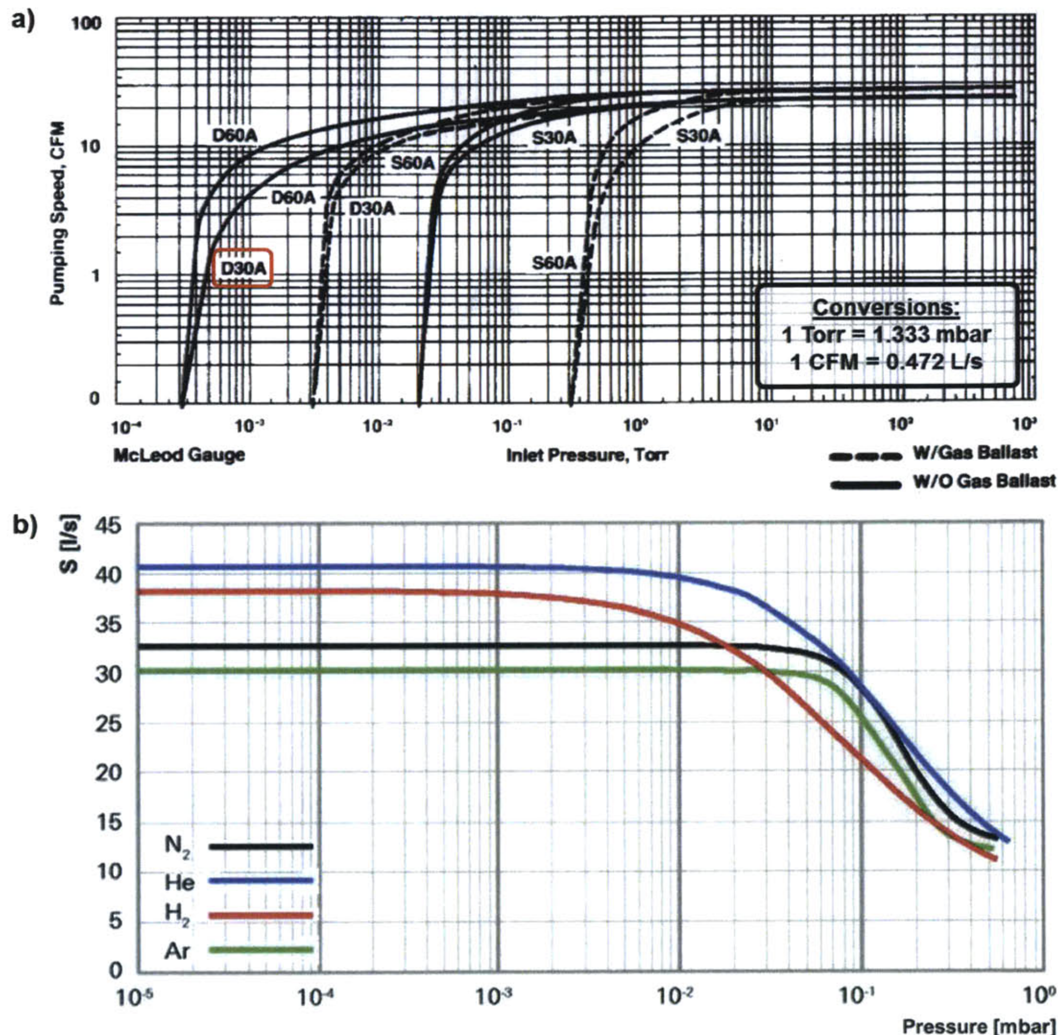

Figure 3.22: Pumping speeds vs. pressure for **a)** Leybold D30A rotary vane pump and **b)** Pfeiffer HiPace 80 turbo pump. Data courtesy of Oerlikon Leybold Vacuum GmbH and Pfeiffer Vacuum GmbH.

There are many other types of vacuum pumps such as diffusion pumps, scroll pumps, and roots blower pumps, each with their own advantages and disadvantages. Pumps from across all these classifications were considered for the 1" Fab DRIE system, with the rotary vane and turbo pumps emerging as the best potential combination of cost, size, and speed.

A comparison of the advantages and disadvantages of turbo pumps and rotary vane pumps is compiled in **Table 3.4**.

Rotary Vane Pump	**Turbo Pump**
Advantages: - Standalone operation - Very robust - Can be cycled from vacuum to atmosphere repeatedly - Relatively inexpensive to obtain and maintain	**Advantages:** - Exceptional performance at low pressures - Small / lightweight
Disadvantages: - Decreased pumping speed at low pressures - Requires expensive oil for operation with oxygen - Large / heavy	**Disadvantages:** - Relatively expensive - Requires a backing pump - Cannot handle large pressure fluctuations - Requires dedicated controller to handle spin up and spin down.

Table 3.4: Comparison of rotary vane and turbo vacuum pumps.

After weighing the merits of each type of pump, a rotary vane pump was chosen as pumping system for the prototype 1" Fab DRIE. These pumps' resilience against high pressures and pressure fluctuations, their overall hardiness, and their considerably lower cost when compared to a quality turbo pump system were the primary deciding factors. To pick a specific rotary vane pump, a figure of merit known as gas residence time was used. Residence time refers to how long a gas molecule remains in a certain region based on that region's volume, pressure, and the gas flow rate. Keeping residence times low is important in ensuring that products of an etch (in fluorine-based etches, the volatile SiF_4 molecules) can be efficiently removed from the vacuum chamber [27,28]. It can be calculated simply using the formula below:

$$Residence\,Time = \frac{Pressure \cdot Volume}{Throughput} = \frac{PV}{\dot{Q}} \tag{3.15}$$

Reported residence times for commercial DRIE systems range from tens of milliseconds to 2-3 seconds, and so this range was used as a metric for picking a specific rotary vane pump. The volume of the 1" Fab

DRIE chamber is approximately 750 mL (45 in^3), and the throughput during normal operation ranges from 1 to 5 sccm of process gas. Plugging these values into **Eqn. 3.15** yields a required process pressure range of ~8 to 42 mTorr for an optimistic residence time of 0.5 seconds, and range of 25 to 126 mTorr for a respectable 1.5 second residence time. With these values in mind, a Leybold D30A (Oerlikon-Leybold, http://www.oerlikon.com/leyboldvacuum/) was chosen as the rotary vane pump for this iteration of the 1" Fab DRIE (the D30A's pumping speed vs. pressure curve is shown in **Figure 3.22a**). Through the 1-100 mTorr range of pressures, the D30A offers 2-7 L/s (roughly 4-15 ft^3/min) of pumping speed. With this pumping speed, the 1" Fab DRIE system can achieve operating pressures between 30 and 50 mTorr under the normal range of gas loads, yielding residence times between 1 and 2 seconds (the center-point tests described in **Chapter 4** have residence times of 1.1-1.2 seconds). These residence times and pressures are well within the range of standard plasma etching conditions. Nevertheless, the 1" Fab DRIE design is compatible with all types of pumping systems, and if future test results indicate a preference for lower process pressures, a turbo pump system is easily integrable into the existing design.

3.2.4 Mass Flow Controllers

The final major piece of external equipment required for the operation of the 1" Fab DRIE is mass flow controllers (MFCs). MFCs are used to provide tightly controlled quantities of process gas to the etching chambers. As the data presented in **Chapter 4** will show, the precise amount of gas used during etching has a major effect on the properties of the etch, and so it is very important to have reliable MFCs. Furthermore, the fast switching requirements of Bosch Process DRIE necessitate a MFC solution that can switch and stabilize gas flows rapidly.

Traditional MFCs take in process gas from a reservoir like a regulated gas cylinder and use a variable throttle valve to control how much gas (mass per unit time) exits the MFC. Determining the correct position of the throttle valve can be accomplished in a number of ways. The most common method is to split a small portion of the process gas off into a measurement region, and then use a configuration of heaters and temperature sensors to determine the flow velocity. The flow velocity, plus knowledge of the

gas type flowing through the MFC allow the mass flow to be determined. Another, newer method for determining the mass flow also splits off a small portion of the input gas and passes it through a laminar flow element (LFE), which laminarizes the gas flow. In the laminar flow regime, the volumetric flow rate of a gas through an enclosure (like a tube) is directly proportional to the pressure drop across the length of that enclosure.

$$Volumetric\ Flow\ Rate = \frac{dV}{dt} = \dot{V} = \frac{\pi d^4 \Delta P}{128 \eta L} \tag{3.16}$$

$$Mass\ Flow\ Rate = \frac{dM}{dt} = \dot{M} = \dot{V}\rho_{meas} = \dot{V}\left(\frac{T_{STP}}{T_{meas}}\right)\left(\frac{P_{meas}}{P_{STP}}\right)\rho_{STP} \tag{3.17}$$

where:
d = diameter
P = pressure
η = viscosity
T = temperature
ρ = density

Equation 3.16 is known as the Hagen-Poiseuille law, and is also encountered in **Section 3.1.5** as part of the discussion on the 1" Fab DRIE's gas distribution system. By measuring the differential pressure across the laminar flow element, the volumetric flow rate can then be determined. To then get to the mass flow rate, the volumetric flow rate is multiplied by the temperature and pressure compensated density of the gas flowing through the LFE. To calculate these compensation factors, the gas temperature and absolute pressure are also measured within the LFE.

Thermal MFCs have a long history of production and refinement, making them extremely reliable options for gas delivery, but for plasma etching applications, much superior performance is found on the newer LFE-based MFCs. Most notably, LFE MFCs offer much quicker response times than thermal MFCs, as measuring differential pressure is significantly faster than measuring thermal convection. The heated elements on thermal MFCs also take at least 10 minutes to initialize and equilibrate, compared to LFE MFCs which are ready to operate within 1 second of powering up. A table containing these and other quantitative comparisons of LFE and thermal MFCs is shown below.

	Thermal MFCs	Laminar Flow Element MFCs
Response/Settling Time	1 to 2 s (300 to 500 ms with predictive software corrections)	50 to 100 ms
Accuracy	0.5 to 1% of setpoint	0.4 to 0.8% of setpoint + 0.2% of full scale
Repeatability	0.2 to 0.3% of setpoint	0.2% of full scale
Turndown Ratio	50:1 to 100:1	200:1
Warm-Up Time	≥10 minutes	<1 sec
Additional Functionality	-	Control of volumetric flow or pressure
Cost	$1000 to $3000, depending on flow range and performance	$1350 to $1800, depending on flow range

Table 3.5: Comparison of thermal and laminar flow element mass flow controllers.

The combination of superior performance and competitive pricing make LFE MFCs the easy choice for the 1" Fab DRIE. The particular LFE MFCs chosen were the MC series from Alicat Scientific, Inc [29]. Alicat is one of the original pioneers of LFE mass flow measurement technology, and their MFCs have gained enough of a reputation that they are now sold by major instrumentation companies like Omega and Cole-Parmer. The Alicat MC series MFCs have both analog and serial control and readback capability, and come standard with digital calibration profiles for 30 common gases (which include all the potential gases for Bosch Process etching (i.e. SF_6, O_2, N_2, Ar) except C_4F_8, which was added as a custom calibration profile). One of the most important characteristics of the Alicat MC series is its large turndown ratio. The full range of the Alicat MFCs used in the presented iteration of the 1" Fab DRIE is 100 sccm, and with the datasheet turndown ratio[16] of 200:1, this allows a minimum flow of 0.5 sccm. The actual turndown ratio is much higher though, exceeding 1000:1, which enables flow setpoints at least as low as 0.1 sccm. The actual flow rates used during testing fell primarily in the 0.5 to 5 sccm range due to the desired residence times and the balance between process pressure and pumping capability (refer back to **Section 3.2.3** more details). While these flows are certainly at the lower end of the Alicat's 0-100 sccm flow range, the extra headroom at the top allows the same MFCs to be used if, for instance, a turbo pump is added to a future iteration and the overall pumping capability drastically increases, thus allowing higher

[16] The turndown ratio is the ratio between the largest and smallest flows possible from a single MFC. For instance, a 100:1 turndown ratio on a 50 sccm full scale MFC means that the lowest flow possible is 0.5 sccm.

gas flows for the same pressure (and therefore reducing the residence time). Conversely, if very low flows are determined to be ideal, LFE MFCs with full scale ranges down to a miniscule 0-0.5 sccm (with the same turndown, accuracy, and response time characteristics) are available from Alicat Scientific.

Chapter 4: Characterization of the 1" Fab DRIE

In order to characterize the performance of the 1" Fab DRIE, a variety of experiments were performed to test the stability and practical limits of the system. These tests include assessments of the system's individual components and subsystems (**Section 4.1**), and tests of the performance of SF_6-based etching (**Section 4.2** and **4.3**).

4.1 Vacuum and Plasma Characterization

In this section, the performance of the vacuum and plasma generation subsystems of the 1" Fab DRIE is quantified. The reliable performance of these subsystems is crucial to the overall success of the etching system. The results shown helped determine the operational boundaries of the system and also validated several of the major design decisions described in **Chapter 3**.

4.1.1 Pump Rate and Leak Rate

The first steps taken to characterize 1" Fab DRIE were to quantify its vacuum tightness and its pumpdown time. This was accomplished by measuring the system's leak rate, base pressure, and time to reach base pressure. Throughout these tests and the etching tests of **Section 4.3**, the system pressure was measured using a Kurt J. Lesker KJL-6000 thermocouple pressure gauge (Kurt J. Lesker, http://www.lesker.com/).

In vacuum systems, there are two main classes of leaks: residual leaks and virtual leaks. The end effect of these leak types are the same, but the sources are very different. Residual leaks stem from physical imperfections in sealing surfaces or other unintentional flow paths to atmosphere. Virtual leaks, on the other hand, are caused by materials or surfaces within the evacuated chamber. They are caused by outgassing of chemicals or trapped pockets of gas created during assembly, machining, or simply exposure to atmospheric pressure. Residual leaks are generally larger in magnitude and can be detected more easily, whereas the sources of virtual leaks are often much more difficult to determine. A very common source of virtual leaks in a vacuum chamber is the trapped volume of gas below screws in blind

threaded holes. As the screws are threaded into these holes (at atmospheric pressure), air is trapped on the bottom of the screw and must traverse through a very low conductance path between the screw threads and the hole threads to escape under vacuum. To help avoid this virtual leak source, "vented" screws are commonly used. **Figure 4.1** illustrates the differences between standard and vented screws. Vented screws have small holes passing through shank that provide a significantly larger conductance path for the trapped air to escape when the vacuum chamber is evacuated. Virtual leaks do have the advantage that they can be essentially eliminated given enough pumping time (which can be reduced with proper prevention methods), whereas residual leaks must be found and plugged.

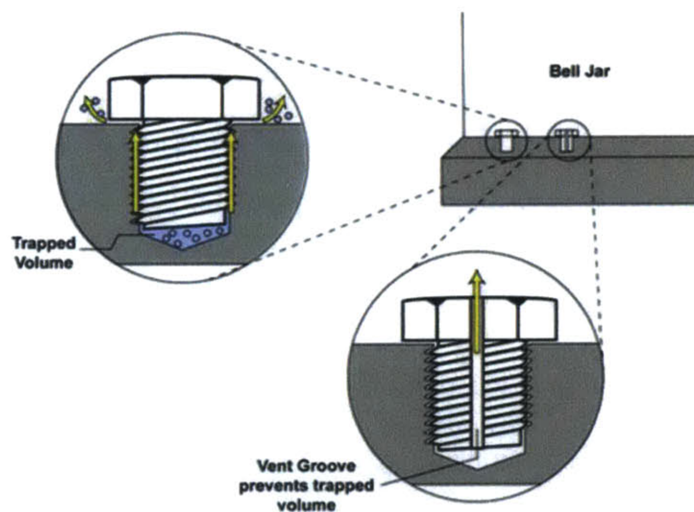

Figure 4.1: Virtual leaks caused by vented screws are shown in this figure. The image on the left shows the high conductance path trapped gas has to travel through before being pumped away and the image on the right shows a vented screw with no trapped gas due the higher conductance path created by the vent hole. Image courtesy of SciTek [30].

To establish the system's practical base pressure, the chamber was pumped down for 6 hours to allow sufficient time for any major virtual leaks to subside. After 15 minutes, the system pressure had dropped to 10 mTorr, and after the full 6 hours, a base pressure of 8 mTorr was reached.

To characterize the practical leak rate of the system, the system was evacuated for a period of 10-15 minutes on several different days (during the week of the etching characterization tests) and after a variety of different processing conditions. After this time, the vacuum valve connecting the chamber to the vacuum pump was closed (leaving the chamber free to vent to atmosphere through any residual leak paths

or remaining virtual leak sources). Once the valve was closed, the pressure was recorded every 10 seconds for 60 total seconds and the rate-of-rise in mTorr per minute was calculated. The leak rate can then be calculated by multiplying the rate-of-rise by the volume of the chamber. The volume of the chamber is ~750 mL, and so the effective leak rate for the chamber is between 0.9×10^{-5} and 1.5×10^{-4} atm·cm^3/sec. The data for these tests is shown in **Figure 4.2**. Converted to the sccm unit used by mass flow controllers (which is technically a unit of throughput (pressure×volumetric flow) and not mass flow (density×volumetric flow)), this leak rate is equivalent to a flow of 0.005 to 0.009 sccm, which is 0.27% to 0.44% of the total center point flow rate of 2 sccm.

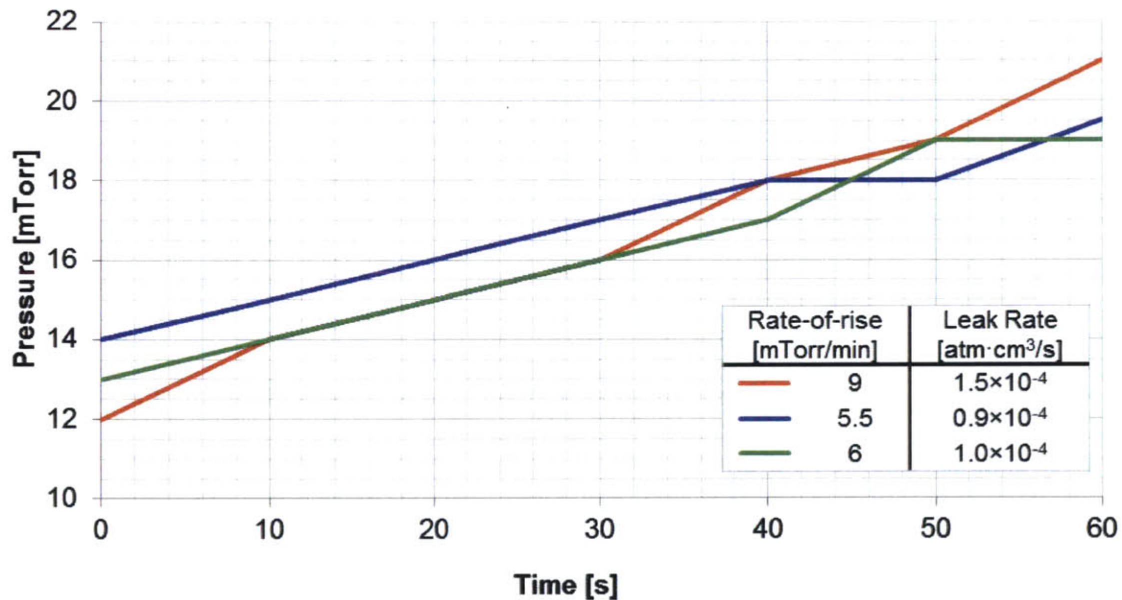

Figure 4.2: The rate-of-rise pressure data after 10-15 minutes of pumpdown. The legend indicates the total rate-of-rise and effective leak rate for each test.

4.1.2 Plasma Characterization - Langmuir Probe

To characterize the performance of the ICP coil plasma generation subsystem, the plasma density was measured for a variety of common processing conditions using a piece of equipment known as a Langmuir probe (LP). Langmuir probes operate by measuring the sheath characteristics of the plasma when different voltages are applied to the probe tip. When the probe voltage is swept from negative to positive, the electrons and ions interact with the probe yielding information about the plasma. A more

detailed description is included in **Appendix E**. The information gained from the LP tests was then used to inform the parameter selection for the etch rate experiments described in **Sections 4.2** and **4.3**.

LP tests were performed for three different process gas configurations (SF_6, O_2, and SF_6+O_2), and for each configuration, measurements were taken at a range of applied RF powers. The selected power ranges centered around the E- to H-mode transition for each gas configuration, as this region contains the most information about the system's performance and realistic limits. The importance of and meaning behind the E- to H-mode transition was introduced in **Section 2.3**. A summary of the parameters used for the LP measurements is included in **Table 4.1**.

	O_2	SF_6	SF_6+O_2
O_2 Flow	5 sccm	-	0.5 sccm
SF_6 Flow	-	1.5 sccm	1.5 sccm
Coil Power Range	30-120 W	100-240 W	100-240 W
Base Pressure	15 mTorr	15 mTorr	15 mTorr
Process Pressure	45 mTorr	35 mTorr	39 mTorr

Table 4.1: Summary of the parameters used for the three Langmuir probe test sequences.

Inductively coupled plasma generation systems have two different regions of operation. The first is a capacitively coupled, electric field-driven mode (the E-mode) that has a characteristically low luminosity and low plasma density, and the second is an inductively coupled, electromagnetically dominated mode (the H-mode) that exhibits characteristically high luminosity and high plasma density. The transition from E- to H-mode (and vice versa from H- to E-mode) happens abruptly, and the accompanying change in brightness is easily noticeable, even through the opaque alumina chamber walls. The E→H and H→E transitions also display a significant amount of hysteresis, with the H-mode region of operation requiring large powers to ignite, but far less power to sustain once ignited. This bi-stability can be roughly explained by the nonlinearities in the power balance equations first introduced in **Section 3.2.1.**

These nonlinearities have been thoroughly studied and modeled by several investigators [22]. In general, the power balance dictates a single unique plasma density for a given coil current, but due to the nonlinearities, two stable solutions and one unstable solution for the plasma density exists at certain coil currents. These multiple solutions are shown graphically in **Figure 4.3**, courtesy of G. Cunge, et al [31]. In these situations the plasma will remain in either E-mode or H-mode given its previous state. As the coil current is changed (effectively raising the power) the plasma density jumps from one mode to the other (E→H or H→E) depending on the previous state. The preference of the plasma discharge to remain in its current state leads then to the hysteresis effect seen for the E→H and H→E transitions. This hysteresis is often taken advantage of by temporarily using a large power to initiate an H-mode discharge and then lowering the applied power to a level just above the H→E transition. In the following Langmuir probe analysis, the exact position of these transitions, as well as the associated plasma densities are determined for the inductively coupled plasma generation system used in the 1" Fab DRIE.

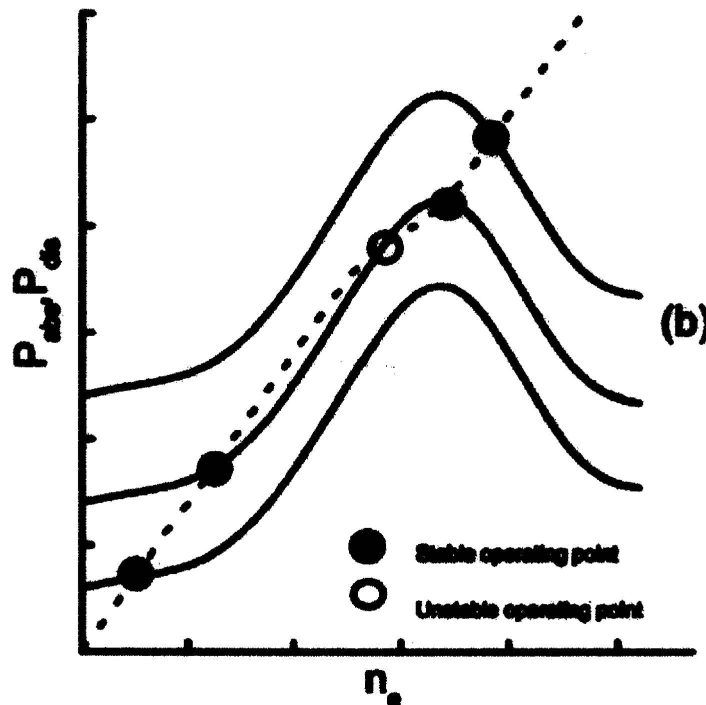

Figure 4.3: Power balance showing why E→H and H→E transition occurs. Power is plotted on the Y axis and electron density is plotted on the x axis. P_{abs} (solid line) and P_{dis} (dotted line) are plotted for three different coil currents and the equilibrium point $P_{abs} = P_{dis}$ are shown with black dots. In the unstable coil current condition, two stable and one unstable (open black dot) are shown indicating the E→H / H→E transition point. Plot reproduced courtesy of G. Cunge, et al [31].

The Langmuir probe used in the characterization tests is shown in **Figure 4.4a**. The probe consists of a 0.0625" (1.6 mm) diameter stainless steel rod encased in 0.25" (6.4 mm) OD alumina tubing that has a BNC connection one end, and a 0.125" (3.2 mm) long section of the stainless steel rod protruding from the other. This small exposed area of the rod serves as the probe tip which collects the charge, and the BNC connector is used connect the probe to a source-measurement unit (SMU), which provides the potential and measures the current gathered through the tip. For a vacuum-tight seal, the rod and alumina tubing are glued together using Torr-Seal epoxy (Agilent Technologies, http://www.agilent.com/) and the full probe assembly is inserted into the system via a CF1.33" to Ultra-Torr compression fitting (Swagelok Company, http://www.swagelok.com/) adapter centered on the top flange of the upper vacuum chamber assembly (shown in **Figure 4.4b**).

For the actual measurements, an HP 4145B semiconductor parameter analyzer was configured to provide a DC voltage sweep across a source-measurement unit and record the resulting probe currents. The measurement signals were filtered using an inline 5MHz low pass filter. A circuit diagram for this setup is shown in **Figure 4.4c**. The applied probe potentials and the resulting probe currents were then imported into Mathematica, and the plasma characteristics were extracted using the LP analysis procedures summarized in **Appendix E**.

Each LP sweep and subsequent analysis provides a single data point for a specific set of plasma conditions. To build the curves showing the transition between the E- and H-modes, sweeps at many different power levels were required.

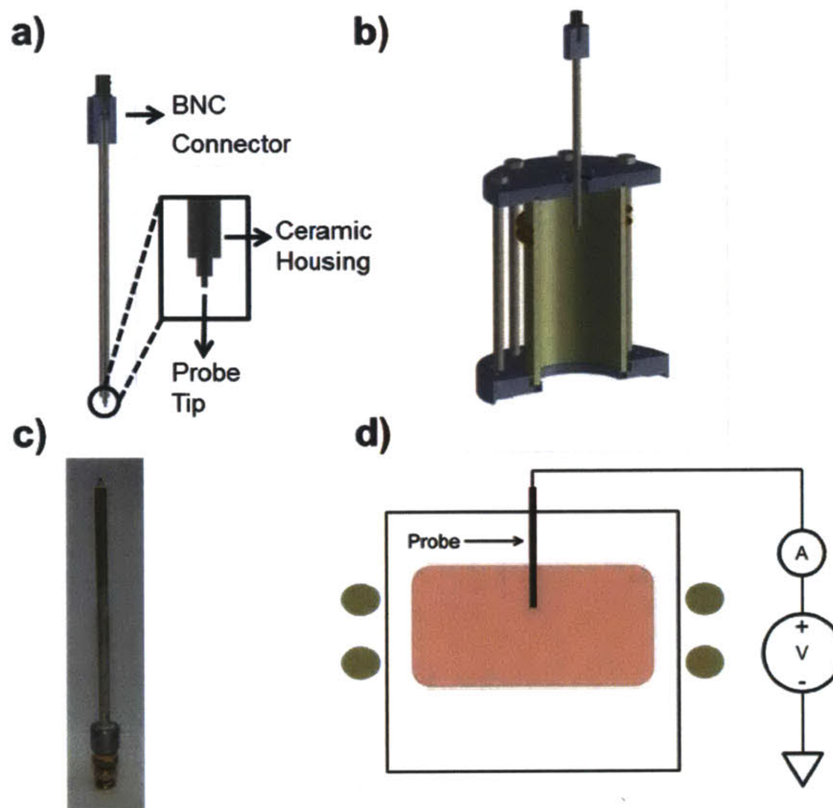

Figure 4.4: Langmuir probe setup. **a)** Cross section of LP showing BNC connection and stainless steel probe tip. **b)** Rendering showing how the probe sits within the chamber. **c)** Actual LP used in experiments. **d)** Circuit diagram of the LP measurement setup.

The first LP sweeps performed were on O_2 plasmas. With 5 sccm of O_2 being introduced by the gas showerhead (5 sccm is the amount of O_2 flown during the plasma cleaning steps) and the chamber pressure stable at 45 mTorr, sweeps were performed for coil powers ranging from 30 W to 120 W. To obtain a measure of the spatial uniformity of the plasma, data sweeps were performed at two different heights in the chamber, one located at the center of coil, and one located 1" above the coil center. The results for these sweeps are shown in **Figure 4.5**.

The E- to H-mode transition for this O_2 plasma system was recorded at ~75W. Comparing the two measurement heights shows that, on average, the plasma densities at the center of the coil were three times higher than the plasma densities found at the edge of the plasma. The peak plasma density recorded in this sweep was 8.46×10^{10} cm^{-3} and as expected, the densities increase monotonically with increasing RF powers. Oxygen plasma cleaning in the 1" Fab DRIE is performed with at least 125 W of power

applied to coil (and most commonly 150 W), and so this data confirms that these cleaning processes are being run well above the E→H transition power and therefore in the high density, inductively coupled mode.

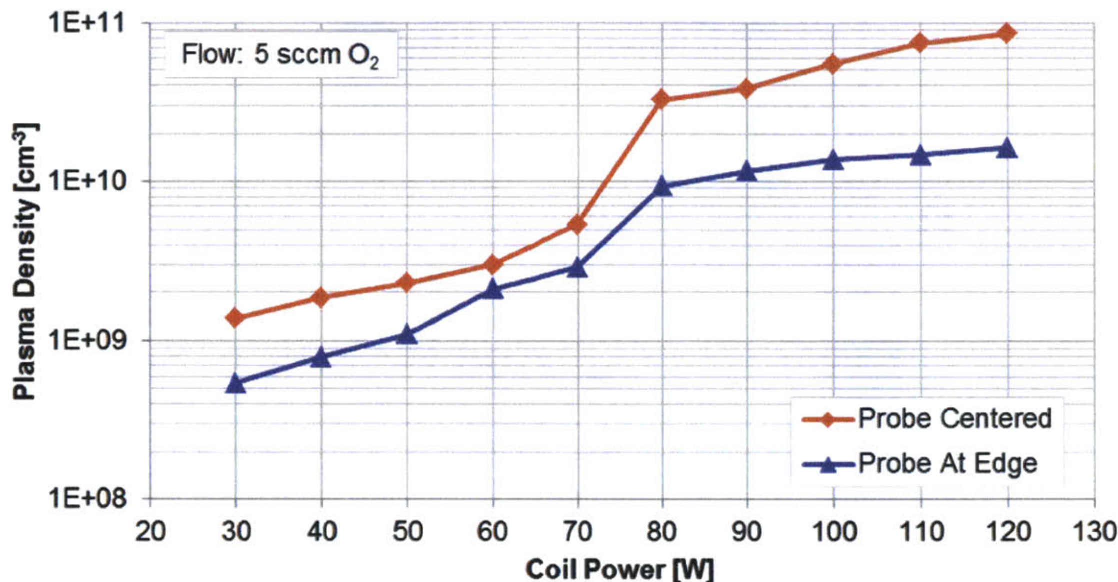

Figure 4.5: Plasma density vs. Coil power for oxygen plasma discharge. The red trace represents measurements taken with the Langmuir probe at the center of the discharge, while the blue trace shows measurements from 1" above the center of the discharge.

For the remaining two process gas configurations (SF_6 and SF_6+O_2), data on the full hysteresis loops was gathered. The results from these sweeps are shown in **Figure 4.6**. For both configurations, the E- to H-mode transition occurred between 200 and 210 W and the H→E transition occurred at approximately 150W. From this plot, it is clear that the SF_6+O_2 plasma exhibits lower plasma densities than simply SF_6 in the H-mode region. This would seem to contradict the established (and previously mentioned in **Section 2.3.3**) notion that higher etch rates (and thus higher plasma densities) occur with the addition of O_2 to SF_6 (up to 30-40% by volume). M. Morshed, et al [32] have in fact directly shown that the addition of up to 20% O_2 to SF_6 increases the etch rate and increases the plasma density. One factor that the data of **Figure 4.6** does not consider however, is the difference in pressure for the two gas configurations. Both configurations used 1.5 sccm of SF_6, but the SF_6+O_2 contained an additional 0.5 sccm of O_2, which raised the system pressure by 4 mTorr. According to Paschen's Law (discussed in **Section 2.1**), increases

in pressure cause increases in the required ionization voltages for a plasma discharge, and subsequently the power necessary to maintain the same plasma density increases. This could potentially be the reason for the larger observed H-mode densities for the SF_6-only configuration. The relative densities aside, the data of **Figure 4.6** do provide the very important numbers of an E- to H-mode transition near 200 W and the ability to reliably sustain an H-mode discharge at powers as low as 160 W.

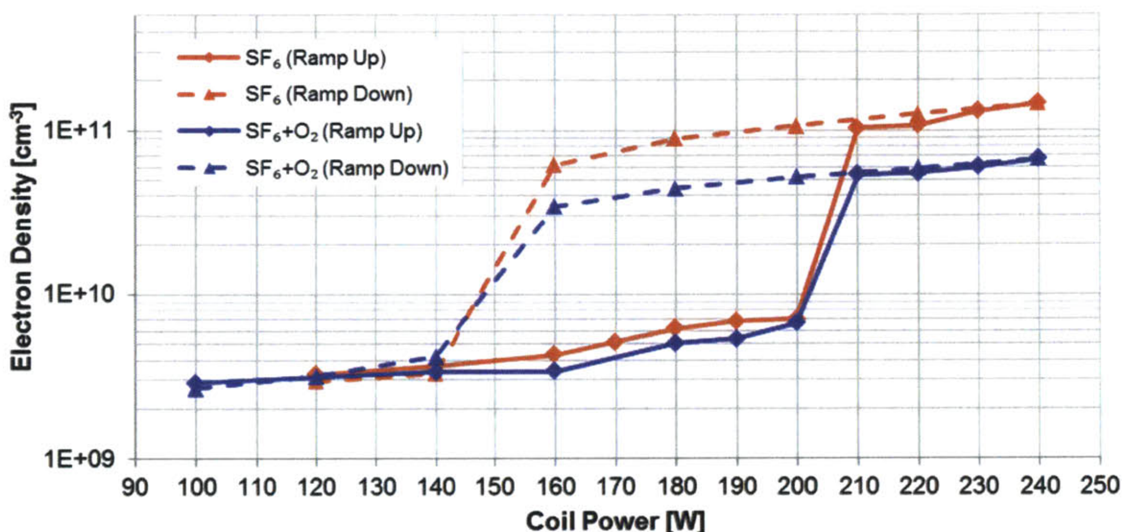

Figure 4.6: Plasma density vs. Coil power for SF_6 (red traces) and SF_6+O_2 (blue traces) plasma discharges. The solid lines represent measurements taken while ramping up the coil power, while the dotted lines represent measurements taken while ramping down the coil power.

4.2 Experimental Design

After establishing some of the capabilities and limits of the system through the Langmuir probe and system pressure tests described in the previous section, several exploratory SF_6-based etching recipes were performed to establish a reasonable range of parameters that could produce quality silicon etches. Once this range was established, a systematic plan for testing the performance of the 1" Fab DRIE system was constructed. Background information and details of this plan are outlined in **Section 4.2.1**, followed by the experimental protocol in **Section 4.2.2**, and a summary of the measurement and imaging techniques used in **Section 4.2.3**, and a discussion of the test wafers used in **Section 4.2.4**.

4.2.1 Response Surface Methodology

Analyzing the results of the exploratory etches in the 1" Fab DRIE system produced a list of five tunable parameters that had a potentially significant impact on the etch characteristics. These five are the ICP (or coil) power, the substrate electrode (or base) power, the SF_6 flow, the O_2 flow, and the spacing between the ICP coil and the substrate electrode. While it would have been ideal to rigorously and systematically test the effects of all five of these parameters, timing requirements restricted the systematic characterization to just three of the five: SF_6 flow, O_2 flow, and base power. The fixed level for each of the remaining two parameters (coil power and coil-substrate spacing) was carefully selected after evaluating the initial stability tests. A coil power of 200 W was chosen after examining the Langmuir probe test results discussed in **Section 4.1.1**, which demonstrated that this power was well within the coil's inductively-coupled (H-mode) region of operation. A spacing of 3.5" (89 mm) between the coil and substrate (at the larger end of the possible spacing) was chosen based on physical considerations about the transport of radicals and ions to the substrate surface [33] and the removal of etch products from the chamber. The 3.5" (89 mm) spacing chosen represents a sufficiently long distance to ensure that the distribution of radicals and ions is uniform once it reaches the substrate (see **Section 3.1.6** for a discussion of gas distribution and diffusion lengths), and also preserves a reasonably large conductance path to the chamber exit. This conductance path allows low pressures to be maintained in the system and facilitates the quick removal of reaction products from the system.

In order to test the effects of the three selected parameters (SF_6 flow, O_2 flow, and base power), a statistical design-of-experiments (DOE) technique known as the response surface method (RSM) was used. The response surface methodology was originally formulated by G.E.P. Box and K. B. Wilson in 1951 as a method for determining the set of parameter values (known as "factors") that produce an optimum response in a system [34]. With a proper design, the response surface method can yield important information about not only the linear effects of parameter changes on a system, but also any second-order and multi-factor interaction effects.

The particular design chosen for the work of this thesis is known as a circumscribed central composite (CCC) design. The simplest way to explain CCC designs is graphically. **Figure 4.7** shows the graphical representation of a three factor CCC design (compiled from the actual SF_6 / O_2 / Base power design used in this chapter), where the X, Y, and Z axes are assigned to the three factors. Each point on the graph represents an individual experiment, and the coordinates of that point indicate the level of each factor in that experiment. The standard practice is to the code these levels in order to compensate for scale differences between the real values used for each factor.

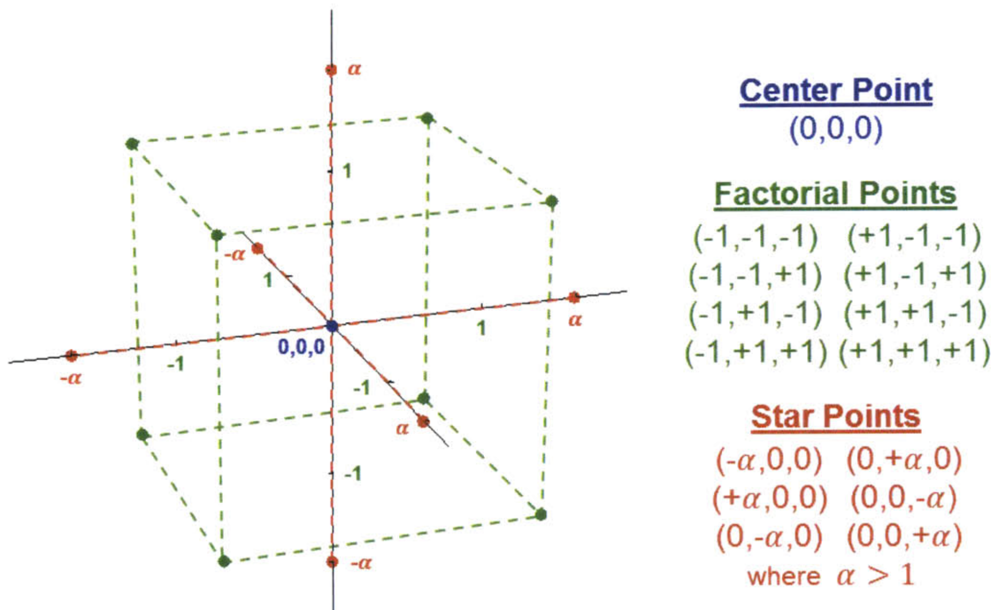

Figure 4.7: The coded factor values in the experiments of a three factor CCC design can be mapped to points on the XYZ plane, where each factor is assigned to one of the three axes. Each of the blue, green, and red dots each correspond to a different experiment.

CCC designs use a combination of three different types of experiments, which are represented by the colors used for the points in the graphs. The blue point represents the center (or zero) point of the design, which is coded as $[0,0,0]$. The green points represent the factorial tests, which are coded as $[\pm1, \pm1, \pm1]$. These points are sometimes referred to as the "cube tests" because in Cartesian space they make up the vertices of a cube. A CCC design with n factors contains 2^n factorial tests. On their own, full factorial tests are a useful tool for determining any linear effects of factor changes. The red points represent the axial, or star tests, which are coded $[\pm\alpha, 0,0]$, $[0, \pm\alpha, 0]$, or $[0,0, \pm\alpha]$. For an n-factor CCC

design, there are always $2n$ star tests. In CCC designs, the value of α is always greater than one, and the specific value is chosen to give the design certain properties. These properties and the methods for choosing α are discussed in the following paragraphs. The star tests probe the extremes of a particular system and allow RSM analysis to estimate any curvature in the response surface.

The specific details of the 3-factor CCC design outlined above were generated and analyzed using the free, open-source (GNU GPL license) statistical analysis program **R** (http://www.r-project.org/) and the *RSM* package for **R** maintained by R.V. Lenth (http://cran.r-project.org/web/packages/rsm/index.html). For exploring potential CCC design configurations, the *RSM* package contains a very useful function called *ccd.pick*, which allows the user to input basic information about their desired central composite design and receive back several different experimental designs that fit their criteria. A screenshot of the results of the *ccd.pick* function for 3 factors is shown in **Figure 4.8**. The boxed result in **Figure 4.8** shows a 20 test CCC design for 3 factors, which is the design chosen used in this thesis. The 20 tests include the basic 16 tests required for any 3 factor CCC design (8 factorial tests, 6 star tests, and 2 center point tests), plus an additional 4 center point tests (6 total center point tests). In addition to their statistical usefulness in computing the lack of fit for RSM models and testing for model curvature [35,36], multiple center points are useful in and of themselves because they provide a measure of the system's repeatability over time.

```
> ccd.pick(3, restrict = "N<25")
   n.c n0.c blks.c n.s n0.s bbr.c wbr.s bbr.s  N alpha.rot alpha.orth
1    8    2      1   6    1     1     1     1 17  1.681793   1.673320
2    8    6      1   6    4     1     1     1 24  1.681793   1.690309
3    8    5      1   6    3     1     1     1 22  1.681793   1.664101
4    8    3      1   6    2     1     1     1 19  1.681793   1.705606
5    8    4      1   6    2     1     1     1 20  1.681793   1.632993
6    8    4      1   6    3     1     1     1 21  1.681793   1.732051
7    8    5      1   6    4     1     1     1 23  1.681793   1.754116
8    8    6      1   6    3     1     1     1 23  1.681793   1.603567
9    8    1      1   6    1     1     1     1 16  1.681793   1.763834
10   8    3      1   6    1     1     1     1 18  1.681793   1.595448
>
```

Factorial Points | Center Points in Factorial Block | Star Points | Center Points in Star Block | Total # of Tests | Potential α values

Figure 4.8: Screenshot of the output of the ccd.pick function called with the input parameters of 3 factors and a requirement of less than 25 total tests. The design chosen is denoted by the red box, and several relevant column headings are defined in black below the output.

The results of *ccd.pick* provide two possible values for α (*alpha.rot* and *alpha.orth*). Selecting *alpha.rot* as the α value will produce a rotatable design, which means that the variance of a point on the generated response surface will only depend on the distance of that point to the center point of the design, not the direction [35,37]. Setting α to *alpha.orth* will instead produce a design that blocks orthogonally, the effect of which is explained in the following paragraph. It is worthwhile to note that the values shown for *alpha.rot* and *alpha.orth* are generally quite close to one another (for the selected design, they differ by less than 3%), and so selecting one over the other (or a value in between) for α will still result in a design that is nearly rotatable or nearly orthogonal, and will have only a small impact on the actual results [37]. For the SF_6 / O_2 / Base power CCC design, the *alpha.orth* value of ~1.633 was chosen for α.

CCC designs are traditionally split into two blocks, a factorial block and a star block, with the center points distributed among the blocks according to orthogonality requirements. In the 20 test design, four of the center points are assigned to the factorial block (yielding a total of 12 tests)[17], and the remaining two are assigned to the star block (8 total tests). Blocking is used to eliminate nuisance variables such as

[17] The factorial block of the 20 test design chosen can also be subdivided into two 6 test blocks (each containing half of the full factorial tests and 2 center points). This is the reason for the *1a* and *1b* notation in **Table 4.2**. For the actual testing, the 12 tests were performed as a single block.

the effect of running tests over multiple days or using multiple bottles of a reagent. When a CCC design is constructed to block orthogonally, it means that the effect of blocking the design does not affect the calculation of the coefficients for the response surface model [37]. Instead, a blocking factor is produced as part of the RSM analysis of a blocked design which compensates for any block-specific differences.

With the 20 test design and an α value chosen, the *ccd* function of the *RSM* package was used to generate the actual list of tests to be performed. **Table 4.2** contains this list in both coded and actual units.

		Coded Values			Actual Values		
Standard Order	**Block**	**Parameter 1**	**Parameter 2**	**Parameter 3**	**SF6 Flow [sccm]**	**O2 Flow [sccm]**	**Chuck Power [W]**
1	1a	-1	-1	-1	1	0.25	5
2	1a	-1	+1	+1	1	0.75	15
3	1a	+1	-1	+1	2	0.25	15
4	1a	+1	+1	-1	2	0.75	5
5	1a	0	0	0	1.5	0.5	10
6	1a	0	0	0	1.5	0.5	10
7	1b	-1	-1	+1	1	0.25	15
8	1b	-1	+1	-1	1	0.75	5
9	1b	+1	-1	-1	2	0.25	5
10	1b	+1	+1	+1	2	0.75	15
11	1b	0	0	0	1.5	0.5	10
12	1b	0	0	0	1.5	0.5	10
13	2	-1.633	0	0	0.684	0.5	10
14	2	+1.633	0	0	2.317	0.5	10
15	2	0	-1.633	0	1.5	0.092	10
16	2	0	+1.633	0	1.5	0.908	10
17	2	0	0	-1.633	1.5	0.5	1.835 (2)
18	2	0	0	+1.633	1.5	0.5	18.165 (18)
19	2	0	0	0	1.5	0.5	10
20	2	0	0	0	1.5	0.5	10

Coding Formulas		
$CP_{SF_6} = 1.5\ sccm$	$\Delta_{SF_6} = 0.5\ sccm$	$SF_6\ Flow = (Coded\ Value) * \Delta_{SF_6} + CP_{SF_6}$
$CP_{O_2} = 0.5\ sccm$	$\Delta_{O_2} = 0.25\ sccm$	$O_2\ Flow = (Coded\ Value) * \Delta_{O_2} + CP_{O_2}$
$CP_{BP} = 10\ W$	$\Delta_{BP} = 5\ W$	$Base\ Power = (Coded\ Value) * \Delta_{BP} + CP_{BP}$

Table 4.2: Coded and actual parameters values for the selected 20 test CCC RSM sequence. The center point and delta values for each parameter, as well as the formulas used to convert between coded and actual values are shown at the base of the table.

In order to move from the coded units to the actual units, the design center point and the increments (or deltas (Δ)) for each factor must be chosen. For the SF_6 / O_2 / Base power design, determining these

values involved balancing the desire to test a large a parameter space with the knowledge gained about the performance and limits of the system from the initial tests (for example, as the process gas flow increases, the system pressure increases and the power required to achieve the E- to H-mode transition increases significantly). The parameters ultimately chosen are summarized in at the bottom of **Table 4.2.**

One of the phenomena that played a large role in determining the placement of the center points was the variation in the etch profile with the percentage of O_2 included in the total process gas flow (calculated as $O_2\% = (Flow_{O_2}/(Flow_{O_2} + Flow_{SF_6})$. This effect has also been documented in the literature [12]. Microscopy of the early samples showed a transition in the etch profile for O_2 fractions near 25%. Samples with higher fractions of oxygen exhibited largely isotropic etching, while etching with less oxygen generally led to anisotropic profiles. The particular value of 25% O_2 is also near several literature accounts of the ideal oxygen fraction for achieving the maximum etch rate in an SF_6+O_2 system (this topic was mentioned in **Section 2.3.3**). As etch profile control and etch rate are among the most important factors in DRIE, the O_2 fraction for the center point of the RSM testing was set at 25% (1.5 sccm of SF_6, 0.5 sccm of O_2) to further explore this relationship. The deltas of 0.5 sccm for SF_6 and 0.25 sccm for O_2 were chosen in order to generate a wide range of O_2 fractions (the ratios in the design range from 6% to 43%). The center point base power of 10 W was chosen to fit within the range of powers used in commonly run DRIE processes [38,39]. The delta of 5 W was selected to ensure that a wide range of ion energies were generated by the tests, as it was hypothesized that these ion energies would play a significant role in determining the etch parameters. Once the test sequence was finalized and the system's stability across all of the chosen parameters was verified, testing commenced.

4.2.2 Experimental Protocol

The following experimental protocol was developed during the initial testing of the 1" Fab DRIE, and used throughout the RSM test sequence.

1. Before the first test of each day, let the system pump down for 15 minutes and perform an oxygen plasma clean for 10 minutes with a blank dummy sample loaded onto the chuck.
    a. Parameters: 5 sccm O_2, 150 W coil power, 0 W base power, 10 minutes.
2. Vent the chamber and remove the dummy sample from the chuck.
3. Apply thermal grease (Apiezon H, http://www.apiezon.com/products/vacuum-greases/h-grease) to the bottom of a test sample (see **Section 4.2.4** for details on the test sample design and preparation) and load it onto the chuck.
4. Evacuate the chamber until the pressure reaches 12-13 mTorr and the chamber temperature (as measured on the top flange) falls to 30°C.
5. Load the parameters for the next test in RSM sequence into the ERAC software and initiate the gas flows.
6. Once the gas flows have stabilized, record the system pressure and begin the test sequence (enabling the RF powers).
7. If the test involves large gas flows, prepare to manually ignite the E- to H-mode transition by selecting a larger power (usually +50 W) for the coil generator setpoint. After the ICP discharge is established (usually within one second), return the coil generator setpoint to the prescribed value for the test.
8. Ensure that the system function is stable by checking the impedance matching for both generators and the gas flows on the MFCs.
9. Once the test is complete (15 minutes), allow the purge sequence to complete and check that the system pressure is at or below 12-13 mTorr (to ensure there are no leaks or residual process gas in the chamber).
10. Vent the chamber and carefully remove the test sample from the chuck.
11. Clean any residual thermal grease from the chuck and load a blank dummy sample onto the chuck.
12. Evacuate the chamber until the system pressure drops below 20 mTorr.

13. Perform a 5 minute oxygen plasma clean.
    a. Parameters: 5 sccm O_2, 150 W coil power, 0 W base power, 5 minutes.
14. Repeat Steps 2 through 12 for any remaining tests.
15. After the last test of the day, load a blank dummy sample onto the chuck and evacuate the chamber.

Each sample in the RSM sequence was generated by performing this sequence of steps. Running through the main repeated block (steps 2 through 12) took approximately 40-45 minutes per sample. Each of the test blocks were collected over a single (long) day of testing, so as to accurately adhere to the blocking regime chosen.

4.2.3 Sample Analysis Procedures

After the 20 tests were completed, each etched sample was measured and characterized using a variety of methods. An outline of each of these methods is included in the following sections.

4.2.3.1 Cross-sectional Measurement Microscopy

For this method, each sample was cleaved perpendicular to the long axis of the trenches to expose a cross-sectional profile of the etch, as shown in **Figure 4.9**. Laterally, this cleave was performed at the centermost section of the dense (100 um spacing) pattern. The cleaved sample was then mounted vertically in a spring-loaded holder and placed under a Nikon Measurescope UM-2 microscope with digital readout (DRO) of the position of the X and Y axes accurate to 1 μm (DRO: Heidenhain Quadra-Chek II). An image of the microscope setup and a vertically mounted sample are shown in **Figure 4.10**. By aligning the reticle in the eyepiece of the Measurescope over the focused edges of the cleaved sample and adjusting the X and Y axes of the stage, the vertical and lateral etch depths, as well as the linewidth of the photoresist could be quantified. Multiple measurements were taken for each of these quantities and averaged to give the value seen in the dataset. Several qualitative factors about the etch, such as the relative isotropy/anisotropy of the profile and the surface roughness could also be noted using this setup.

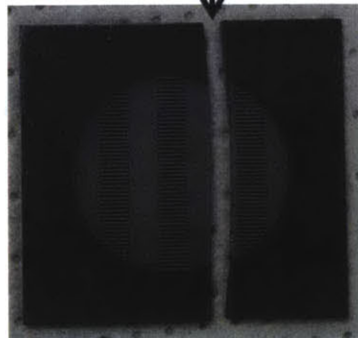

Figure 4.9: The standard cleavage plane for preparing samples for cross-sectional imaging.

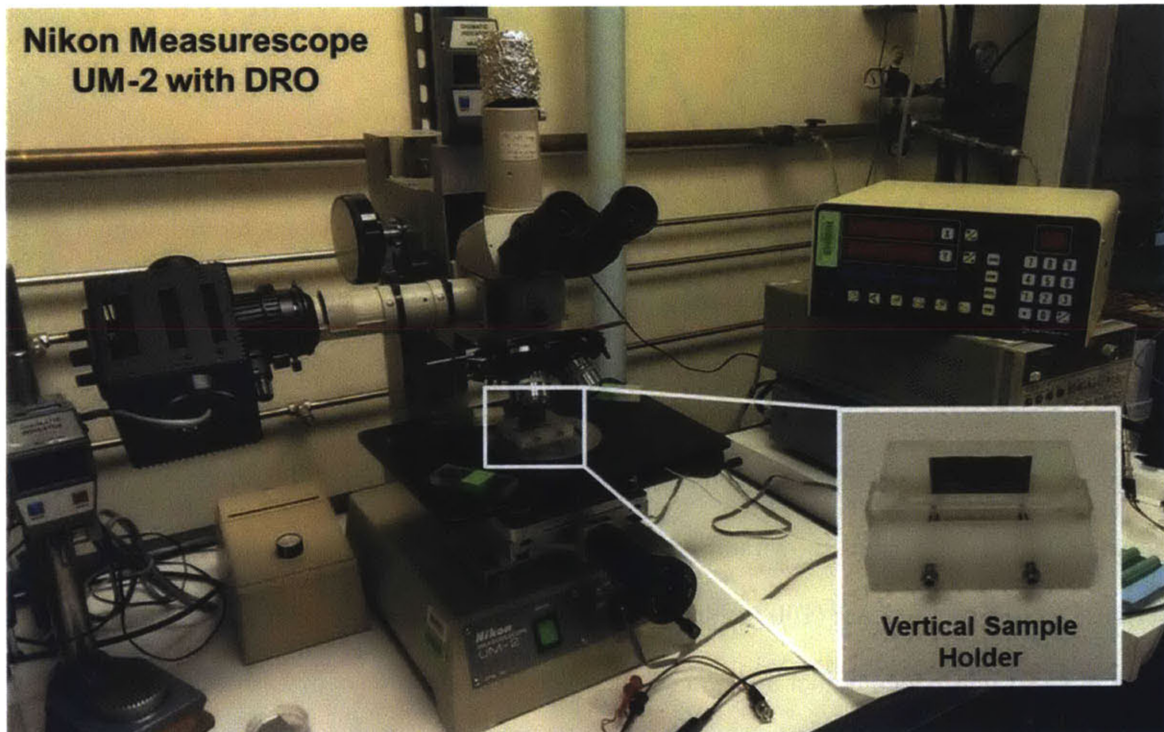

Figure 4.10: The Nikon Measurescope UM-2 setup used to measure the cross-sections of each sample. The inset shows a close-up view of the vertical sample holder used during imaging.

4.2.3.2 Surface Profilometry

To characterize the mask selectivity and the etch rate uniformity across the whole width of the sample, a Veeco Dektak 150 profilometer, housed in the Exploratory Materials Laboratory (EML) of MTL was used. This profilometer generates 1D scans of the height of the sample by dragging a thin stylus tip across the sample surface and measuring its deflection. The profilometer provides measurements of the surface height accurate to a few nanometers, but has geometrical limitations on the surfaces it can

measure. The stylus tip used to measure the surface heights has a conical profile and a nonzero tip radius (the tip radius used was 12.5 um, and the included cone angle was 45°, which means that stylus deflection can occur when features of a sample contact the side of the stylus as well as the tip). With a little math, it can be shown that these limitations lead to a maximum trench depth that can be measured for a given trench width. A handy equation for estimating this depth using the 12.5 μm tip radius styles is $Maximum\ Trench\ Depth = 1.2 * (Trench\ Width) - 20$. For the nominally 100 μm trench widths and the maximum RSM etch depth observed of 65 μm, the dimensions of the stylus did not present a problem. However, on the RSM samples where black silicon or silicon grass was present at the base of the etch (see **Section 2.3.3** for an explanation of this surface phenomenon), the locally large aspect ratios could prevent the stylus from reaching the actual bottom of the etch (this will be discussed in greater detail in **Section 4.3.3**). In samples without this extra surface roughness, the profilometer measurements of the trench depths agreed well with the Measurescope's vertical etch depth measurements. Four total scans of each sample were taken. **Figure 4.11** shows a picture of an etched sample with the locations of the four scan lines overlaid.

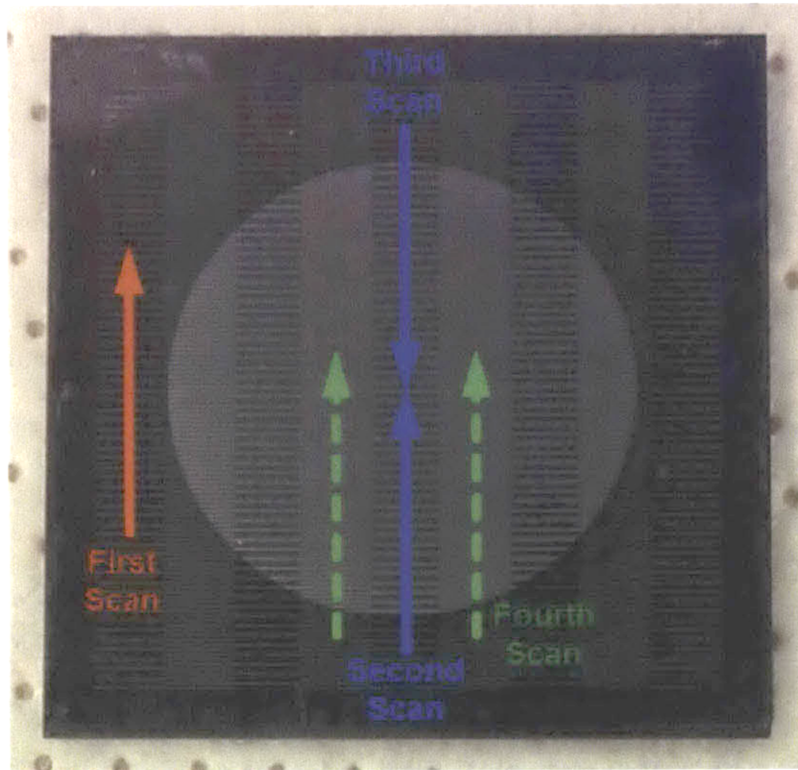

Figure 4.11: Etched sample with profilometer scan directions overlaid. Four scans were taken to provide an accurate assessment of the etch uniformity and mask selectivity.

Each scan length was 12 mm, with height measurements recorded every 500 nm (24,000 measurements per scan). The first scan taken for each sample was of the photoresist height in an unetched portion of the sample (the red line in **Figure 4.11**). This scan was used to provide a baseline for the measurement of the photoresist erosion in the etched region, which was then used to calculate the mask selectivity (the ratio of the silicon etch rate to the photoresist etch/erosion rate). The second scan started ~1 mm outside the etched region and moved perpendicularly across the etched trenches toward the center of the sample. The 12 mm (0.47") scan length ensured that measurements were taken beyond the halfway point of the etched region (the radius of the etched region for the RSM tests was 9.5 mm (0.375")). The third scan was identical to the second scan, except it began at the opposite end of the sample. Together, these two scans (the blue lines in **Figure 4.11**) provided a full picture of how the etch depth varied across a sample[18]. The fourth scan (at either of the dotted green lines in **Figure 4.11**) also started ~1 mm outside of the etched

[18] The second and third scans were not combined into a single scan due to data buffering and storage issues with the Dektak software.

region and traversed toward the middle of the sample, but along a path including the denser feature pattern. The purpose of including the ~1 mm region outside the etched region for the final three scans was to provide several lengths of bare silicon (the unetched trenches) to level the stylus trace across. Without this reference region, it would be very difficult to determine what tilt profile accurately fit the sample.

For analysis, the raw data from the leveled scans were imported into Microsoft Excel and a custom Visual Basic macro was used to generate graphs and histograms showing the results of the scans. From this data, the progression of the etch depth with distance across the sample and the relative photoresist erosion rate were determined for each sample.

4.2.3.3 Scanning Electron Microscopy

Fortunately, the relatively large length scales of the etched samples allowed much of the initial visual characterization to be performed quickly and simply with an optical microscope. When deeper inspection was required, scanning electron microscopes (SEMs) were used. Two SEMs housed in MIT's Center for Materials Science and Engineering (CMSE) Electron Microscopy Shared Experimental Facility (EMSEF) were used to visualize samples: a JEOL 5910 general purpose SEM and a Zeiss Merlin high-resolution SEM. Both of these SEMs offer full tilt and rotation of samples. The SEMs were used to better visualize the base and sidewall surfaces of the etched samples, which allowed more insight into the physical and chemical mechanisms occurring during the etch process.

4.2.4 Test Wafer Design

As mentioned in **Section 3.1.2**, the test samples used for the experiments of this thesis were formed by dicing 6" (150 mm) wafers. The specific size used during testing was 30 mm by 30mm. This size was chosen to easily allow for a full 1" round or 1" square (25.4 mm by 25.4 mm) area to be exposed, while still allowing some area around the edge for substrate clamping easy wafer handling. With this die size, 12 full 30 mm by 30 mm dies and 4 partial dies (missing a small amount of one corner) could fit on a

single 6" (150 mm) wafer. For processing in the 1" Fab DRIE, the patterned dies were mounted in the shallow recess at the top of the chuck assembly (shown in **Figure 3.9** in **Section 3.1.3**) and secured in place using an alumina clamping ring. The aperture cut into the alumina ring defines the exposed area available for etching. For the RSM test sequence, a 0.75" wide aperture was used. This limited exposure area was chosen to allow a portion of the patterned die to remain shielded from the etch. This portion was then used to provide a sample-specific baseline with which the etch properties could be compared.

To fabricate the dies for the RSM test sequence, a custom (dark field) mask pattern was designed. The individual die pattern contained an array of 100 μm wide by 8.5 mm long lines arranged to provide full (200 μm) pitch and double (400 μm) pitch spacing. **Figure 4.12** shows the mask layout with nested insets showing an individual die and a magnified look at the patterned trenches. Line-based patterns were chosen over other geometries to allow for clean and consistent cross sectional views once the dies were cleaved. To ensure that the dies always cleaved squarely across the lines, the mask was carefully aligned to the crystal structure of the wafer during patterning.

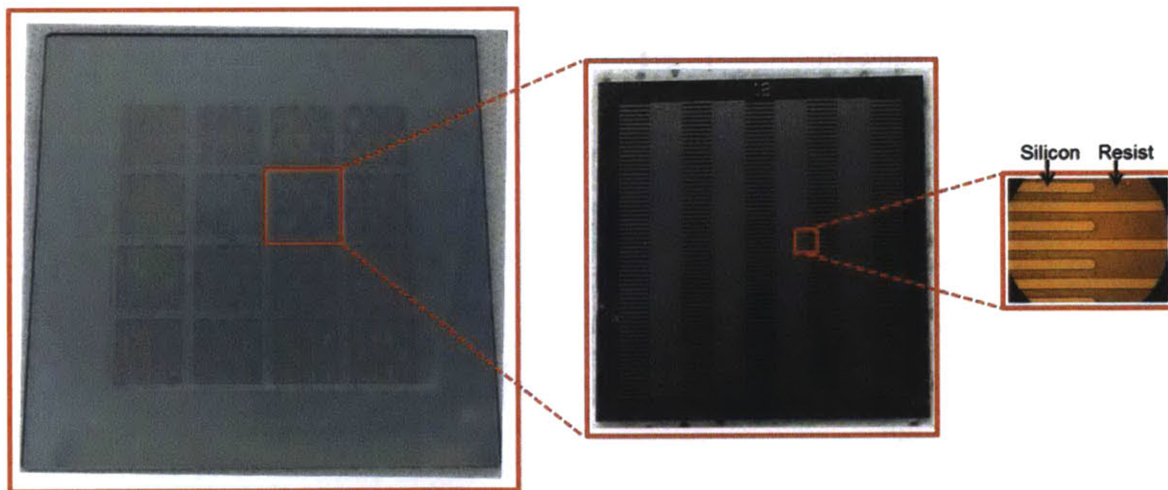

Figure 4.12: Mask design for the RSM tests. Moving from left to right, the first image is the full 7" mask with 16 individual dies, the second image shows a single die after dicing, and the third image shows the features on each die.

The dies for the RSM sequence were patterned using a conventional photolithography protocol in the Technology Research Laboratory (TRL) cleanroom of MTL. Briefly, the 7" mask created using the pattern described above was used to expose wafers coated with 10 μm of AZ4620 positive photoresist.

The thick 10 μm coating of photoresist was chosen to fully ensure that the mask would withstand the 15 minute etch times. Later analysis showed that the local photoresist height varied by ±1 μm.

After the patterned wafers were postbaked, a heat-release dicing tape was placed across the top of the wafer. This tape was applied to protect the dies from debris generated during the dicing process. After the dicing process, the wafers were placed in a 90°C oven for 10 minutes to release the protective tape. It should be noted that 90°C is 30°C lower than the specified reflow temperature of the AZ4620 photoresist.

4.3 SF_6 Etching Characterization

Analyzing the full set of data gathered from the RSM test sequence yielded some very useful knowledge about the performance of the 1" Fab DRIE and suggested several additional tests and potential improvements to the system. The results of this analysis are detailed and discussed in the following section.

4.3.1 RSM Data Analysis

The response surface portions of the data analysis of the 20-test CCC design were performed using **R** and the associated *RSM* package. The collection of quantitative data gathered using the techniques of **Section 4.2.3** was compiled and loaded into **R** with the factors coded in accordance to the formulas shown at the base of **Table 4.2**. The portion actively used for the following data analysis is shown in **Table 4.3** (the complete data set can be found in **Appendix F**. From the coded data set, the *rsm* function was used to fit the data to response surfaces. Through the parameters specified in the *rsm* function call, the type of surface fitting could be specified. The options available to *rsm* for fitting range from a full, second-order fit, which generates coefficients for linear terms, two-way interaction terms, and pure quadratic terms to a basic fit using just linear terms. A model fit with any combination of the term types is possible. In general, the best fit to the data was found using a second-order fit, which helps to justify the use of a full CCC design (rather than a simple factorial design) for the 1" Fab DRIE characterization.

The data object created by an *rsm* function call contains all of the information about the fit parameters for the selected response surface type. The fit parameters include an analysis of variance (ANOVA) table, and information specific to the type of surface fit (e.g. for a linear model it provides the direction of steepest ascent for further testing, and for a second-order model it provides information about the estimated stationary point of the surface). This data can be used for further analysis or plotting within the **R** environment, but for the following sections, the data for the fitted responses was imported into Mathematica, which provided additional options for data manipulation and visualization.

Standard Order Test	Block	SF_6 [sccm]	O_2 [sccm]	Base Power [W]	% O_2 in Total Flow	Vertical Etch Rate [μm/min]	Lateral Etch Rate [μm/min]	V/L Etch Rate Ratio	Mask Selectivity	APDM (Uniformity)	Etch Profile
1	1	1	0.25	5	20.0%	2.533	1.167	2.171	19.000	0.368%	Isotropic
2	1	1	0.75	15	42.9%	2.867	0.233	12.286	12.286	2.810%	Anisotropic
3	1	2	0.25	15	11.1%	3.867	1.833	2.109	33.143	0.634%	Isotropic
4	1	2	0.75	5	27.3%	4.333	0.933	4.643	52.000	0.524%	Anisotropic
5	1	1.5	0.5	10	25.0%	3.400	1.733	1.962	25.500	0.462%	Isotropic
6	1	1.5	0.5	10	25.0%	3.200	1.633	1.959	24.000	0.428%	Isotropic
7	1	1	0.25	15	20.0%	2.533	1.033	2.452	12.667	0.945%	Isotropic
8	1	1	0.75	5	42.9%	2.867	0.133	21.500	14.333	4.014%	Anisotropic
9	1	2	0.25	5	11.1%	3.867	1.800	2.148	38.667	0.820%	Isotropic
10	1	2	0.75	15	27.3%	3.867	2.033	1.902	29.000	0.462%	Isotropic
11	1	1.5	0.5	10	25.0%	3.400	1.600	2.125	22.667	0.395%	Isotropic
12	1	1.5	0.5	10	25.0%	3.400	1.833	1.855	29.143	0.588%	Isotropic
13	2	0.684	0.5	10	42.2%	2.000	0.167	12.000	8.000	3.854%	Anisotropic
14	2	2.317	0.5	10	17.7%	4.200	2.100	2.000	42.000	0.811%	Isotropic
15	2	1.5	0.092	10	5.8%	3.067	1.467	2.091	23.000	0.461%	Isotropic
16	2	1.5	0.908	10	37.7%	3.400	0.267	12.750	20.400	3.921%	Anisotropic
17	2	1.5	0.5	1.8	25.0%	4.000	0.400	10.000	60.000	0.740%	Anisotropic
18	2	1.5	0.5	18.2	25.0%	3.400	1.667	2.040	22.667	0.700%	Isotropic
19	2	1.5	0.5	10	25.0%	3.467	1.600	2.167	24.471	0.512%	Isotropic
20	2	1.5	0.5	10	25.0%	3.333	1.633	2.041	25.000	0.361%	Isotropic

Table 4.3: Selection of results from the RSM sequence. The factors are shown in blue and the results in green.

4.3.2 Vertical Etch Rate

The first and arguably most important response analyzed was the vertical etch rate of the samples. The data for the vertical etch rate was taken using the Nikon Measurescope microscope setup and confirmed where possible (on samples without excess roughness) by profilometry. A second-order fit of the data provided the best fit (Lack of Fit: $p = 0.292$), and is shown below in **Figure 4.13**[19].

[19] For the calculation of the surface plots in **Figure 4.13** and all subsequent figures, the unused independent variable (e.g. base power for **Figure 4.13a**) was set to the center point value for the factors (1.5 sccm for SF_6, 0.5 sccm for O_2, 10 W for base power) and the center point value of the block effect (1.4, calculated from the number of tests in each block: $(12\ Tests)(1) + (8\ Tests)(2)/(20\ Total\ Tests) = 1.4$ unless otherwise noted on the Figure.

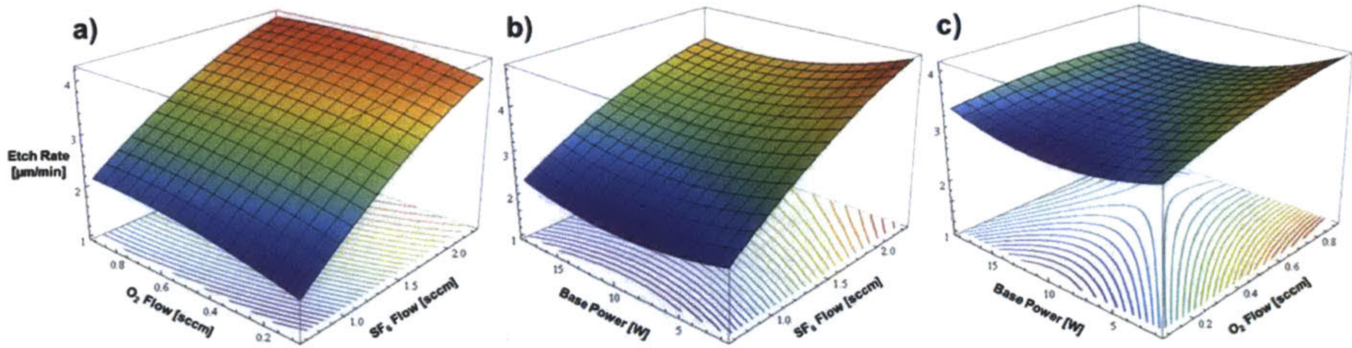

Figure 4.13: Vertical etch rate response surface plots for each two parameter combination in the three factor test sequence. Contour plots of the same data can be seen below each surface. **a)** displays SF_6 vs. O_2, **b)** displays SF_6 vs. base power, **c)** displays O_2 vs. base power.

$$\textbf{Etch Rate} = 2.842(SF_6) + 2.070(O_2) - 0.063(BP) - 0.200(SF_6)(O_2) - 0.023(SF_6)(BP) - 0.047(O_2)(BP) - 0.400(SF_6)^2 - 0.800(O_2)^2 + 0.005(BP)^2 + 0.035 \quad (4.1)$$

$$\textbf{\textit{For}}: \quad Etch\ Rate\ [\mu m/min], \ \ SF_6\ [sccm], \ \ O_2\ [sccm], \ \ BP\ [W]$$

From these plots several things are immediately apparent. First, the SF_6 flow has by far the biggest effect on the etch rate. Since the SF_6 flows are relatively small[20], this is a simple point to accept, and it shows that the fluorine etch process is, in all likelihood mass transport limited rather than reaction rate limited. This is due to the high reactivity of fluorine radicals with silicon atoms and the high volatility of the SiF_4 product molecule. The point is further driven home by grouping the samples with identical O_2 flows and base powers and then plotting the vertical etch rate versus the SF_6 flow rate. This is done in **Figure 4.14**.

[20] The SF_6 flows in the RSM tests are small compared to the flows seen in commercial etchers, even when accounting for the size difference (V). This is because commercial etchers use very large turbo pumps and sophisticated pressure controllers to achieve short residence times (10s to 100s of ms) ($Residence\ Time = PV/Q$). The fast reaction and desorption time of the $Si + 4F \rightarrow SiF_4$ reaction permits these shorter residence times. The large turbo pumps used can maintain the low pressure (P) needed for etching while operating at very large gas flows (Q). The gas residence times for the 1" Fab DRIE during the RSM sequence were ~1-1.5 seconds.

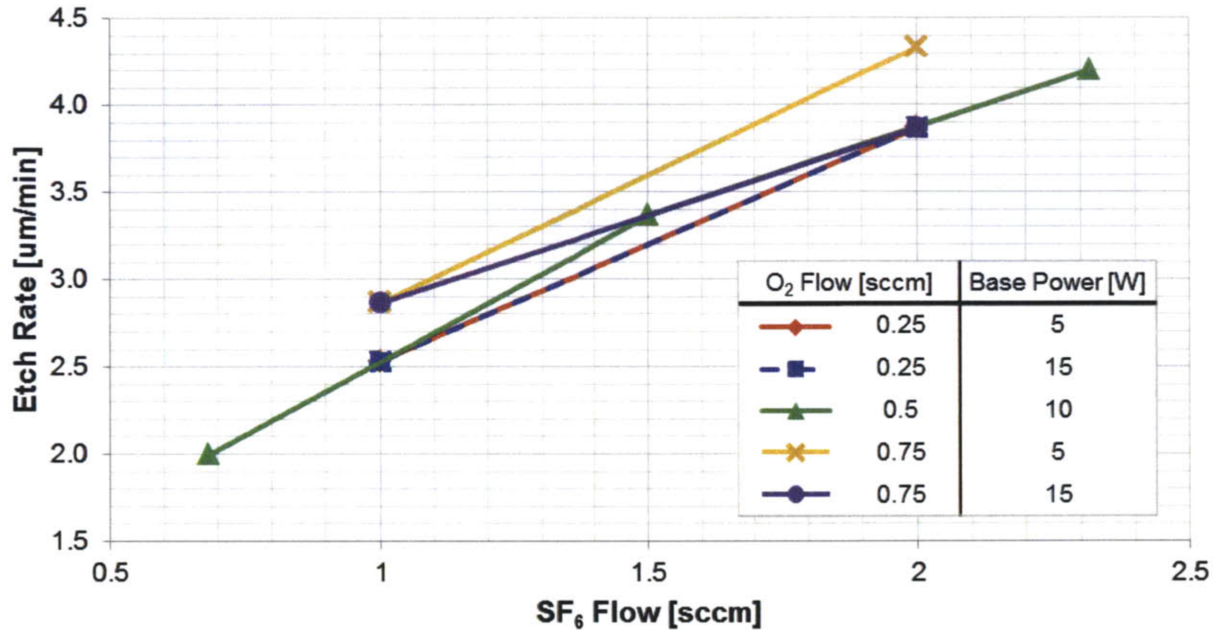

Figure 4.14: SF6 vs. etch rate for five different groups of O2 flow and base power. The 0.5 sccm O2 and 10 W base power grouping uses the average etch rate value for the six center point tests.

The positive correlation between SF_6 flow and vertical etch rate holds across all 5 parameter groups. Furthermore, among the five groups all of the different types of etch profiles are represented. The 0.25 sccm O_2 / 5 W base power and 0.25 sccm O_2 / 15 W base power groups show only isotropic profiles, the 0.75 sccm O_2 / 5 W base power group shows only anisotropic profiles, and the remaining two groups show a mix of profile types. This shows that no matter the etch profile or the combination of other factors, increasing the SF_6 flow will increase the etch rate, which agrees with the established theory.

The effect of the O_2 flow is a bit less clear. Increased O_2 flow shows a moderately positive effect on increasing the etch across the full range of SF_6 flows, and another moderately positive effect at low base powers, but very little effect at higher powers. The synergistic effect with SF_6 agrees with the literature (as discussed in **Section 2.3.3** oxygen helps catalyze the production of fluorine radicals in the plasma). Like the previous observation relating the SF_6 flow and the etch rate, the relationship between O_2 flow and the etch rate can be further examined by plotting groups of data that differ only in the quantity of O_2 used. This figure is shown below.

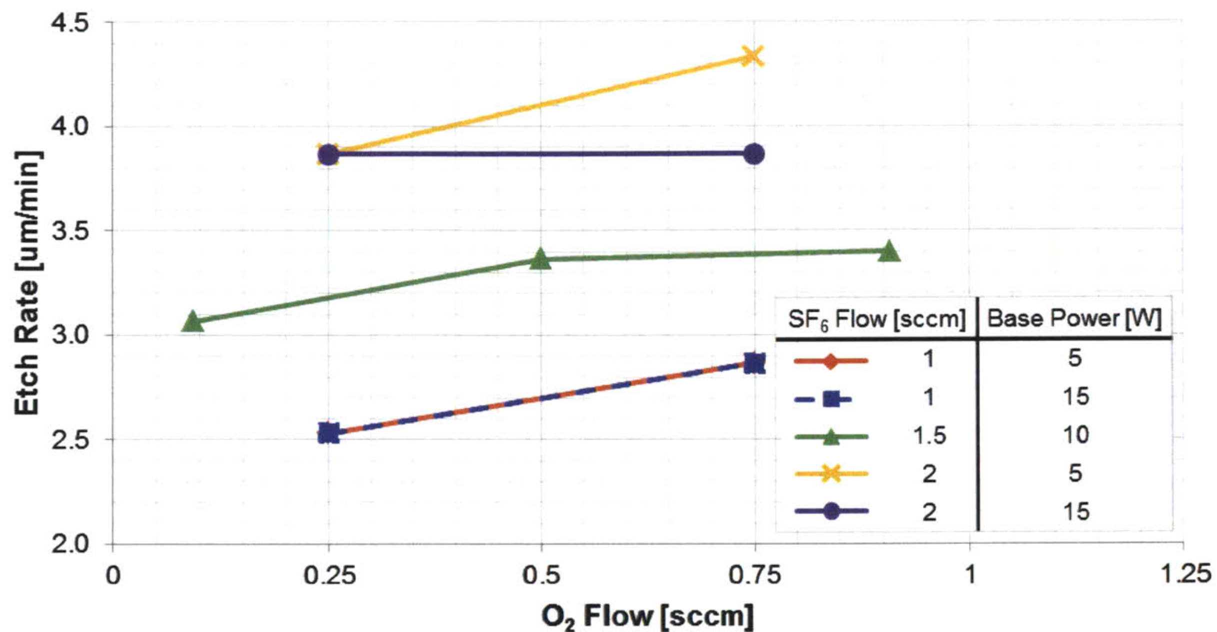

Figure 4.15: O_2 vs. etch rate for five different groups of SF_6 flow and base power. The 1.5 sccm SF_6 and 10 W base power grouping uses the average etch rate value for the six center point tests.

As **Figure 4.15** shows, four of the five parameter groups exhibit higher etch rates with increased O_2 flow. The fifth group, which corresponds to a large SF_6 flow and a large base power, shows no effect for different O_2 flows, but this combination of parameters does correspond to a pair of the flattest regions of the original response surface curves (the high SF_6 flow region of **Figure 4.13a** and the high base power region of **Figure 4.13c**), suggesting that there may be a limit to the positive effect of oxygen addition as the SF_6 flows and applied base powers increase.

The 1" Fab DRIE's response to changing base power was the most surprising of the three factors tested in the RSM sequence. The RSM data show that etch rates are the lowest near 10 W of power, and increase only slightly for powers both above and below 10 W. The suggested maximum etch rate occurs at the higher end of the SF_6 and O_2 flow rate ranges with low base powers. This is a bit of a counterintuitive result, as increased base powers are associated with larger ion energies, which should assist the etching process [39]. Looking back at the raw data, we can see that this is not just an aberration from the fitting process, as the grouped data points (fixed SF_6 and O_2 flows, varying base powers) in **Figure 4.16** show.

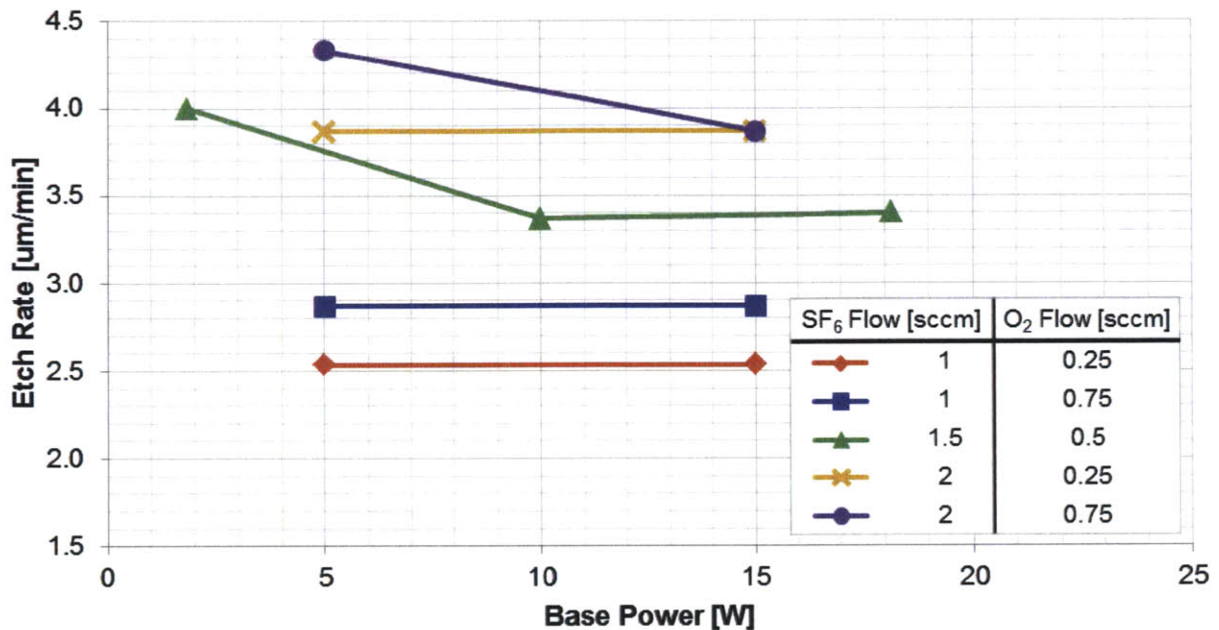

Figure 4.16: Base power vs. etch rate for five different groups of SF_6 flow and O_2 flow. The 1.5 sccm SF_6 and 0.5 sccm O_2 base power grouping uses the average etch rate value for the six center point tests.

Three of the five groups exhibited no base power effect, and of the two with some variation, the trend is to higher etch rates with lower base power. Interestingly, the two instances where a decreased base power produced a larger etch rate (the leftmost points of the green and purple traces) make up two of three largest etch rates observed across all tests[21] and also coincide with the transition from an isotropic etch profile to an anisotropic etch profile. These isotropic-to-anisotropic profile changes are the only two such transitions (in either direction) that occur within the constant gas flow test groups.

Combined with their large etch rates, these two samples certainly suggest that an unexpected base power mechanism is in play. The typical role for base power in an ICP-RIE is to control the ion energies and directionality. In this role, increased base power generates larger and more focused ion energies, which assist etching by providing extra energy for chemical reactions and also by providing a measure of physical sputtering. Further discussion of the two samples in question, as well as possible explanations of the observed base power effect is included in **Section 4.3.4**.

[21] The top 3 etch rates observed were 4.33 μm/min for standard order test (SO) #4 (2 sccm SF_6, 0.75 sccm O_2, 5 W base power), 4.2 μm/min for SO #14 (2.317 sccm SF_6, 0.5 sccm O_2, 10 W base power), and 4.0 μm/min for SO #17 (1.5 sccm SF_6, 0.5 sccm O_2, 1.8 W base power).

Building on the positive effects seen for both SF_6 and O_2 flow, one interesting point to explore is the effect of the relative fraction of O_2 on the observed etch rate. This fraction was one of the motivating factors in choosing the RSM design center point and the delta points (in combination with its possible effects on the etch profile), and the etch rate versus this fraction is a common graph to find in academic papers or course lectures about the SF_6+O_2 etching system [11,12,14]. The 20-test RSM performed on the 1" Fab DRIE does not have a specific set of tests that can be used to directly build such a curve (a maximum of three tests exist for a constant SF_6 flow rate and base power). By using the response surface generated by the RSM test however, this curve can be approximated (as the response surface is just a continuous model of the etch rate of all possible parameter combinations). This is simply done in software like Mathematica by taking the response surface equation (**Eqn. 4.1**), and plotting its estimated etch rate (for a given SF_6 flow and base power) over the percentage of O_2 in the total gas flow. This plot is shown in **Figure 4.17**. Also shown alongside the plot is a selection of the ideal oxygen percentages for different parameter combinations as predicted by the response surface.

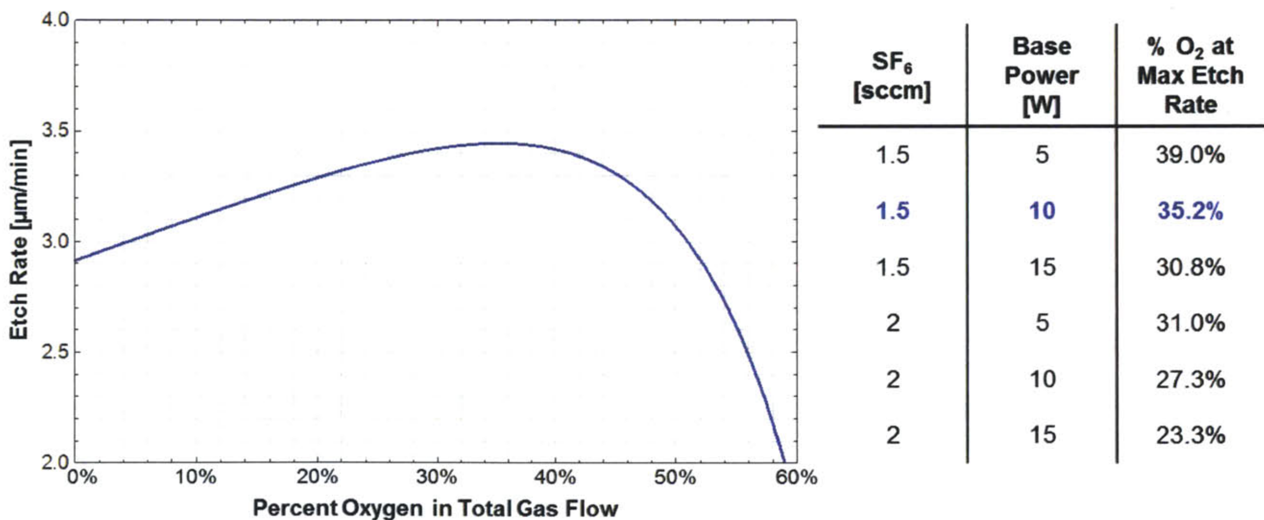

SF_6 [sccm]	Base Power [W]	% O_2 at Max Etch Rate
1.5	5	39.0%
1.5	10	35.2%
1.5	15	30.8%
2	5	31.0%
2	10	27.3%
2	15	23.3%

Figure 4.17: The expected etch rate vs. percent O_2 in the total gas flow as calculated using the fitted response surface equation (for an SF_6 flow of 1.5 sccm and a base power of 10 W). The oxygen fraction at the estimated peak etch rate for several different combinations of SF_6 flow and base power are included in the table on the right.

At a basic level, the first takeaway from the information in **Figure 4.17** is that the response surface model does indeed predict the existence of an ideal percentage of O_2 flow for achieving the maximum etch rate. Since this is a well-documented feature of SF_6+O_2 etching systems, this alone is a good point of

confirmation for the model itself. Secondly, the predicted values for the ideal O_2 percentages agree quite well with the actual values seen in the literature. This provides more confirmation to the model, but also to the performance of the system itself, and suggests that the same mechanisms that occur in commercial etching systems are also occurring in the 1" Fab DRIE.

4.3.3 Spatial Uniformity of Etch Rate

The next response investigated was the spatial uniformity of the etch rate across the samples. For the end user of an etching system, this is arguably even more important than the actual etch rate, as it is much more difficult to compensate for a spatially varying etch rate than it is for a time-varying or inconsistent (but spatially uniform) etch rate. In practice, fully uniform etch rates across an entire substrate are very difficult to achieve due to a variety of factors including local variations in the substrate temperature, aspect-ratio dependent etching (ARDE) or RIE lag, and electric field or shadowing effects from the etch mask or clamping mechanism. Nevertheless, uniformity within a few percent across an entire wafer is acceptable for most applications and can readily be achieved in modern commercial etching systems.

The characterization of the etch uniformity for the 1" Fab DRIE was carried out by analyzing the profilometry data gathered for each sample (refer to **Section 4.2.3.2** for details). The primary mode of analysis was calculating the etch rates for each trench across the width of a sample (47 trenches per 0.75" sample width) and then comparing these rates to the average rate seen for the sample. In all of the samples analyzed, there were clear edge effects stemming from shadowing by the 1 mm thick alumina sample clamp. This shadowing caused a diminished etch rate for the first 1 to 1.5 mm of the exposed area. To assess the effect of the etching environment and etch parameters, rather than the effect of a substrate clamp, this edge area was not included in the analysis. This decision is similar in effect to the common practice of purposefully planning not to use an outer section of a substrate[22]. The edge area was excluded by removing the outer eight trenches (four on each side) from the analysis. Four trench widths

[22] "Edge Exclusion" is a parameter specified in the International Techology Roadmap for Semiconductors (ITRS), and currently sits at 2 mm for front-end processes like plasma etching [43].

corresponds to an approximately 1.6 mm wide ring (depending on the exact placement of the alumina clamp) being excluded from the etched area. With these exclusions, the dataset for etch rate uniformity contains etch rate values for the middle 39 trenches for each of the 20 samples in the RSM test sequence. Several quantities were calculated from this raw data, including the average etch rate for each sample, the standard deviation of the etch rate across the sample, and the average percent deviation rate across the sample. This final value is the most useful number, as it provides an etch rate-independent look at a sample's uniformity. This quantity was calculated according to the following formula:

$$Average\ \%\ Deviation\ from\ the\ Mean = APDM = \left(\frac{1}{N}\sum_{i=1}^{N} |ER_i - ER_{Mean}|\right) \Big/ ER_{Mean} \quad (4.2)$$

The APDM for each sample was calculated and analyzed against the three RSM test factors for any potential relationships. There are no readily discernible connections to the individual factors or suitable models fits for all three factors, but when the APDM is plotted versus the percentage of oxygen in the total gas flow, a very clear relation emerges. This plot is shown below as the red series in **Figure 4.18**.

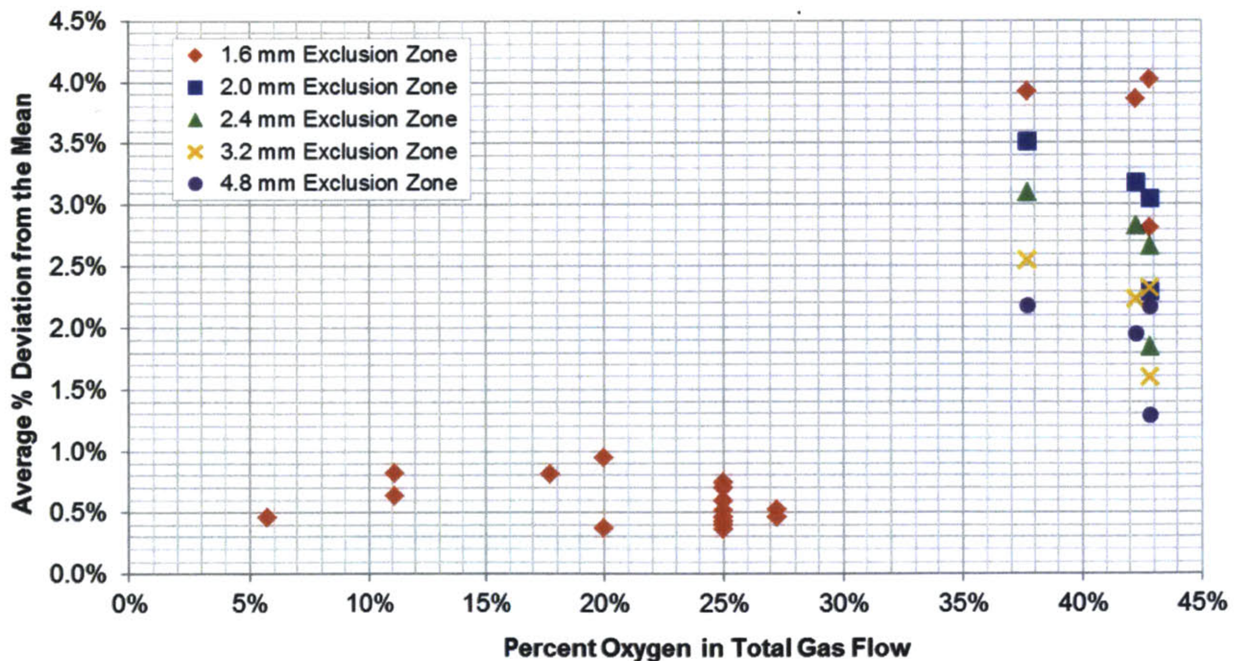

Figure 4.18: Average percent deviation from the mean (APDM) vs. the fraction of O_2 in the total gas flow. The data for all 20 RSM samples is plotted at the standard exclusion zone length of 1.6 mm. Data for the four outlying samples is also shown using increasingly larger exclusion zones.

Two observations can immediately be made from this scatter plot. The first is that the etch rate uniformity is generally quite good, with 80% (16/20) of the samples showing an APDM of less than 1%. On the scale of the full etch depths observed for each sample, this corresponds to an average deviation of just ~200-500 nm. These 16 samples, which were processed using a variety of base powers (2 W to 18 W) and gas flows (total flows ranging from 1.25 sccm to 2.8 sccm and O_2 fractions between 6% and 27%), indicate two encouraging things about the conditions in the etch chamber. Firstly, the samples' high degree of spatial uniformity is evidence that a radially uniform distribution of reactants is being transported to substrate and that transport of etch products away from the substrate is similarly uniform. This helps to validate the design of the process gas distribution system and the decision on the coil-chuck spacing. Secondly, the etch rate uniformity suggests that there are no major temperature gradients across the substrate, as etch rate is temperature dependent [9,39]. This suggests that the substrate cooling system (chilled water flowing through the chuck with thermal grease used as a heat transfer medium between the substrate and chuck) is working as designed and dissipating heat from the substrate uniformly.

The second observation from **Figure 4.18** is that appreciably more deviation (lower uniformity) exists in the samples with the highest oxygen fractions (the red points with a ~37% to ~43% oxygen fraction). Examining the data for these four samples shows that a sizable portion of these samples' nonuniformity stems from wider-than-normal edge effects. For most of the samples, edge effects are negligible once inside the four trench (~1.6 mm) exclusion ring. In these four samples, however, the transition region is much longer. To grasp how this extended transition region affects the APDM values, **Figure 4.18** also shows the APDM calculated using several larger exclusion regions (5, 6, 8, and 12 trenches, or ~2 to ~4.8 mm) for the four high O_2% samples. As the data show, increasing the exclusion does help to screen out some of the nonuniformity, but even with the most extreme exclusion zone, all four samples still display a larger APDM than any of the sample with lower oxygen fractions.

Re-examining these four samples in the context of the full dataset helps elucidate the reasons for this increased etch rate variation. In addition to having the four largest APDM values, these four samples also

have the four largest vertical to lateral etch rate ratios (VLERR). A high VLERR is indicative of an anisotropic sample, which the cross-sectional microscope images of these samples confirms. The calculation and interpretation of the VLERR statistic is discussed in more detail in the next section (**Section 4.3.4**). These images for the four samples in question are compiled below in **Figure 4.19**.

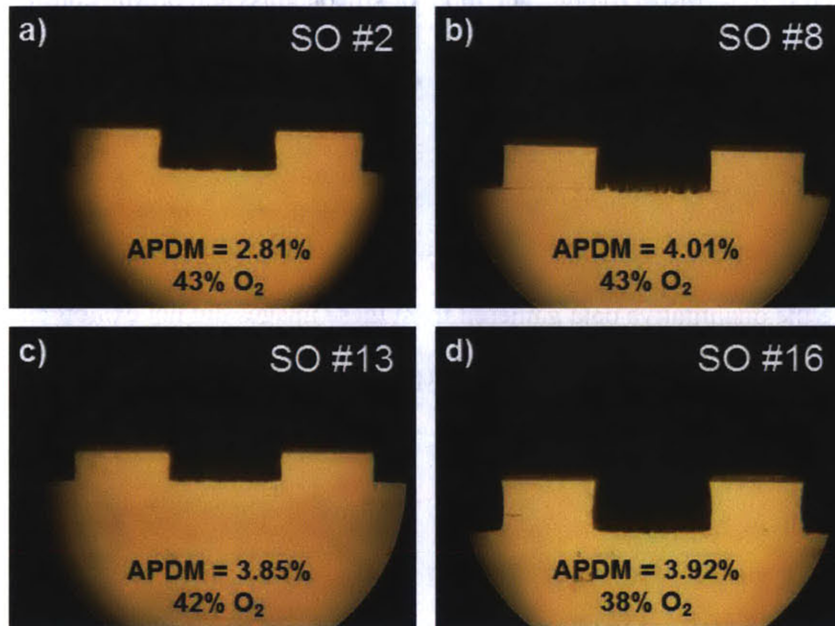

Figure 4.19: Cross-sectional images of the four samples with large APDM values. The samples all display an anisotropic profile and silicon grass.

From the images it is seen that the four samples in question also have another shared characteristic: silicon grass structures. As briefly discussed in **Section 2.3.3**, silicon grass (or "black silicon"), can occur when small amounts of polymeric material deposit on the surface of the etch and act as microscale masks for the etch process. The polymeric deposits can be generated from the readsorption of etched or sputtered mask material or from the formation of $Si_xO_yF_z$ compounds (the very same compounds that provide the sidewall passivation that helps enable anisotropic SF_6+O_2 etching). This silicon grass represents a different, but important source of etch rate nonuniformity: etch roughness. Depending on the specific path taken by the profilometer stylus through each trench, it may encounter more or less "blades" of silicon grass, which affects the measurements for that trench. From an end-user perspective, the general randomness of the heights and placement of the grass blades is very undesirable, making it difficult to achieve consistent device properties across a substrate.

To prove the exclusivity of grass to high O_2 fraction samples, the 16 remaining samples of the RSM sequence were inspected. Grass was not found on any of these 16, including the two other samples with profiles identified as anisotropic. These two samples (SO #4 and SO #17) were highlighted in the analysis of the base power effect on the etch rate, and have O_2 percentages of 27% and 25%, and APDM values of 0.52% and 0.70%, respectively. The topic of silicon grass and profile control is discussed further in the following section.

4.3.4 Etch Profile

The etch profiles were analyzed using cross sectional images taken using optical and scanning electron microscopy. While the quantitative data gathered from these images did not exhibit any statistically significant first or second order fits to the three RSM factors, several important relationships could still be discerned from both the raw data and the qualitative properties observed in the images.

4.3.4.1 Anisotropy

The strongest relationship determined from the microscopy data suggests that lower SF_6/O_2 ratios (or large O_2 fractions) lead to anisotropic profiles. This was alluded to in the previous section, and was also one of the hypotheses that guided the selection of the values for RSM test sequence. To visualize the SF_6/O_2 ratio effect on the etch profile, **Figure 4.20** displays two different sets of three etches with varying O_2 percentages. In the first set (**Figure 4.20a-c**), the O_2 flow and base power are held constant at 0.5 sccm and 10 W, and the SF_6 flow is varied from 2.32 sccm down to 0.68 sccm. In the second set (**Figure 4.20d-f**), the SF_6 flow and base power are held constant at 1.5 sccm and 10W, and the O_2 flow is varied from 0.91 sccm down to 0.09 sccm. The middle point for both sets of tests is a center point (1.5 sccm SF_6, 0.5 sccm O_2, 10 W base power). The specific factor values used and the O_2 percentage for each sample are displayed below their profiles.

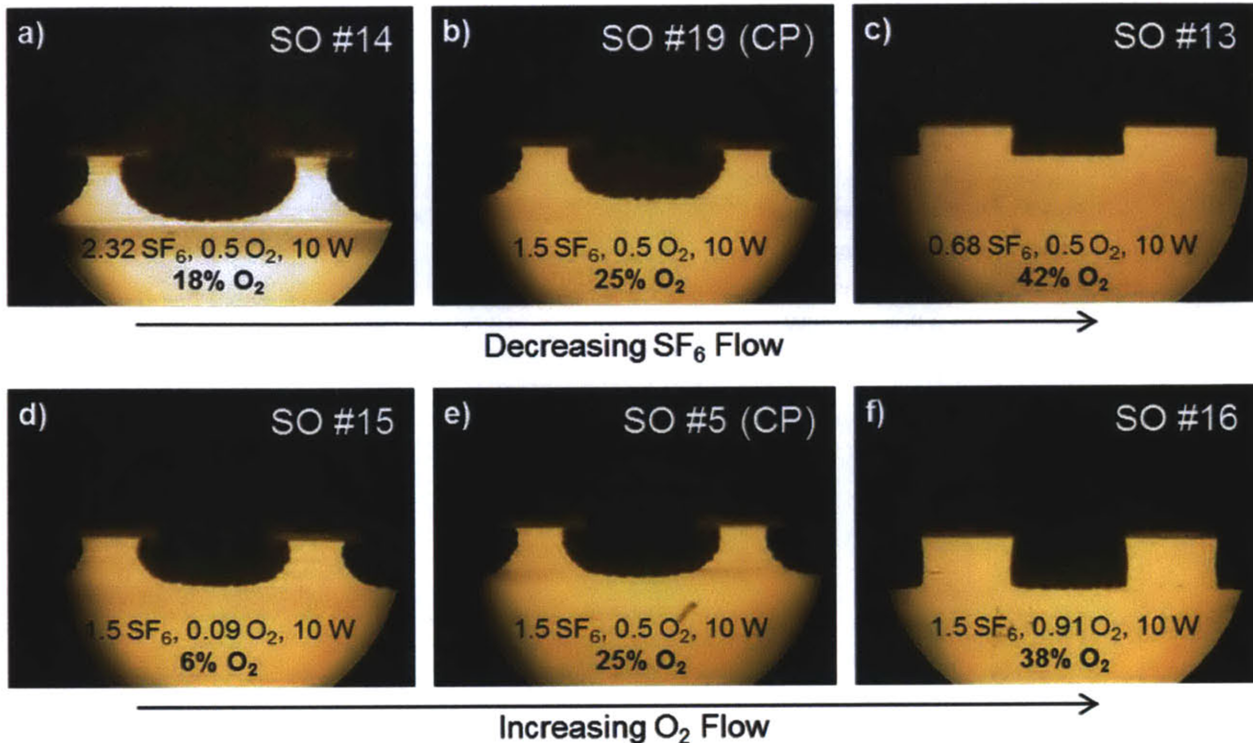

Figure 4.20: The effect of increasing O_2 fractions on the etch profile. **a)-c)** show a group of samples with constant O_2 and base power, but decreasing amounts of SF_6 (thus increasing the O_2 fraction). **d)-f)** show a second group with SF_6 and base power held constant and the amount of O_2 increased.

Both groups of tests shown in **Figure 4.20** show that increasing the O_2 fraction eventually leads to an anisotropic profile.

The trends shown in the cross-sectional images were quantified by determining the lateral etch rate for each sample (calculated at the widest portion of the etch depth), and then combining these values with the vertical etch ratio to form the vertical to lateral etch rate ratio (VLERR)[23] for each sample (This is same statistic mentioned briefly during the spatial uniformity section). This data is plotted in **Figure 4.21**. The data in this figure are broken down in two stages. The first stage splits the data into isotropic samples (shown in blue) and anisotropic samples (shown in red). These two groups are then further split into three subgroups (shown as different marker shapes) that classify the base power used for the sample. The

[23] The calculation of the VLERR is equivalent to the calculation of 1/Aspect Ratio. Aspect ratio, however is generally reserved for discussion of anisotropic features, and so for the combination of isotropic and anisotropic profiles discussed in this chapter, using VLERR makes a bit more sense. Some investigators have called used the value (1-VLERR) and called it the "anisotropy" of the sample [15], but this provides complications in terminology when speaking qualitatively about the etch profile.

distinction between the isotropic and anisotropic classifications (for this plot and all other discussions involving the type of etch profile) was determined by visual assessment of the curvature of the sidewalls.

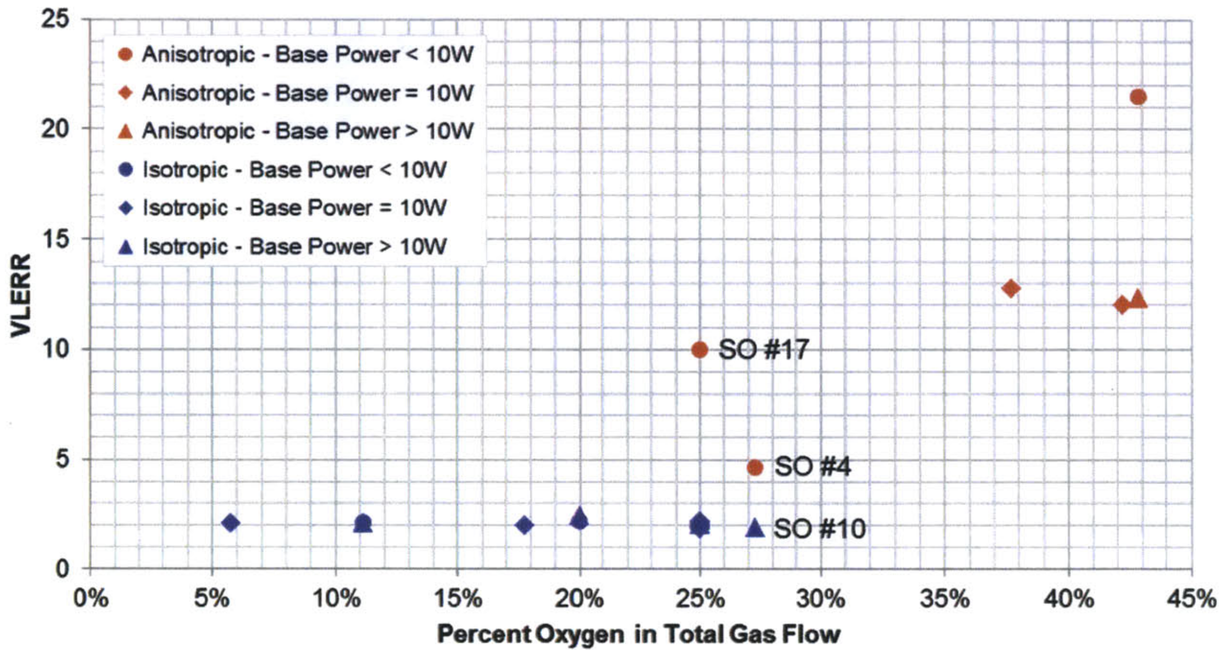

Figure 4.21: Vertical to lateral etch rate ratio (VLERR) vs. the fraction of O_2 in the total gas flow. The data is split by profile type (isotropic in blue and anisotropic in red) and by the amount of base power used in each test. Three samples near the transition point between low and high VLERR are labeled and discussed further in the text.

From the data in **Figure 4.21**, three conclusions can be drawn. The first and most obvious is that the isotropic samples have much higher lateral etch rates than anisotropic samples, and thus have the lowest VLERR values. This difference in lateral etch rates can clearly be seen from the relative amount of mask undercut in the cross-sectional images of **Figure 4.20**. The second conclusion is that base power appears to have very little effect on the profile. As stated in the previous sections, this runs counter to the hypothesized base power mechanisms. One potential reason for the lack of an expected base power effect may be that the powers applied, while comparable in absolute value to the powers used in commercial systems, represent significantly larger areal power densities (due to the smaller size of the substrate electrode in the 1" Fab DRIE). This extra power density (2-6 W/cm^2 compared to <1 W/cm^2 in ICP-RIE systems like the STS Multiplex ICP) may have caused excessive ion bombardment, which would increase the substrate temperature and lead to diminished etch rates [9,39].

The final conclusion that can be drawn from the VLERR data is that, at minimum, a 25% O_2 fraction is needed to form anisotropic profiles, and that by ~37% O_2, these profiles will form readily. Unfortunately the RSM data does not include any test results for O_2 fractions between 27% and 37%, so a more precise estimate of the transition ratio or fraction is not possible. The general ranges, however, do provide reference points for future parameter selection in DRIE processes.

Complicating this isotropic / anisotropic delineation however are the samples with 25% and 27% O_2 (the labeled samples in **Figure 4.21**). At both fractions, there are instances of isotropic and anisotropic profiles. At 25% O_2, there are eight samples, seven of which have a consistent VLERR around 2 (these correspond to the six center points and standard order test #18 (SO #18, not labeled), which used the extreme base power level of 18 W). The eighth sample (SO #17) was a star test carried out using the extreme low base power of 2 W. The cross-section of this test is shown in **Figure 4.22a**. The two 27% O_2 samples correspond to the high gas flow (2.75 sccm SF_6, 0.75 sccm O_2) tests in the factorial block. The anisotropic sample (SO #4, VLERR = 4.6) used 5 W of base power and has its cross-section displayed in **Figure 4.22b**. The isotropic sample (SO #10, VLERR = 1.9) used 15 W of base power and is shown in cross-section in **Figure 4.22c**.

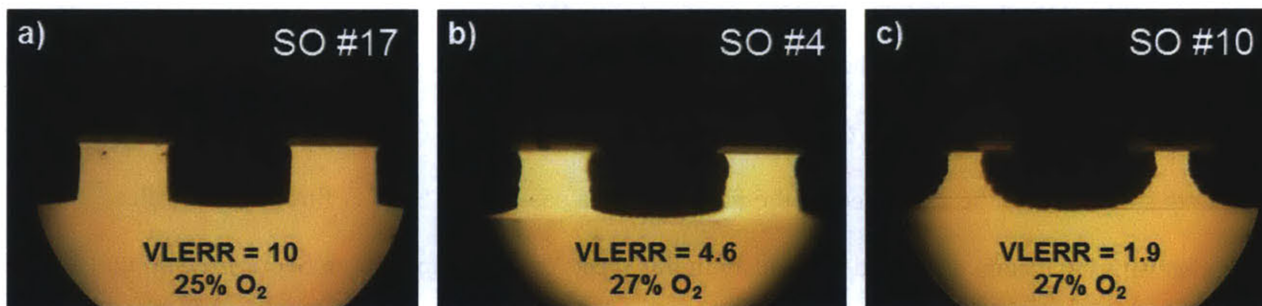

Figure 4.22: Cross-sectional images of the three labeled samples from the transition region of **Figure 4.21** (VLERR vs. oxygen fraction). The profile of **b)** appears to be in between the clearly anisotropic SO #17 in **a)** and the clearly isotropic SO #10 in **c)**.

Up until this point, the etch profiles of the RSM samples have been characterized using the binary anisotropic or isotropic classification. The cross sectional views in **Figure 4.22** however, show three different sidewall profiles. SO #17 and SO #10 show the stereotypical anisotropic and isotropic profiles, respectively. SO #4, on the other hand, while officially classified as anisotropic because of its reasonably

straight sidewalls and squareness at the base, has a few isotropic tendencies, like the mild curvature near the top of the etch. No other samples in the RSM sequence showed a profile like SO #4 (they all fit much more clearly into anisotropic or isotropic category) and the quantitative VLERR value of 4.6 for SO #4 backs this up. Looking back to **Figure 4.21**, the VLERR values for isotropic etches range from 1.85 to 2.17, and the VLERRs for everything but SO #4 are 10 or higher.

If we disregard the result of the single ultra-low base power test (SO #17, just 2 W of base power applied), this suggests then that 27% O_2 may be near the true transition point between anisotropic and isotropic profiles for the SF_6+O_2 etching system in the 1" Fab DRIE. The original hypothesis (from **Section 4.2.1**) for this transition region was for a 25% O_2 fraction, and so the 27% O_2 fraction fits nicely with this prediction.

4.3.4.2 Surface Properties

All of the etches in the RSM displayed some measure of surface roughness. For isotropic etches the surfaces were uniformly rough and for the anisotropic etches the side walls were smooth and the bottom surfaces had silicon grass (the two exceptions to this characterization were the fringe cases of SO #17 and SO #4, which were discussed in the preceding section). SEM images of the two different surface types are shown in **Figure 4.23**. For the anisotropic samples (like SO #16, which is shown in **Figure 4.23a-b**), the formation of silicon grass on the trench bottom occurs due to the micromasking phenomenon, and the smooth sidewalls can be explained by the formation of a passivating $Si_xO_yF_z$ film. Both of these mechanisms have been discussed previously in this thesis (most completely in **Section 2.3.3**) and also in the literature [9]. The surface roughness observed in the isotropic samples (like the center point sample (SO #19) shown in **Figure 4.23c-d**) is well documented in the literature [14,40,41] and its mechanism has been suggested as a similar but less severe version of micromasking (due to a decreased fraction of O_2, which is needed to form the passivating $Si_xO_yF_z$ molecules and cause mask erosion and redeposition) [14] or potentially as a result of a combination of processing pressure in the 10s of mTorr and using alumina as a chamber material [42].

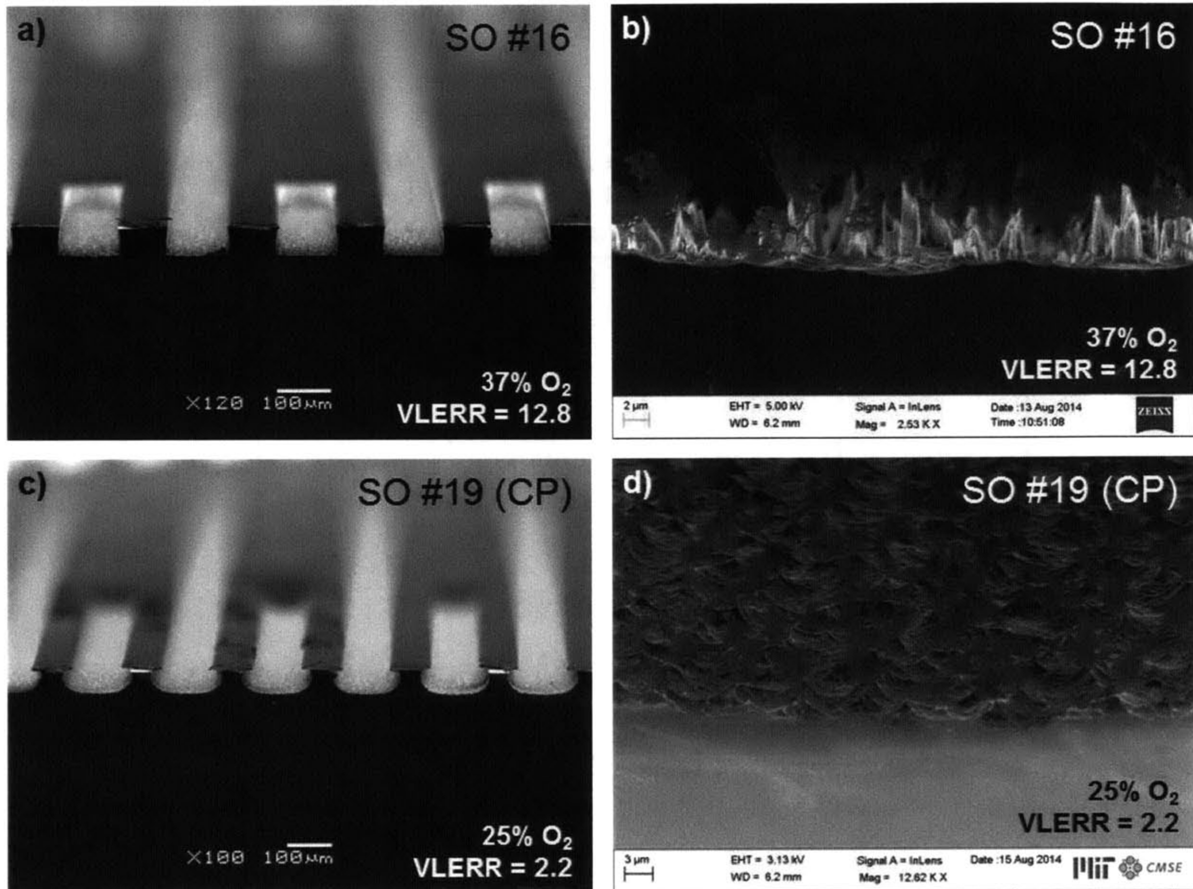

Figure 4.23: SEM images of two samples showing different roughness profiles. **a)** and **b)** show SO #16, which has an anisotropic profile and exhibits silicon grass, while **c)** and **d)** show SO #19, a center point run with an isotropic profile and mild roughness at the base of the etch.

4.3.5 Center Point Repeatability

During the 20 test RSM sequence, six center point tests were performed. In this section, the results of these center point tests are compared. Above all else, an etching system should produce the same results with the same input parameters, and with these center point test results, the 1" Fab DRIE's ability to do just that can begin to be assessed.

For the repeatability assessment, five etch characteristics were compared: the vertical etch rate, the lateral etch rate, the VLERR, the mask selectivity, and the etch rate uniformity. **Table 4.4** contains the values for these characteristics for each of the six center points and several statistical measures. The etch rate

uniformities are presently separately later[24]. To account for the numerical differences in the quantities, the normalized quantity of percent deviation from the mean was selected for plotting in **Figure 4.24**.

	Standard Order	Vertical Etch Rate [μm/min]	Lateral Etch Rate [μm/min]	V/L Etch Rate Ratio (VLERR)	Mask Selectivity
1	5	3.4000	1.7333	1.9615	24.3000
2	6	3.2000	1.6333	1.9592	23.5500
3	11	3.4000	1.6000	2.1250	21.6889
4	12	3.4000	1.8333	1.8545	27.7143
5	19	3.4667	1.6000	2.1667	22.7765
6	20	3.3333	1.6333	2.0408	24.7000
Average		3.3667	1.6722	2.0180	24.1216
Standard Deviation		0.0919	0.0929	0.1161	2.0653
Average Deviation		0.0667	0.0741	0.0929	1.4498
Percent Deviation		1.98%	4.43%	4.60%	6.01%

Table 4.4: Summary of center point measurements and associated statistics.

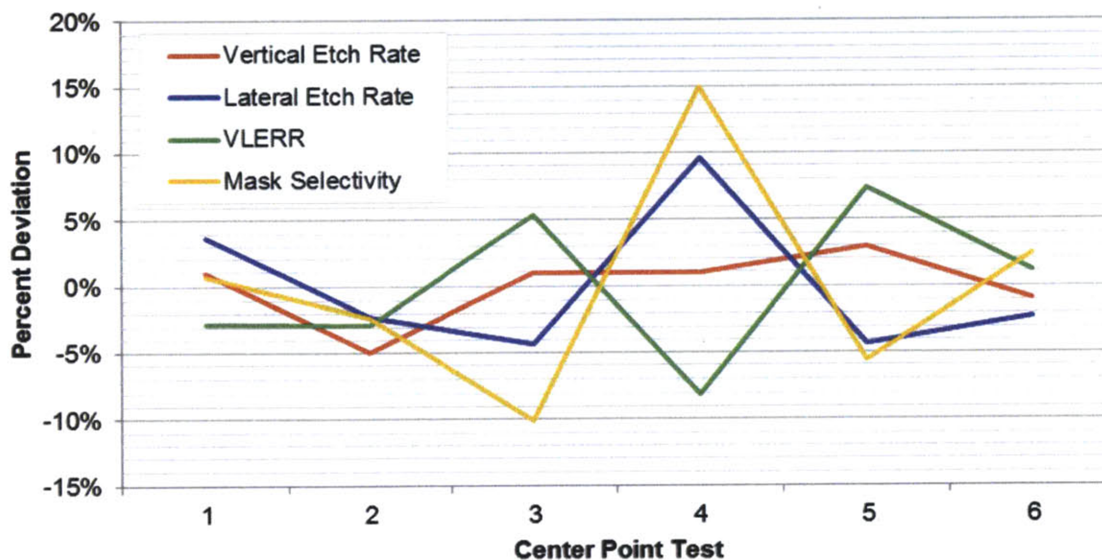

Figure 4.24: Comparison of center point measurements. The normalized measurements shown represent the percent deviation of each sample from the average value across all six center points. The raw values used for calculation are displayed in **Table 4.4**.

[24] The uniformities values are already presented as the average percent deviation from the mean (APDM, **Eqn. 4.2**) values, and so performing additional statistical measures (like calculating the percent variation of the percent etch rate variation) provides an unnecessary layer of abstraction.

As the data show, the variation across the center point tests was generally good (below 10% for everything except the mask selectivity of center point #4), particularly in the vertical etch rate parameter. The worst variation is seen in the mask selectivity, but some of the variance in this response may stem from the measurement method. The selectivity was calculated by measuring the average differences in photoresist heights between the etched and non-etched portions of a sample. The resist height, however, undulates across the length of a sample, with an average height of 10 μm and variations as large as 1 μm. This makes it difficult to estimate a precise value for the amount of photoresist erosion, which forms the denominator of the selectivity value. For deep etching (using SF_6+O_2 and the Bosch Process), materials other than photoresist are commonly used for their increased selectivity against silicon. This increase in the absolute selectivity makes variations less important. The final parameter used for evaluating the consistency of the center point tests was the etch rate uniformity. The values are plotted in **Figure 4.25**.

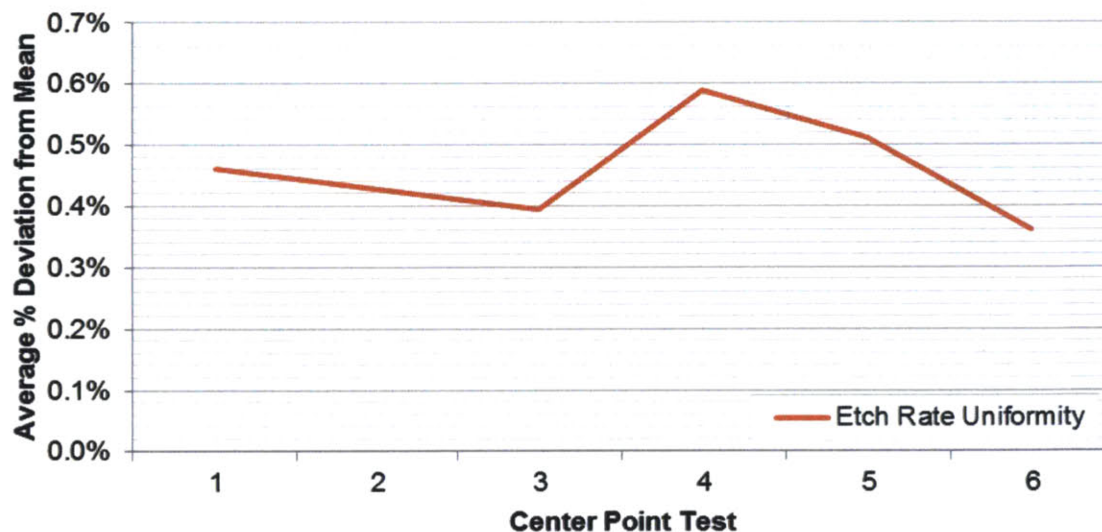

Figure 4.25: Comparison of the average percent deviation from the mean (APDM) etch rate (calculated on a per sample basis) for each of the six center point tests. This metric used to assess the spatial uniformity of the etch rate across a sample and was discussed in **Section 4.3.3**.

Just like the vertical etch rate statistics shown in **Table 4.4** and **Figure 4.24**, the data of **Figure 4.25** shows that the etches for the center point tests were all very consistent. The last comparison of the center point tests is the “eye test” of the profile and surface characteristics. The cross-sectional views for this test are provided below in **Figure 4.26**.

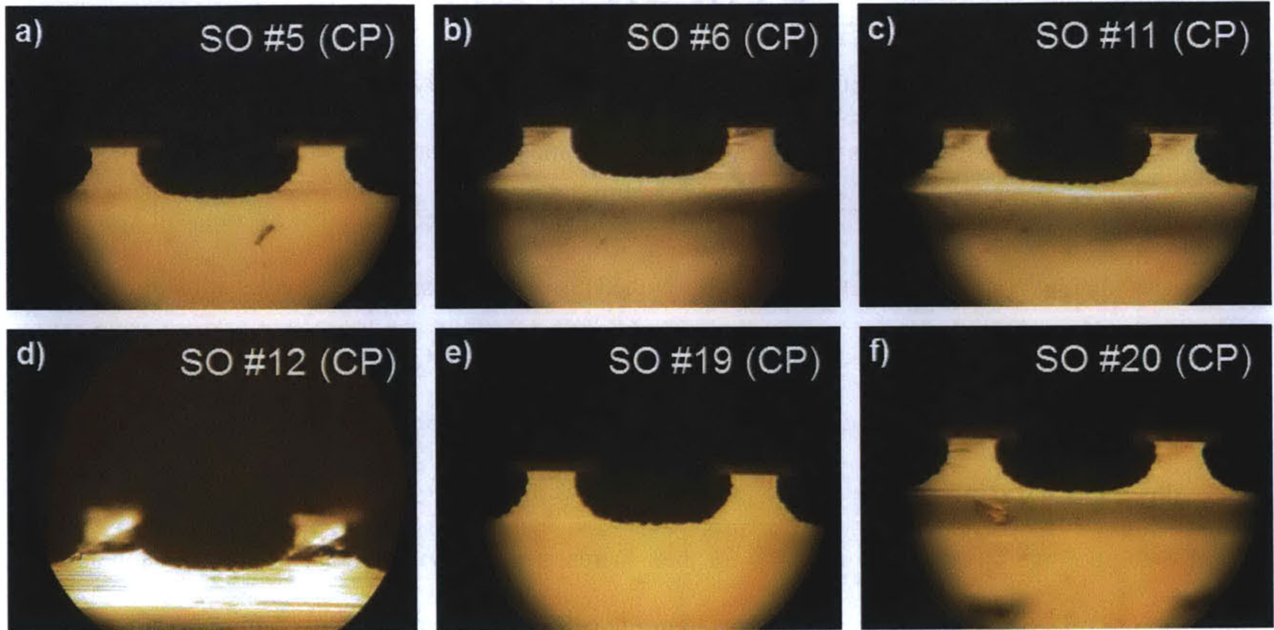

Figure 4.26: Cross-sectional views of the six center point tests. The profiles appear very similar. The missing photoresist on **b)** SO #6 and **d)** SO #12 are the result of problems during the cleaving process.

With the exception of the missing photoresist from two of the samples, the profiles of the center point tests look remarkably similar. Combined with the quantitative data, this shows that good repeatability is possible in the 1" Fab DRIE system. Further improvement is certainly still needed, and will be aggressively sought as the system evolves into its next iteration.

Chapter 5: Conclusions and Future Directions

In this thesis, significant progress has been made toward an inexpensive and compact deep reactive ion etching system for small substrates. The 1" Fab DRIE system is an essential piece of the larger 1" Fab platform that will help fill the current market gap in small-scale production and prototyping of novel electronic and electromechanical devices based on IC manufacturing methods.

Through the characterization tests discussed in **Chapter 4**, the performance of several aspects of the 1" Fab DRIE has been assessed and analyzed. These results are quite promising, and show that the 1" Fab DRIE system operates with largely the same physical and chemical mechanisms as established commercial systems for processing larger substrates. There is still, however, much important work to be done. Specific questions about the 1" Fab DRIE's operation under certain parameter groupings need to be answered, and the C_4F_8 deposition capabilities must be examined before testing and optimizing any Bosch Process DRIE recipes. Additionally, several opportunities for increased reliability and performance of the system were discovered while carrying out this thesis work, and these need to be integrated and characterized. Along with a summary of the work leading up to this chapter, the sections below will also discuss these future directions for the 1" Fab DRIE system.

5.1 Summary of Performance

Before performing any quantitative etching, the vacuum and plasma generation subsystems were tested to establish their capabilities and limits. The full vacuum system exhibited a leak tightness rating of between 0.9×10^{-5} and 1.5×10^{-4} atm·cm^3/sec after pumping down for 10-15 minutes. This is equivalent to a process gas flow of 0.005 to 0.009 sccm, or just 0.27% to 0.44% of the normal (center point) process gas flow used for etching. The Langmuir probe tests of the inductively coupled plasma generation system provided the baseline power requirements for initiating E- to H-mode transitions in several common process gas mixtures. The transition to the H- or inductively coupled mode is necessary to obtain the high

plasma densities required for faster etching. This transition was seen to occur for normal process gas flows including SF_6 around 200 W, which was then used as the coil power in later processing. Additional Langmuir probe sweeps showed that hysteresis allowed these H-mode discharges to be sustains at coil powers as low as 160 W.

After establishing the characteristics of the vacuum and plasma generation subsystems, the operation of the full system was investigated through the use of a design-of-experiments technique known as the response surface methodology (RSM). Using RSM techniques, a three factor, 20 test circumscribed central composite (CCC) design was carefully constructed and carried out. Measurements of the vertical etch depth, lateral etch depth, etch profile, etch spatial uniformity, and mask erosion were collected for each sample. This data was then used to determine relationships between the factors (SF_6 flow, O_2 flow, and base power) and the etch properties, as well provide insight on the performance of the 1" Fab DRIE system as a whole.

The vertical etch rates observed during the RSM test sequence ranged from 2-4.3 um/min and showed clear dependencies on the amounts the SF_6 and O_2 in the system. Etch rates universally increased with larger SF_6 flows, and while they generally increased with larger O_2 flows, the RSM model was able to predict an optimum percentage of O_2 near 30% for the maximum etch rate. Both the positive effect of additional SF_6 and the optimum O_2 percentage of ~30% fit readily with observations made in the literature. The trajectory of these findings also indicate that significantly larger etch rates are possible with increased process gas flows and a small increase in pumping capacity (resulting in a reduction in residence time). One of the most unexpected results of the RSM test sequence was the base power effect on etch rate. It was originally thought that increases in the base power would improve the etch rate and the anisotropy, but instead the data showed a slight indication of lower base powers producing the faster and more anisotropic etches. The exact mechanism causing this change is not known, but it is hypothesized that while the total power applied to base electrode was not large by normal plasma etching standards, the areal power density was quite large compared to normal standards (due to the reduced size

of the electrode). This large density may have led to increased substrate heating, which has been shown to decrease etch rates [9,39].

The spatial uniformity data gathered for the RSM test sequence showed that the etch rate across the samples was quite consistent, with 80% (sixteen samples) of the samples displaying average deviations of less than 1% from the mean etch rate. The remaining 20% (four samples) had silicon grass on the etch surface and average deviations between 3% and 4%. The onset of this surface-roughening and uniformity-dampening grass was shown to be related again to the percentage of O_2 in the process gas flow, with grass forming on all four samples etched with greater than 37% O_2. The high degree of spatial uniformity observed on the remaining 80%, which were processed using a variety of base powers and process gas flows, indicates both a high degree of uniformity in the distribution of etching species in the chamber and the lack of temperature gradients across the substrate (uniform cooling).

The etch profile was assessed by both qualitative and quantitative metrics. Qualitatively the etch profiles were classified into isotropic and anisotropic based on their sidewall profiles and quantitatively the samples were assessed based on their vertical to lateral etch rate ratio (VLERR). Again the most important parameter was found to be the percentage of O_2 in the gas flow. For O_2 percentages above 37% the profiles were always anisotropic (and exhibited silicon grass), while isotropic profiles were found on 88% (14/16) of samples with O_2 percentages below 28% (silicon grass was absent on all 16 samples below 28% O_2).

As a final look into the performance of the 1" Fab DRIE, the results of the six center point tests of the RSM sequence were compared. Each of the six samples showed a very consistent isotropic profile, with etch rates across each individual sample varying by less than 0.6%. This consistency generally extended to the quantitative measures as well with variations from the mean values below 5% for vertical etch rate, below 10% for lateral etch rate and VLERR, and below 15% for mask selectivity (although the mask selectivity variation may have been partially attributable to the measurement method).

In total, the data from RSM sequence provided a substantial amount of knowledge about the performance of the 1" Fab DRIE. The most important parameters in determining the properties of etch appear to be the quantity of SF_6 used and the relative percentage of oxygen in the total process gas flow. The effect of the base power was difficult to determine from the tests performed, but the reason for this may be a confounded effect with the substrate temperature.

5.2 Follow Up Tests

One of the primary reasons for running RSM test sequences is to establish a baseline for the performance of a particular system, and identify specific areas of interest for future tests. For the 1" Fab DRIE, the two areas of follow-up testing that are immediately apparent from the RSM test sequences are the low base power region and the region with gas flows containing between 27% and 37% O_2. Further tests in these areas will help determine if in fact lower base powers (or confounded effects with base power) do correspond to higher etch rates, and help confirm the ideal percentage of oxygen in a gas stream for the desired etch characteristics (e.g. large etch rates, anisotropy, spatial uniformity).

Outside of the parameters tested by the RSM sequence, tests involving varying coil powers and coil-chuck spacing, both of which are known to affect etch characteristics also need to be performed, as well as tests on samples with different feature sizes and feature densities, which are necessary to understand the effects of macroloading and microloading for the 1" Fab DRIE.

The ultimate application for this etching system is of course Bosch Process DRIE, and so in addition to tests of SF_6-based etching, tests assessing the system's C_4F_8 deposition capabilities must also be performed. Proof-of-concept tests have been performed for C_4F_8 deposition and gas-switching protocols like the Bosch Process, but rigorous and systematic testing will be needed to determine the ideal parameters and practical limits for the 1" Fab DRIE.

5.3 Future Improvements

The test results presented in **Chapter 4** and summarized in **Section 5.1** demonstrate that the 1" Fab DRIE is a functional etching system capable of uniformly etching silicon substrates with degrees of both profile and etch rate control. However, the characterization process also exposed several areas where the current capabilities of the system (in both control and monitoring) need improvement. In response to these observations, four changes to the system have been proposed. Each of these changes and their expected effect on the system's performance are outlined below.

5.3.1 Conductance Control Valve

In the current iteration of the 1" Fab DRIE, the system pressure is determined by the amount of process gas being flown through the system. The coupling of these two parameters is not ideal, and thus the first proposed change to the existing system is the addition of a conductance control valve. This type of valve fits in series with the vacuum line and has the ability to mechanically change its conductance. The differing conductance of the valve changes the effective pumping speed of the vacuum pump, which changes the upstream pressure in the chamber. This change will allow a constant pressure to be maintained in the system regardless of the amount of process gas being flown through the system (within the limits of the pumping system). The lack of pressure control in the current iteration of the system was most evident during the Langmuir probe measurements on SF_6 and SF_6+O_2 plasma densities. Higher densities were expected for the SF_6+O_2 gas flows because O_2 is known to facilitate the dissocation of SF_6 molecules [9,32], but the opposite was observed. However, the pressure in the system was not held constant for these tests, and so the lower densities may have been caused by the increased chamber pressure measured during the SF_6+O_2 tests (via Paschen's Law, as described in **Section 4.1.2**). The addition of a conductance control valve would allow these Langmuir probe tests, as well any other test sequences, to occur under constant pressure conditions.

5.3.2 Turbo Pump

The second proposed change also involves controlling the system pressure. The original decision to use a rotary vane pump to pull the vacuum in the system was made because of their resilience against large pressures and pressure fluctuations and their lower cost compared to turbo pumps. Large pressure influxes were primarily a point of concern in the early stages of development of the 1" Fab DRIE, but since that time the pressure stability of the current system has been greatly improved, making the hardiness of rotary vane pumps less important. In a stable vacuum environment, even a very small turbo pump (for instance a Varian Turbo-V 81 or a Pfeiffer HiPace 80) can provide significantly larger pumping speeds than the rotary vane pump currently in use (~70 L/s vs. 2-7 L/s) over the 1-100 mTorr range of pressures used during etching. For a given target pressure, this increased pumping speed would permit the use of significantly larger process gas flow rates, which would increase the maximum etch rate and also allow for faster gas switching times (due to the decreased gas residence times) when running Bosch Process DRIE tests. A rendering of the current 1" Fab DRIE with a butterfly-style conductance control valve and a 70 L/s turbo pump is shown below in **Figure 5.1**.

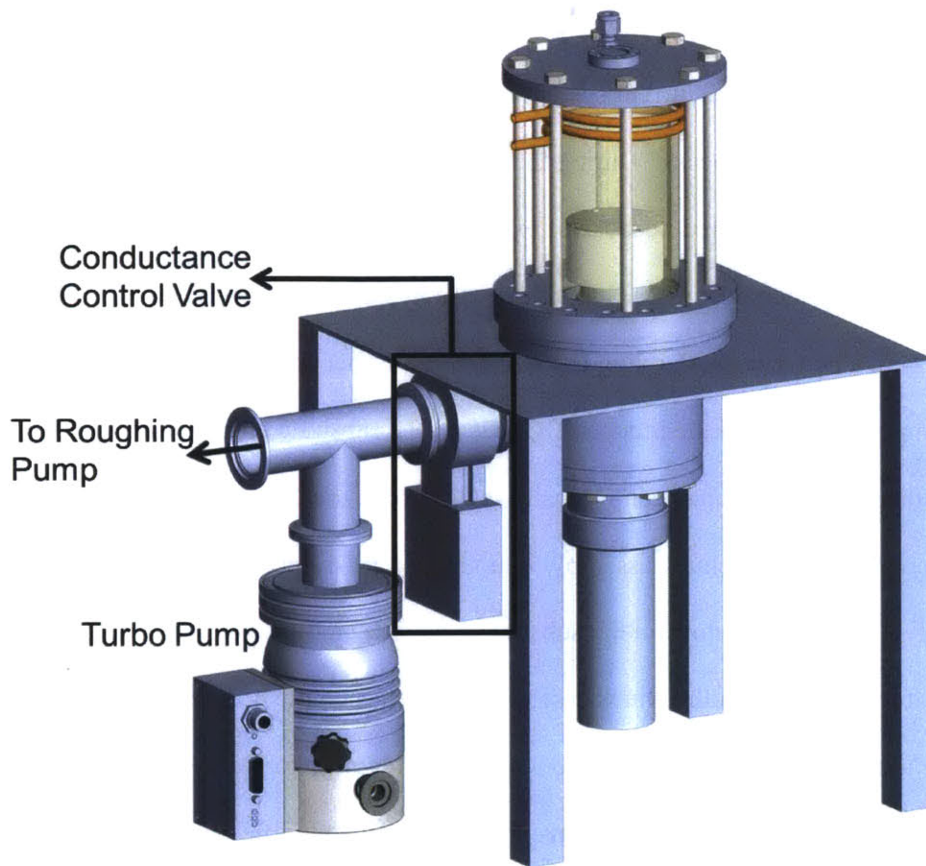

Figure 5.1: A rendering of a 1" Fab DRIE with a turbo pump and conductance control valve.

5.3.3 Helium Backside Wafer Cooling

The third improvement that can be made to the system is the incorporation of a helium backside cooling system to the chuck. The current system for substrate cooling uses a low-outgassing thermal vacuum grease as a heat transfer medium between the substrate (which is being heated by ion bombardment and the exothermic $Si + 4F \rightarrow SiF_4$ chemical reaction) and the water-cooled chuck. The thermal grease system provides significantly better thermal conduct to the water-cooled chuck than can be achieved by simply placing a sample on the chuck. However, the use of a hydrocarbon-based grease in a vacuum chamber and having that grease make intimate contact with the back side of devices being etched are non-ideal scenarios. The use of helium instead of thermal grease eliminates both of these problems, and may further improve the efficiency of the cooling system by providing a more uniform contact area for heat transfer.

5.3.4 Process Monitoring - Substrate Temperature and Bias Voltage

The final proposed change to the current system is an expansion of the range of parameters that can be monitored during an etching process. During the RSM tests, the counterintuitive effect of the base power was hypothesized to have occurred because of excess substrate heating, but the current system has no way of determining if the applied power leads to an increase in substrate temperature. To test this hypothesis and in general gain a better understanding of the mechanisms occurring around the substrate, the ability to monitor the temperature as well the induced DC bias on the substrate electrode are needed. The apparatus for measuring these two parameters can be easily integrated to the existing design. The DC bias can be monitored externally from the chuck assembly by making a RF-filtered measurement of the voltage between the RF blocking capacitor (on the substrate electrode side) and the chamber ground. The measurement of temperature on the chuck assembly can be accomplished by adding a hole and O-ring sealing groove to the PEEK isolation block to act as a feedthrough for a RF-shielded thermocouple or resistance temperature detector (RTD). **Figure 5.2** displays the modified PEEK piece.

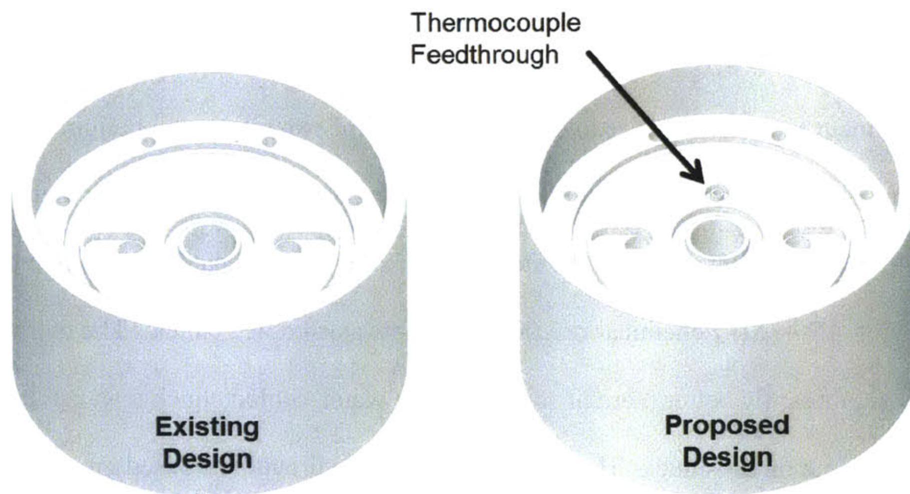

Figure 5.2: Rendering of the necessary modification to the chuck isolation and alignment block to incorporate the thermocouple. The piece shown on the left is currently used in the system and does not have the feedthrough port.

Each of the four changes outlined above can be quickly integrated into the current iteration of the 1" Fab DRIE and together will have a significant and immediate impact on the performance, repeatability and monitoring abilities of the system. The increased capabilities of the system will also aid in the remaining

characterization tests of the SF_6 system, the forthcoming tests on C_4F_8 deposition, and ultimately the tests of Bosch Process DRIE. These upgrades are, of course, not without cost. The additional cost is estimated at ~\$3,300, bringing the total system cost to ~\$35,000[1], with the costs of the chamber assembly and peripherals now at ~\$6300 and ~\$28,700[25], respectively. This represents an increase of 10.5% in cost from the current iteration, but it is strongly believed that the performance gains from these additions more than justify their additional cost. The bill of materials including these improvements is also included in **Appendix A**.

5.4 Looking Forward

On the road to a fully functional 1" Fab platform, the results presented in this thesis on the design of a small scale DRIE tool and the characterization of its etching performance represents a significant milestone. In addition to its own usefulness as a tool for creating high aspect ratio features in silicon, the 1" Fab DRIE design constructed here will also serve as a building block for future 1" Fab etching and deposition tools. There is still a great deal of work to be done, but the progress made over the course of this thesis work puts the 1" Fab's vision of a disruptive shift in semiconductor manufacturing several steps closer to reality.

[25] The peripheral cost now stands at ~82% of the total system costs, buoyed primarily by the RF generators and the addition of the turbo pump. The turbo pump requires a backing pump, which can be the rotary vane pump already used in this system, or a smaller, inexpensive diaphragm pump. The diaphragm pump is a better choice for a stand-alone system as it keeps costs low, but for an integrated platform like the 1" Fab, a large rotary vane pump can be used as the backing system for many turbo pumps, offsetting its initially larger cost. Both cost options are included in **Appendix B**.

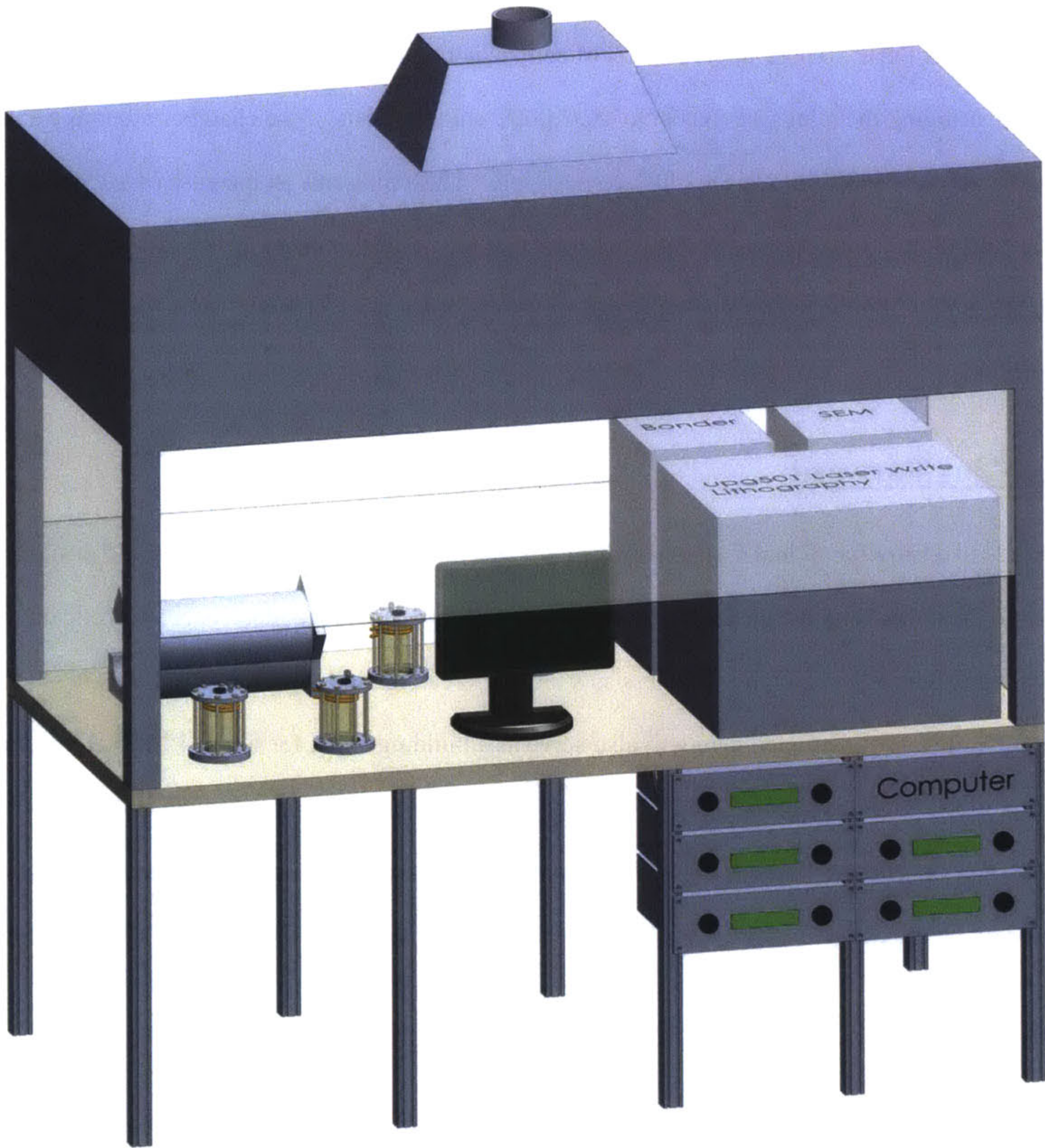

"The future of semiconductor fabrication"

References

1. Yole (2014) Status of MEMS Industry 2014. Available:http://www.i-micronews.com/upload/Rapports/Yole_Status_MEMS_Industry_July_2014_Report_Sample.pdf.

2. Bryzek J (2013) Emergence of Trillion Sensor Opportunity. Available:http://www.semiconwest.org/sites/semiconwest.org/files/docs/SW2013_Janusz Bryzek_Fairchild Semiconductor.pdf.

3. Heck S, Kaza S, Pinner D (2011) Creating value in the semiconductor industry.

4. Christensen C (2013) The innovator's dilemma: when new technologies cause great firms to fail. Harvard Business Review Press. p.

5. Ecole Polytechnique Federale De Lausanne (n.d.) Manual for AMS 200 SE. Available:https://cmi.epfl.ch/etch/AMS200.php.

6. Donnelly VM, Kornblit A (2013) Plasma etching: Yesterday, today, and tomorrow. J Vac Sci Technol A Vacuum, Surfaces, Film 31: 050825. Available:http://scitation.aip.org/content/avs/journal/jvsta/31/5/10.1116/1.4819316. Accessed 20 July 2014.

7. Park HM, Garvin C, Grimard DS, Grizzle JW (1999) Control of Ion Energy in Capacitively Coupled Reactive Ion Etcher. J Electrochem Soc. Available:http://web.eecs.umich.edu/~grizzle/papers/JECS99.pdf.

8. Collins KS, Rice M, Trow J, Buchberger D, Roderick CA (2004) Inductively coupled RF plasma reactor and plasma chamber enclosure structure therefor.

9. Jansen H, Gardeniers H, Boer M de, Elwenspoek M, Fluitman J (1996) A survey on the reactive ion etching of silicon in microtechnology. J Micromechanics Microengineering 6: 14–28. Available:http://stacks.iop.org/0960-1317/6/i=1/a=002. Accessed 21 July 2014.

10. Tu Y-Y, Chuang T, Winters H (1981) Chemical sputtering of fluorinated silicon. Phys Rev B 23: 823–835. Available:http://link.aps.org/doi/10.1103/PhysRevB.23.823. Accessed 6 August 2014.

11. d'Agostino R (1981) Plasma etching of Si and SiO2 in SF6–O2 mixtures. J Appl Phys 52: 162. Available:http://scitation.aip.org/content/aip/journal/jap/52/1/10.1063/1.328468. Accessed 7 August 2014.

12. Lim, Y-D., Lee, S-H., Yoo, W. J., Jung, O-J., Kim, S-C., Lee H-C (2009) Roles of F and O Radicals and Positive Ions in a SF6/O2 Plasma in Forming Deep Via Structures. J Korean Phys Soc 54: 1774.

13. Jansen H, Boer M de, Legtenberg R, Elwenspoek M (1995) The black silicon method: a universal method for determining the parameter setting of a fluorine-based reactive ion etcher in deep

silicon trench etching with profile control. J Micromechanics Microengineering 5: 115–120. Available:http://stacks.iop.org/0960-1317/5/i=2/a=015. Accessed 19 October 2012.

14. Syau T (1991) Reactive Ion Etching of Silicon Trenches Using SF6/O2 Gas Mixtures. J Electrochem Soc 138: 3076. Available:http://jes.ecsdl.org/content/138/10/3076.abstract. Accessed 18 April 2014.

15. Legtenberg R (1995) Anisotropic Reactive Ion Etching of Silicon Using SF6/O2/CHF3 Gas Mixtures. J Electrochem Soc 142: 2020. Available:http://jes.ecsdl.org/content/142/6/2020.abstract. Accessed 11 April 2014.

16. Laermer F, Schilp A (1996) Method of anisotropically etching silicon. Available:http://www.google.com/patents/US5501893.

17. PlasmaTherm (2012) Current Trends with DRIE/DSE Processing for MEMS Devices and Structures (Whitepaper). Available:http://www.plasmatherm.com/pdfs/Current-Trends-with-DRIE-DSE.pdf.

18. SPTS (2013) 1000 modules: A Milestone in SPTS DRIE History. Available:http://www.spts.com/banners/1000th-drie-module-sold.

19. Nikon (2014) i-line Stepper NSR-2205i14E2. Available:http://nikon.com/products/precision/lineup/nsr/iline/nsr-2205i14e2/pdf/NSR-2205i14E2_e.pdf.

20. Silicon-Edge Ltd. (2014) Die-per-Wafer Estimator. Available:http://www.silicon-edge.co.uk/j/index.php?option=com_content&view=article&id=68.

21. Theil JA (1995) Gas distribution through injection manifolds in vacuum systems. J Vac Sci Technol A Vacuum, Surfaces, Film 13: 442. Available:http://link.aip.org/link/?JVTAD6/13/442/1. Accessed 26 August 2013.

22. Lieberman MA, Lichtenberg AJ (1994) Principles of Plasma Discharges and Materials Processing. John Wiley and Sons. p.

23. Todorow V (2009) Impedance Matching and Matching Networks. Available:http://www.engr.sjsu.edu/rkwok/Engr297/Val_Impedance Matching and Matching Networks.pdf.

24. Advanced Energy (2012) Advanced Energy Introduces Fastest RF Matching Network. Available:http://www.mksinst.com/docs/ur/DynamicFrequencyTuning.aspx.

25. MKS Instruments (2014) Dynamic Frequency Tuning (DFT) for RF Plasma Generators. Available:http://ir.advanced-energy.com/phoenix.zhtml?c=105985&p=irol-newsArticle&ID=1713138&highlight=.

26. Comdel Inc. (2014) Frequency Agile Tuning. Available:http://www.comdel.com/optional-frequency-agile-tuning.

27. Ayon AA, Braff R, Lin CC, Sawin HH, Schmidt MA (1999) Characterization of a Time Multiplexed Inductively Coupled Plasma Etcher. J Electrochem Soc 146: 339. Available:http://jes.ecsdl.org/content/146/1/339.abstract. Accessed 18 November 2013.

28. Lee C, Graves DB, Lieberman MA (1996) Role of etch products in polysilicon etching in a high-density chlorine discharge. Plasma Chem Plasma Process 16: 99–120. Available:http://link.springer.com/10.1007/BF01465219. Accessed 13 August 2014.

29. Alicat Scientific (2014) Alicat MC Series Mass Flow Controllers. Available:http://www.alicat.com/documents/sales_sheets/MC-Series-Sales-Sheet.pdf.

30. Scitek (2014) Vacuum Screws. Available:http://www.scitek.com.au/wp-content/uploads/2012/11/vacuum_screws1.jpg.

31. Cunge G, Crowley B, Vender D, Turner MM (1999) Characterization of the E to H transition in a pulsed inductively coupled plasma discharge with internal coil geometry: bi-stability and hysteresis. Plasma Sources Sci Technol 8: 576–586. Available:http://iopscience.iop.org/0963-0252/8/4/309/pdf/ps9409.pdf. Accessed 21 August 2014.

32. Morshed MM, Daniels SM (2012) Electron Density and Optical Emission Measurements of SF 6 /O 2 Plasmas for Silicon Etch Processes. Plasma Sci Technol 14: 316–320. Available:http://iopscience.iop.org/1009-0630/14/4/09.

33. Okumura T (2010) Inductively Coupled Plasma Sources and Applications. Phys Res Int 2010. Available:http://dx.doi.org/10.1155/2010/164249.

34. Box GEP, Wilson KB (1951) On the Experimental Attainment of Optimum Conditions. J R Stat Soc Ser B 13: 1–45 CR – Copyright © 1951 Royal Statistical. Available:http://www.jstor.org/stable/2983966.

35. Lenth RV (2012) Response-Surface Methods in R Using RSM. Available:http://cran.r-project.org/web/packages/rsm/vignettes/rsm.pdf.

36. NIST-SEMATECH (2013) Engineering Statistics Handbook: Chapter 5. Available:http://www.itl.nist.gov/div898/handbook/.

37. Montgomery DC (2013) Design and Analysis of Experiments. 8th ed. New York: John Wiley & Sons. p.

38. Zhang H (Alice), Guo Y, Wang Y, Sun G (2008) Parameters Extraction for DRIE Model. Conference on Nano/Micro Engineered and Molecular Systems. Sanya, China: IEEE. pp. 544–547. Available:http://ieeexplore.ieee.org/lpdocs/epic03/wrapper.htm?arnumber=4484391. Accessed 20 August 2014.

39. Hooda MK, Wadhwa M, Verma S, Nayak MM, George PJ, et al. (2010) A systematic study of DRIE process for high aspect ratio microstructuring. Vacuum 84: 1142–1148. Available:http://www.sciencedirect.com/science/article/pii/S0042207X1000076X. Accessed 20 August 2014.

40. Drotar J, Zhao Y-P, Lu T-M, Wang G-C (2000) Mechanisms for plasma and reactive ion etch-front roughening. Phys Rev B 61: 3012–3021. Available:http://link.aps.org/doi/10.1103/PhysRevB.61.3012. Accessed 21 August 2014.

41. Gogolides, E., Boukouras, C., Kokkoris, G., Brani, O., Tserepi, A., Constantoudis V (2004) Si etching in high-density SF6 plasmas for microfabrication: surface roughness formation. Microelectron Eng 73-74: 312–318. Available:http://www.sciencedirect.com/science/article/pii/S0167931704001170. Accessed 28 August 2014.

42. Martin M, Cunge G (2008) Surface roughness generated by plasma etching processes of silicon. J Vac Sci Technol B Microelectron Nanom Struct 26: 1281. Available:http://scitation.aip.org/content/avs/journal/jvstb/26/4/10.1116/1.2932091. Accessed 21 August 2014.

43. ITRS (2013) 2013 International Technology Roadmap for Semiconductors. Available:http://public.itrs.net/Links/2013ITRS/Summary2013.htm.

Appendix A: 1" Fab DRIE Bill of Materials

Part	Manufacturer	URL	Price	Customization?	Customization description	Labor Hours	Added Cost	Total Cost	Notes	Customization Charge
Gas manifolds	McMaster	http://www.mcmaster.com/	$20.00	yes	from stock	2	$160.00	$180.00		$80.00
Clippard valves (x5)	Clippard	http://www.clippard.com/part/E	$130.00	no			$0.00	$130.00		per hour
Three-way bleed valve (1/4" Swagelok)	Swagelok	http://www.swagelok.com/sear	$87.00	no			$0.00	$87.00		
Sapphire CF 1.33" Viewport	MDC	http://www.mdcvacuum.com/Di	$200.00	no			$0.00	$200.00		
1/4" Ultra-Torr	Swagelok	http://www.swagelok.com/	$25.00	no			$0.00	$25.00		
CF 6" Top Flange	Kurt Lesker	http://www.lesker.com/	$60.00	yes	gas inlet, viewport, cyl. recess	4	$320.00	$380.00		
Gas showerhead	McMaster	http://www.mcmaster.com/	$20.00	yes	from stock	4	$320.00	$340.00		
Alumina Cylinder	Sentro Tech	http://www.sentrotech.com/	$175.00	no			$0.00	$175.00		
Copper ICP coil	McMaster	http://www.mcmaster.com/	$10.00	yes	bend to coil	3	$240.00	$250.00		
RF+water coil connection plate	McMaster	http://www.mcmaster.com/	$10.00	yes	from stock	1.5	$120.00	$130.00	Plate, spacers, copper RF rod connector	
Type HN bulkhead RF connector	Pasternack	http://www.pasternack.com/hn-	$45.00	no			$0.00	$45.00		
1/4" Swagelok bulkhead fitting	Swagelok	http://www.swagelok.com/sear	$17.00	no			$0.00	$17.00		
1/4" push-to-connect bulkhead fitting	McMaster	http://www.mcmaster.com/#57	$6.00	no			$0.00	$6.00		
Copper+plastic RF shroud	McMaster	http://www.mcmaster.com/	$30.00	yes	cut to size	0.5	$40.00	$70.00		
CF 6" quick release flange	McMaster	http://www.mcmaster.com/	$40.00	yes	from stock	6	$480.00	$520.00		
CF 6"-4.5" zero length reducer	Kurt Lesker	http://www.lesker.com/	$119.00	no			$0.00	$119.00		
Alumina sample clamp	McMaster	http://www.mcmaster.com/	$12.00	yes	waterjet	1	$80.00	$92.00		
PEEK chuck insulator	McMaster	http://www.mcmaster.com/	$100.00	yes	from stock	4	$320.00	$420.00		
Aluminum water cooling chuck	McMaster	http://www.mcmaster.com/	$10.00	yes	from stock	4	$320.00	$330.00		
Chuck/pyrex spacers	McMaster	http://www.mcmaster.com/	$20.00	yes		1	$80.00	$100.00		
Aluminum hollow chuck rod	McMaster	http://www.mcmaster.com/	$53.00	yes		3	$240.00	$293.00		
Chuck suckback stop / hose clamp	McMaster	http://www.mcmaster.com/	$10.00	yes		0.5	$40.00	$50.00		
Chuck water fittings	McMaster	http://www.mcmaster.com/	$6.00	no			$0.00	$6.00		
Chuck RF fitting (BNC)	Pasternack	http://www.pasternack.com/bnc	$8.00	no			$0.00	$8.00		
Base plate / stand	McMaster	http://www.mcmaster.com/	$100.00	yes	from stock	2	$160.00	$260.00		
Lower cylinder	McMaster	http://www.mcmaster.com/	$40.00	yes	from stock	2	$160.00	$200.00		
CF 4.5" UT flange	Kurt Lesker	http://www.lesker.com/	$41.00	yes	weld prep	1	$80.00	$121.00		
2" Ultra-torr fitting	Kurt Lesker	http://www.lesker.com/	$135.00	yes	weld to flange	0.5	$40.00	$175.00		
1.5" NPT to KF40 flange	IdealVac	http://www.idealvac.com/	$126.00	no			$0.00	$126.00		
KF40 - 1/8" NPT - KF40 Tee	IdealVac	http://www.idealvac.com/	$62.00	no			$0.00	$62.00		
KF40 vacuum hose (48")	Kurt Lesker	http://www.lesker.com/	$255.00	no			$0.00	$255.00		
Miscellaneous hardware	McMaster	http://www.mcmaster.com/	$200.00	no			$0.00	$200.00	M8, 5/16-24, 10-32, 4-40, 2-56	
Miscellaneous tubing/fittings	McMaster	http://www.mcmaster.com/	$100.00	no			$0.00	$100.00		
Type HN cable (36")	Pasternack	http://www.pasternack.com/hn-	$119.00	no			$0.00	$119.00		
Type N cable (2x18")	L-com	http://www.l-com.com/productfi	$40.00	no			$0.00	$40.00		
BNC Cables (1x18", 1x36")	L-com	http://www.l-com.com/coaxial-r	$17.00	no			$0.00	$17.00		
RF Capacitor	RF Parts Co.	http://www.rfparts.com/capacito	$28.00	no			$0.00	$28.00		
RF Capacitor housing	McMaster	http://www.mcmaster.com/	$10.00	yes	from stock	1	$80.00	$90.00		
RF fittings (BNC)	Pasternack	http://www.pasternack.com/bnc	$16.00	no			$0.00	$16.00		
			$2,502.00 Total Raw Materials/Parts Cost				$3,280.00 Total Customi	$5,782.00 Total Chamber Cost		$5,782.00 Total Chamber Cost
O2 MFC (MC-100SCCM-D)	Alicat	http://www.alicat.com/products	$1,260.00	no			$0.00	$1,260.00		
SF6 MFC (MC-100SCCM-D)	Alicat	http://www.alicat.com/products	$1,260.00	no			$0.00	$1,260.00		
C4F8 MFC (MCS-100SCCM-D)	Alicat	http://www.alicat.com/products	$1,710.00	no			$0.00	$1,710.00		
600W Coil RF Generator (CX600-AS)	Comdel	http://comdel.com/cx-series-hi	$5,600.00	no			$0.00	$5,600.00		
600W Chuck RF Generator (OEM-6B)	ENI		$3,900.00	no			$0.00	$3,900.00		
600W Automatic Matching Network	T&C Power Con	http://www.tcpowerconversion.c	$2,800.00					$2,800.00		
1kW Manual Matching Network	Heathkit		$250.00					$250.00		
Pneumatic valve	Lesker	http://www.lesker.com/	$450.00	no			$0.00	$450.00		
Thermocouple gauges and readouts (2x)	Lesker	http://www.lesker.com/	$600.00	no			$0.00	$600.00		$22,270.00 Total Peripheral Cost
Control circuitry	various, mostly Newark		$200.00	yes	assembly	3	$240.00	$440.00		
Rotary vane pump (Leybold D30A)	IVS	http://www.ivsonline.com/	$2,000.00	no			$0.00	$2,000.00		**$28,052.00 Total Everything Cost**
PFPE oil	IVS	http://www.ivsonline.com/	$2,000.00	no			$0.00	$2,000.00		
								$22,270.00 Total Peripheral Cost		

This sheet contains the prices for the system as tested in the thesis

Part	Manufacturer	URL	Price	Customization?	Customization description	Labor Hours	Added Cost	Total Cost	Notes	Customization Charge	
Gas manifolds	McMaster	http://www.mcmaster.com/	$20.00	yes	from stock	2	$160.00	$180.00		$80.00	
Clippard valves (x5)	Clippard	http://www.clippard.com/part/E	$130.00	no			$0.00	$130.00		per hour	
Three-way bleed valve (1/4" Swagelok)	Swagelok	http://www.swagelok.com/sear	$87.00	no			$0.00	$87.00			
Sapphire CF 1.33" Viewport	MDC	http://www.mdcvacuum.com/Di	$200.00	no			$0.00	$200.00			
1/4" Ultra-Torr	Swagelok	http://www.swagelok.com/	$25.00	no			$0.00	$25.00			
CF 6" Top Flange	Kurt Lesker	http://www.lesker.com/	$60.00	yes	gas inlet, viewport, cyl. recess	4	$320.00	$380.00			
Gas showerhead	McMaster	http://www.mcmaster.com/	$20.00	yes	from stock	4	$320.00	$340.00			
Alumina Cylinder	Sentro Tech	http://www.sentrotech.com/	$175.00	no			$0.00	$175.00			
Copper ICP coil	McMaster	http://www.mcmaster.com/	$10.00	yes	bend to coil	3	$240.00	$250.00			
RF+water coil connection plate	McMaster	http://www.mcmaster.com/	$10.00	yes	from stock	1.5	$120.00	$130.00	Plate, spacers, copper RF rod connector		
Type HN bulkhead RF connector	Pasternack	http://www.pasternack.com/hn-	$45.00	no			$0.00	$45.00			
1/4" Swagelok bulkhead fitting	Swagelok	http://www.swagelok.com/sear	$17.00	no			$0.00	$17.00			
1/4" push-to-connect bulkhead fitting	McMaster	http://www.mcmaster.com/#57	$6.00	no			$0.00	$6.00			
Copper+plastic RF shroud	McMaster	http://www.mcmaster.com/	$30.00	yes	cut to size	0.5	$40.00	$70.00			
CF 6" quick release flange	McMaster	http://www.mcmaster.com/	$40.00	yes	from stock	6	$480.00	$520.00			
CF 6"-4.5" zero length reducer	Kurt Lesker	http://www.lesker.com/	$119.00	no			$0.00	$119.00			
Alumina sample clamp	McMaster	http://www.mcmaster.com/	$12.00	yes	waterjet	1	$80.00	$92.00			
PEEK chuck insulator	McMaster	http://www.mcmaster.com/	$100.00	yes	from stock	4	$320.00	$420.00			
Aluminum water cooling chuck	McMaster	http://www.mcmaster.com/	$10.00	yes	from stock	4	$320.00	$330.00			
Chuck/pyrex spacers	McMaster	http://www.mcmaster.com/	$20.00	yes		1	$80.00	$100.00			
Aluminum hollow chuck rod	McMaster	http://www.mcmaster.com/	$53.00	yes		3	$240.00	$293.00			
Chuck suckback stop / hose clamp	McMaster	http://www.mcmaster.com/	$10.00	yes		0.5	$40.00	$50.00			
Chuck water fittings	McMaster	http://www.mcmaster.com/	$6.00	no			$0.00	$6.00			
Chuck RF fitting (BNC)	Pasternack	http://www.pasternack.com/bnc	$8.00	no			$0.00	$8.00			
Base plate / stand	McMaster	http://www.mcmaster.com/	$100.00	yes	from stock	2	$160.00	$260.00			
Lower cylinder	McMaster	http://www.mcmaster.com/	$40.00	yes	from stock	2	$160.00	$200.00			
CF 4.5" UT flange	Kurt Lesker	http://www.lesker.com/	$41.00	yes	weld prep	1	$80.00	$121.00			
2" Ultra-torr fitting	Kurt Lesker	http://www.lesker.com/	$135.00	yes	weld to flange	0.5	$40.00	$175.00			
1.5" NPT to KF40 flange	IdealVac	http://www.idealvac.com/	$126.00	no			$0.00	$126.00			
KF40 - 1/8" NPT - KF40 Tee	IdealVac	http://www.idealvac.com/	$62.00	no			$0.00	$62.00			
KF40 vacuum hose (48")	Kurt Lesker	http://www.lesker.com/	$255.00	no			$0.00	$255.00			
Miscellaneous hardware	McMaster	http://www.mcmaster.com/	$200.00	no			$0.00	$200.00	M8, 5/16-24, 10-32, 4-40, 2-56		
Miscellaneous tubing/fittings	McMaster	http://www.mcmaster.com/	$100.00	no			$0.00	$100.00			
Type HN cable (36")	Pasternack	http://www.pasternack.com/hn-	$119.00	no			$0.00	$119.00			
Type N cable (2x18")	L-com	http://www.l-com.com/productfi	$40.00	no			$0.00	$40.00			
BNC Cables (1x18", 1x36")	L-com	http://www.l-com.com/coaxial-r	$17.00	no			$0.00	$17.00			
RF Capacitor	RF Parts Co.	http://www.rfparts.com/capacito	$28.00	no			$0.00	$28.00			
RF Capacitor housing	McMaster	http://www.mcmaster.com/	$10.00	yes	from stock	1	$80.00	$90.00			
RF fittings (BNC)	Pasternack	http://www.pasternack.com/bnc	$16.00	no			$0.00	$16.00			
			$2,502.00				$3,280.00	$5,782.00			$5,782.00
			Total Raw Materials/Parts Cost				Total Customi	Total Chamber Cost			Total Chamber Cost
N2 MFC (MC-100SCCM-D)	Alicat	http://www.alicat.com/products	$1,260.00	no			$0.00	$1,260.00	*not in the original system, but necessary in a commercial system*		
O2 MFC (MC-100SCCM-D)	Alicat	http://www.alicat.com/products	$1,260.00	no			$0.00	$1,260.00			
SF6 MFC (MC-100SCCM-D)	Alicat	http://www.alicat.com/products	$1,260.00	no			$0.00	$1,260.00			
C4F8 MFC (MCS-100SCCM-D)	Alicat	http://www.alicat.com/products	$1,710.00	no			$0.00	$1,710.00			
600W Coil RF Generator (CX600-AS)	Comdel	http://comdel.com/cx-series-hi	$5,600.00	no			$0.00	$5,600.00			
300W Chuck RF Generator (R301)	Seren IPS	http://www.serenips.com/R301	$3,600.00	no			$0.00	$3,600.00			
600W Automatic Matching Network	T&C Power Con	http://www.tcpowerconversion.c	$2,800.00					$2,800.00			
600W Automatic Matching Network	T&C Power Con	http://www.tcpowerconversion.c	$2,800.00					$2,800.00			
Pneumatic valve	Lesker	http://www.lesker.com/	$450.00	no			$0.00	$450.00			
Thermocouple gauges and readouts (2x)	Lesker	http://www.lesker.com/	$600.00	no			$0.00	$600.00			$25,780.00
Control circuitry	various, mostly Newark		$200.00	yes	assembly	3	$240.00	$440.00			Total Peripheral Cost
Rotary vane pump (Leybold D30A)	IVS	http://www.ivsonline.com/	$2,000.00	no			$0.00	$2,000.00			**$31,562.00**
PFPE oil	IVS	http://www.ivsonline.com/	$2,000.00	no			$0.00	$2,000.00			**Total Everything Cost**
								$25,780.00			
								Total Peripheral Cost			

This sheet contains the price to build and sell an equivalent system to the one tested in the thesis

Only new and readily available components are used in this calculation

Part	Manufacturer	URL	Price	Customization?	Customization description	Labor Hours	Added Cost	Total Cost	Notes	Customization Charge
Gas manifolds	McMaster	http://www.mcmaster.com/	$20.00	yes	from stock	2	$160.00	$180.00		$80.00
Clippard valves (x5)	Clippard	http://www.clippard.com/part/E	$130.00	no			$0.00	$130.00		per hour
Three-way bleed valve (1/4" Swagelok)	Swagelok	http://www.swagelok.com/sear	$87.00	no			$0.00	$87.00		
Sapphire CF 1.33" Viewport	MDC	http://www.mdcvacuum.com/Di	$200.00	no			$0.00	$200.00		
1/4" Ultra-Torr	Swagelok	http://www.swagelok.com/	$25.00	no			$0.00	$25.00		
CF 6" Top Flange	Kurt Lesker	http://www.lesker.com/	$60.00	yes	gas inlet, viewport, cyl. recess	4	$320.00	$380.00		
Gas showerhead	McMaster	http://www.mcmaster.com/	$20.00	yes	from stock	4	$320.00	$340.00		
Alumina Cylinder	Sentro Tech	http://www.sentrotech.com/	$175.00	no			$0.00	$175.00		
Copper ICP coil	McMaster	http://www.mcmaster.com/	$10.00	yes	bend to coil	3	$240.00	$250.00		
RF+water coil connection plate	McMaster	http://www.mcmaster.com/	$10.00	yes	from stock	1.5	$120.00	$130.00	Plate, spacers, copper RF rod connector	
Type HN bulkhead RF connector	Pasternack	http://www.pasternack.com/hn-	$45.00	no			$0.00	$45.00		
1/4" Swagelok bulkhead fitting	Swagelok	http://www.swagelok.com/sear	$17.00	no			$0.00	$17.00		
1/4" push-to-connect bulkhead fitting	McMaster	http://www.mcmaster.com/#57	$6.00	no			$0.00	$6.00		
Copper+plastic RF shroud	McMaster	http://www.mcmaster.com/	$30.00	yes	cut to size	0.5	$40.00	$70.00		
CF 6" quick release flange	McMaster	http://www.mcmaster.com/	$40.00	yes	from stock	6	$480.00	$520.00		
CF 6"-4.5" zero length reducer	Kurt Lesker	http://www.lesker.com/	$119.00	no			$0.00	$119.00		
Alumina sample clamp	McMaster	http://www.mcmaster.com/	$12.00	yes	waterjet	1	$80.00	$92.00		
PEEK chuck insulator	McMaster	http://www.mcmaster.com/	$100.00	yes	from stock	5	$400.00	$500.00		
Aluminum water cooling chuck	McMaster	http://www.mcmaster.com/	$10.00	yes	from stock	5	$400.00	$410.00		
Chuck/pyrex spacers	McMaster	http://www.mcmaster.com/	$20.00	yes		1	$80.00	$100.00		
Aluminum hollow chuck rod	McMaster	http://www.mcmaster.com/	$53.00	yes		3	$240.00	$293.00		
Chuck suckback stop / hose clamp	McMaster	http://www.mcmaster.com/	$10.00	yes		0.5	$40.00	$50.00		
Chuck water fittings	McMaster	http://www.mcmaster.com/	$6.00	no			$0.00	$6.00		
Chuck RF fitting (BNC)	Pasternack	http://www.pasternack.com/bnc	$8.00	no			$0.00	$8.00		
Base plate / stand	McMaster	http://www.mcmaster.com/	$100.00	yes	from stock	2	$160.00	$260.00		
Lower cylinder	McMaster	http://www.mcmaster.com/	$40.00	yes	from stock	2	$160.00	$200.00		
CF 4.5" UT flange	Kurt Lesker	http://www.lesker.com/	$41.00	yes	weld prep	1	$80.00	$121.00		
2" Ultra-torr fitting	Kurt Lesker	http://www.lesker.com/	$135.00	yes	weld to flange	0.5	$40.00	$175.00		
1.5" NPT to KF40 flange	IdealVac	http://www.idealvac.com/	$126.00	no			$0.00	$126.00		
KF40 - 1/8" NPT - KF40 Tee	IdealVac	http://www.idealvac.com/	$62.00	no			$0.00	$62.00		
KF40 vacuum hose (48")	Kurt Lesker	http://www.lesker.com/	$255.00	no			$0.00	$255.00		
Miscellaneous hardware	McMaster	http://www.mcmaster.com/	$200.00	no			$0.00	$200.00	M8, 5/16-24, 10-32, 4-40, 2-56	
Miscellaneous tubing/fittings	McMaster	http://www.mcmaster.com/	$100.00	no			$0.00	$100.00		
Type HN cable (36")	Pasternack	http://www.pasternack.com/hn-	$119.00	no			$0.00	$119.00		
Type N cable (2x18")	L-com	http://www.l-com.com/productfi	$40.00	no			$0.00	$40.00		
BNC Cables (1x18", 1x36")	L-com	http://www.l-com.com/coaxial-r	$17.00	no			$0.00	$17.00		
RF Capacitor	RF Parts Co.	http://www.rfparts.com/capacito	$28.00	no			$0.00	$28.00		
RF Capacitor housing	McMaster	http://www.mcmaster.com/	$10.00	yes	from stock	1	$80.00	$90.00		
RF fittings (BNC)	Pasternack	http://www.pasternack.com/bnc	$16.00	no			$0.00	$16.00		
RF-shielded thermocouple	Watlow	http://www.watlow.com/	$95.00	no			$0.00	$95.00		
Low pass filter (for DC bias)	Mini-Circuits	http://www.minicircuits.com/	$35.00	no			$0.00	$35.00		
Voltmeter	Digikey	http://www.digikey.com/	$50.00	no			$0.00	$50.00		
Helium regulator and vent valves	Omega	http://www.omega.com/	$150.00	no			$0.00	$150.00		
			$2,832.00 Total Raw Materials/Parts Cost				**$3,440.00** Total Customi	**$6,272.00** Total Chamber Cost		**$6,272.00** Total Chamber Cost
N2 MFC (MC-100SCCM-D)	Alicat	http://www.alicat.com/products	$1,260.00	no			$0.00	$1,260.00	*not in the original system, but necessary in a commercial system*	
O2 MFC (MC-100SCCM-D)	Alicat	http://www.alicat.com/products	$1,260.00	no			$0.00	$1,260.00		
SF6 MFC (MC-100SCCM-D)	Alicat	http://www.alicat.com/products	$1,260.00	no			$0.00	$1,260.00		
C4F8 MFC (MCS-100SCCM-D)	Alicat	http://www.alicat.com/products	$1,710.00	no			$0.00	$1,710.00		
600W Coil RF Generator (CX600-AS)	Comdel	http://comdel.com/cx-series-hi	$5,600.00	no			$0.00	$5,600.00		
300W Chuck RF Generator (R301)	Seren IPS	http://www.serenips.com/R301	$3,600.00	no			$0.00	$3,600.00		
600W Automatic Matching Network	T&C Power Con	http://www.tcpowerconversion.c	$2,800.00					$2,800.00		
600W Automatic Matching Network	T&C Power Con	http://www.tcpowerconversion.c	$2,800.00					$2,800.00		
Pneumatic valve	Lesker	http://www.lesker.com/	$450.00	no			$0.00	$450.00		
Thermocouple gauges and readouts (2x)	Lesker	http://www.lesker.com/	$600.00	no			$0.00	$600.00		
Butterfly control valve (MKS 253B)	MKS	http://www.mksinst.com/	$1,800.00	no			$0.00	$1,800.00		
Control circuitry	various, mostly Newark		$250.00	yes	assembly	3	$240.00	$490.00		
Pump Option A: Turbo + Rotary Vane										
Turbo pump (Pfeiffer HiPace 80)	Pfeiffer	http://www.pfeiffer-vacuum.com	$3,200.00				$0.00	$3,200.00		
Rotary vane pump (Leybold D30A)	IVS	http://www.ivsonline.com/	$2,000.00	no			$0.00	$2,000.00		
PFPE oil	IVS	http://www.ivsonline.com/	$2,000.00	no			$0.00	$2,000.00		
Pump Option B: Turbo + Diaphragm										
Turbo pump station (Pfeiffer HiCube 80)	Pfeiffer	http://www.pfeiffer-vacuum.com	$5,000.00	no			$0.00	$5,000.00		

$30,830.00
Total Peripheral Cost (with Pump Option A)

$28,630.00
Total Peripheral Cost (with Pump Option B)

$37,102.00
Total Everything Cost (with Pump Option A)

$34,902.00
Total Everything Cost (with Pump Option B)

Current System Cost
$31,562.00

	Added Cost	% Increase	Peripheral % of cost
with Pump Option A	$3,340.00	10.58%	83.10%
with Pump Option B	$5,540.00	17.55%	82.03%

System cost changes in noted in green

This sheet contains the price to build a new system with the improvements described in Chapter 5 of the thesis

Appendix B: Gas Flow Equations

The following equations were used during the course of the analysis of the gas distribution system (**Section 3.1.5**). They are taken from the chapter entitled "Flow of Gases Through Tubes and Orifices" by R. G. Livesey from Foundations of Vacuum Science and Technology, edited by J. M. Lafferty.

Knudsen Number (Kn):

Equation	Where:
$$Kn = \frac{\lambda}{d_c} = \frac{\eta}{Pd_c}\sqrt{\frac{\pi R_0 T}{2M_m}}$$	λ = mean free path d_c = characteristic dimension η = viscosity R_0 = ideal gas constant T = temperature M_m = relative molar mass

Gas Factor (used as a correction factor for formulas based on air) (F_g):

Equation	Where:
$$F_g = \frac{\lambda_{air}}{\lambda_{gas}} = \frac{\eta_{air}}{\eta_{gas}}\sqrt{\frac{M_{gas}}{M_{air}}}$$	λ = mean free path η = viscosity M_m = relative molar mass

Throughput (volumetric flow rate at a certain pressure) ($\dot{Q}$):

Equation	Where:
$$\dot{Q} = P\frac{dV}{dt} = C \cdot P_{drop}$$	P = pressure V = volume C = conductance P_{drop} = pressure drop

Reynolds number (used to assess viscous flow laminarity) (Re):

Equation	Where:
$$Re = \frac{\rho u D_h}{\eta} = \frac{4\rho u A}{\eta B}$$	ρ = density u = flow velocity D_h = hydraulic diameter η = viscosity A = cross-sectional area B = perimeter of cross section

Molecular conductance formulas

Molecular flow conductance of an aperture ($C_{m,a}$):

$$C_{m,a} = A\sqrt{\frac{R_O T}{2\pi M_m}}$$	**Where:** A = aperture area R_0 = ideal gas constant T = temperature M_m = relative molar mass

Molecular flow conductance of a long ($l > 50d$) circular duct ($C_{m,l}$):

$$C_{m,l} = C_{m,a}\frac{4d}{3l} = \frac{d^3}{3l}\sqrt{\frac{\pi R_O T}{2M_m}}$$	**Where:** d = duct diameter l = duct length R_0 = ideal gas constant T = temperature M_m = relative molar mass

Molecular flow conductance of a short circular duct ($C_{m,s}$):

$$C_{m,s} = C_{m,a}\alpha_{m,s} = \frac{\pi d^2}{4}\sqrt{\frac{R_O T}{2\pi M_m}}\left(\frac{28d^2 + 8ld}{28d^2 + 36ld + 6l^2}\right)$$	**Where:** d = duct diameter l = duct length R_0 = ideal gas constant T = temperature M_m = relative molar mass

Molecular flow conductance of an annulus ($C_{m,ann}$):

$$C_{m,ann} = C_{m,a}\alpha_{m,ann} = \frac{\pi}{4}(d_2^2 - d_1^2)\sqrt{\frac{R_O T}{2\pi M_m}}\alpha_{m,ann}$$ $$\alpha_{m,ann} = \left(\frac{d_2 - d_1}{d_2 - d_1 + l - 2lu\left(\tan^{-1}\left(\frac{2l}{v(d_2 - d_1)}\right)\right)}\right)$$ $$u = \frac{-0.037d_1^2 - 0.014d_1 d_2 + 0.0741d_2^2}{0.05d_1^2 - 0.918d_1 d_2 + d_2^2}$$ $$v = \frac{-1.45d_1^2 - 2.86d_1 d_2 + 5.825d_2^2}{-1.28d_1^2 + 0.56d_1 d_2 + d_2^2}$$	**Where:** d_2 = outer diameter d_1 = inner diameter l = duct length R_0 = ideal gas constant T = temperature M_m = relative molar mass

Viscous (laminar) conductance formulas

Viscous flow conductance of a long circular duct ($C_{v,l}$):

$$C_{v,l} = \frac{\pi d^4}{128 \eta l} \bar{P}$$	**Where:** d = duct diameter l = duct length η = viscosity $\bar{P}$ = average pressure across duct

Viscous flow conductance of an annulus ($C_{v,ann}$):

$$C_{v,ann} = \frac{\pi}{128 \eta l} \bar{P} \left(d_2^4 - d_1^4 - \frac{(d_2^2 - d_1^2)^2}{\ln(d_2/d_1)} \right)$$	**Where:** d_2 = outer diameter d_1 = inner diameter l = duct length η = viscosity $\bar{P}$ = average pressure across duct

Viscous flow long duct criterion for circular cross-sections (basically, how to decide what counts as a "long" tube):

$$length = l > \frac{20 Re \cdot d}{64}$$	**Where:** l = duct length Re = Reynolds number d = duct diameter

For the very small Reynolds numbers encountered in the 1" Fab DRIE, the long duct criterion basically says that if the length of the duct is near its diameter, it can be treated as a long duct.

Transitional conductance formulas

Transitional flow conductance [empirical] of a long circular duct ($C_{t,l}$):

	Where:
$$C_{t,l} = C_{m,l}\left(1.485\bar{P}dF_g + \frac{1+25.277\bar{P}dF_g}{1+31.217\bar{P}dF_g}\right)$$	$C_{m,l}$ = molecular long tube conductance $\bar{P}$ = average pressure across duct [Torr] d = duct diameter [mm] F_g = gas factor

Transitional flow conductance [empirical] of an aperture ($C_{t,a}$):

	Where:
$$C_{t,a} = C_{m,a}\left(\left(\frac{k_sKn}{k_sKn+1}\right) + \left(1 - \frac{k_sKn}{k_sKn+1}\right)\sqrt{\frac{4\pi}{K_p - 1}}\right)$$	$C_{m,a}$ = molecular aperture conductance k_s = fitting factor (~12 for air) Kn = Knudsen number K_p = ratio of higher pressure to lower pressure (i.e. upstream to downstream)

Transitional flow long duct criterion for circular cross-sections (basically, how to decide what counts as a "long" tube):

	Where:
$$length = l > \frac{Re \cdot d}{64}\left(1 + \frac{\gamma(\gamma+1)}{2}\right)$$	l = duct length Re = Reynolds number d = duct diameter γ = ratio of the principle specific heats of a gas (~1.1 for polyatomic gases like SF_6)

Like the viscous case, for the very small Reynolds numbers encountered in the 1" Fab DRIE, this long duct criterion basically says that if the length of the duct is near its diameter, it can be treated as a long duct.

Appendix C: 1" Fab DRIE Operation Protocol

The following is the SOP for running a process on the 1" Fab DRIE system starting from the system in a completely shut down state.

1. Turn on the roughing pump and allow it to run for ~15 minutes to warm up. (Note: rotary vane pumps are made to operate continuously for months at a time, so this is a very rare step).
2. Open the valves of each process gas cylinder.
3. Adjust the regulator to ~20 psig. (Note: this is rarely necessary, as the regulators are never intentionally adjusted away from this pressure).
4. Open the valves on the chilled water and chilled water return lines.
5. Turn on the breaker switches for the ICP coil RF generator and the substrate chuck RF generator.
6. Turn on the power switch for the ICP coil matching network.
7. Turn on the shared power switch for the MFCs, gas manifolds, and the vacuum isolation switch.
8. Switch on the control circuitry (make sure the USB cable is plugged in).
9. Start the ERAC Software from the desktop computer. The RF Generators should transition into remote control mode (can be confirmed on the front panel of each generator).
10. Remove the upper chamber assembly and carefully place it to the side.
11. If the alumina wafer clamp is attached to the chuck, unscrew it and set it aside.
12. Apply a small dollop of thermal grease to bottom side of the substrate to be processed.
13. Load the wafer onto the recess at the top of the chuck assembly. Check to make sure the wafer is fully seated in the recess.
14. Replace the alumina wafer clamp by tightening the 2 PTFE screws.
15. Move the chuck to the desired height by slightly loosening the 2" compression fitting on the lower chamber assembly. Retighten the compression fitting AND the backup hose-clamp.

16. Replace the upper chamber assembly. Confirm that the o-ring sealing surfaces are aligned before pumping down.
17. Make sure the upper chamber vent valve is closed. If not, close this valve.
18. Turn on the vacuum switch to begin pumping down.
19. Wait until the chamber pressure falls below 15mTorr before beginning any processing.
20. Load the process you wish to run into the ERAC software. Selecting this process in the Operation tab will begin the process gas flows, but the RF generators will remain off until "Start" is clicked.
21. Wait 1-2 minutes to allow the pressure to stabilize with the process gases flowing.
22. Click "Start" to begin the process.
23. Confirm that the manual matching network is reading a SWR of <1.1. If not, adjust the tuning knobs until the SWR falls below 1.1.
24. Cross your fingers and wait for the process to complete. The ERAC indicates the remaining time.
25. After the purge sequence completes, vent the chamber using the vent valve on the upper chamber assembly.
26. Remove the upper chamber assembly and carefully place it to the side.
27. Undo the alumina wafer clamp and remove the processed wafer. Clean any excess thermal grease.
28. Replace the alumina wafer clamp by tightening the 2 PTFE screws.
29. Replace the upper chamber assembly. Confirm that the o-ring sealing surfaces are aligned before re-pumping down the system.
30. Turn on the vacuum valve to begin pumping down the chamber. (It is a good practice to leave the chamber under vacuum when not in use.)
31. Close the ERAC software.
32. Perform Steps 4-8 in reverse, closing and shutting off each component.
33. Close the process gas cylinder valves.
34. If (and only if) the system will not be used for an extended period, turn off the roughing pump.

Appendix D: Control System Circuit Diagram

The current iteration of the 1" Fab DRIE has a serial port assigned to Alicat #1-#3 (ALC1-3), the Comdel (CDL), and the ENI (ENI).
The Clippard valves (CV) in the gas manifold are controlled by I/O pins.

Released under the Creative Commons
Attribution Share-Alike 3.0 License
http://creativecommons.org/licenses/by-sa/3.0

TITLE: full_RS_232_controller

Design by: P. Gould

REV: B

Date: not saved!

Sheet: 1/1

Appendix E: Langmuir Probe Theory and Analysis

Langmuir probes (LP) can be used to measure a variety of plasma characteristics such as electron temperature, plasma potential, and plasma density. The simplest Langmuir probe is a shielded wire with a small portion of the conductor (the "probe tip") exposed to the plasma. By sweeping the voltage on the probe tip, the interactions between the probe and the electrons and ions within the plasma change according to the voltage induced on the probe. These changes can be measured by monitoring the induced current in the probe. The resulting LP probe data comes in the form of an I-V curve as shown in the plot below. Different regions of the curve yields different information about the plasma discharge.

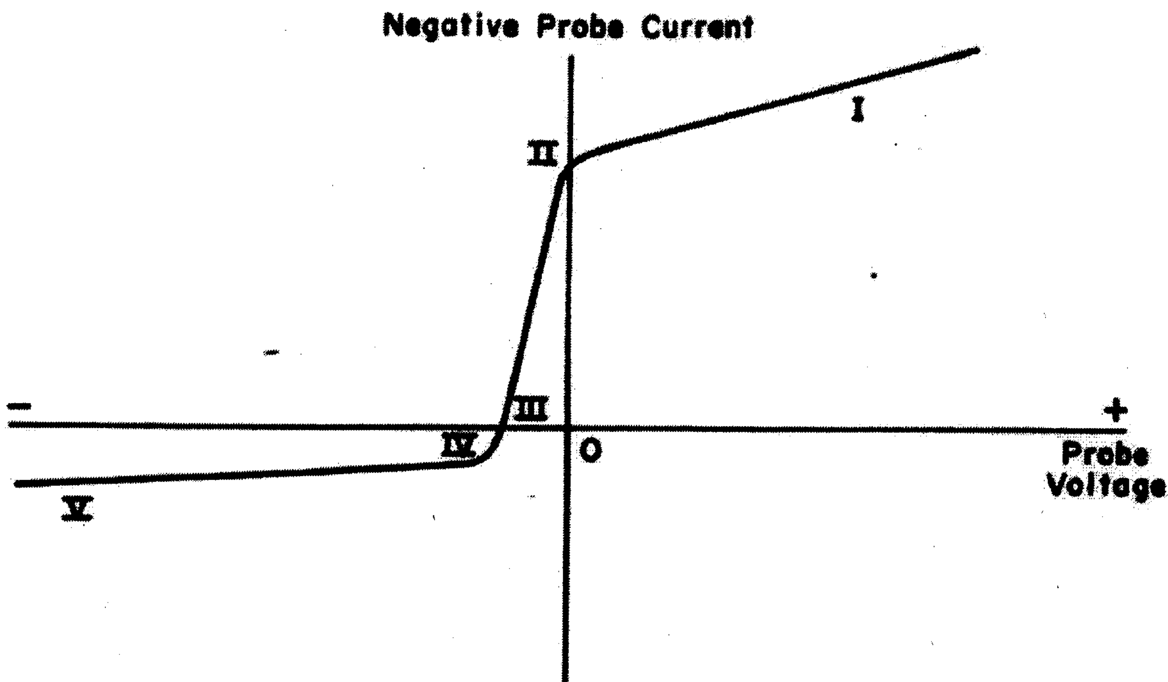

Fig. B I-V Trace For A Typical Plasma

Graph courtesy UC-Irvine Physics Dept. [https://www.physics.uci.edu/~advanlab/plasma.pdf]

In this LP analysis, $i_{electron}$ are defined as positive currents and i_{Ion} are defined as negative currents. There are 5 regions of the LP I-V curve which yield particular information about the plasma. These regions, labeled in Roman numerals in the above plot are referred to as follows: (I) Electron Saturation, (II) Knee Region, (III) Floating Point Potential, (IV) Transition Region, and (V) Ion Saturation Region. The probe voltage decreases as Regions (I) – (V) are traversed, with the changes in probe current reflecting the changes in the plasma characteristics. In the electron saturation region (I) the probe voltage is highly positive causing ions to get repelled from the probe creating a negative sheath around the probe. In this region, only electrons penetrate the sheath to contribute to the probe current. As the probe voltage is decreased, the knee region (II) is reached. In the knee region, the high energy ions start to overcome the sheath and probe current is decreased.

As the probe voltage is further decreased, the floating point potential (III) is reached. Here, an equal number of electrons and ions are transported between the sheath yielding zero net probe current. The floating potential occurs at a negative probe voltage because of the mass difference between electrons and ions. As the probe voltage is reduced again, the transition region (IV) is reached. In this region the probe voltage is negative enough that only the very highest energy electrons (the rightmost side of the Maxwellian distribution of electron energies) are able to pass the sheath, while an increasing number of ions are attracted to the probe tip. For Maxwellian plasmas, like the plasmas in this study, the transition region probe current can be expressed as **Eqn. F.1**. With further reduction of the probe voltage, all electrons are repelled from the probe and ion saturation is reached (V). By analyzing the currents collected in each region, the plasma potential, electron temperature, and plasma density can be calculated.

The most useful quantity determined from collected LP data is the plasma density. This is the data presented in Section 4.1.2 for several plasma types. The plasma density can be calculated from information contained in the ion saturation (V) and transition regions (IV) described above. The electron temperature in the plasma can be determined by fitting region IV of the LP curve to a Maxwellian distribution of velocities of electron energies. The Maxwellian distribution can be written as:

$$i_e = i_{es} Exp\left(\frac{q(V_p - V_s)}{KT_e}\right)$$

where:

$i_{es} = qAn_e\left(\frac{KT_e}{2\pi m}\right)^{\frac{1}{2}}$
T_e: Electron Temperature
A: Probe Tip Area
q: Electron Charge
n_e: Electron Density
m: Mass of electron
V_p: Plasma Potential
V_s: Ion Saturation Voltage
K: Boltzmann Constant

(F.1)

To obtain the electron density from the electron temperatures (T_e) obtained via **Eqn. F.1**, the following process was used:

1) The ion saturation current is subtracted from the LP current measurements. The ion saturation current can be removed by fitting a line to region V of the LP curve and subtracting the extrapolated line from the original data.

2) A linear fit is then approximated to the log of the (ion saturation-corrected) current measurements from region IV. This effectively linearizes **Eqn. F.1**, allowing the electron temperatures to be determined.

3) From the electron temperature, the thermal velocity of the electrons passing through the sheath can be determined using **Eqn. F.2**.

$$v = \left(\frac{KT_e}{M_i}\right)^{\frac{1}{2}}$$

where:
v: Electron Thermal Velocity
M_i: Mass of ion
K: Boltzmann Constant
T_e: Electron Temperature

(F.2)

4) From the thermal velocity, the electron density can be calculated using **Eqn. F.3**.

$$n = \frac{2i}{qvA}$$

where:
n: Electron density
q: Charge of electron
v: Electron velocity (F.2)
i: Electron Saturation Current

(F.3)

The plasma's quasineutrality means that the electron density is the same as the ion density, and therefore this quantity is commonly referred to as the "plasma density".

Appendix F: Full RSM Data Set

Standard Order Test	Actual Run Order	Block	SF_6 [sccm]	O_2 [sccm]	Base Power [W]	% O_2 in Total Flow	SF_6/O_2 Ratio	Process Pressure [mTorr]	Vertical Etch Depth [µm]	Lateral Etch Depth [µm]	Resist Erosion [µm]	Vertical Etch Rate [µm/min]	Lateral Etch Rate [µm/min]	V/L Etch Rate Ratio	Mask Selectivity	APDM (Uniformity)	Etch Profile
1	12	1	1	0.25	5	20.0%	4.00	34	38	17.5	2.0	2.533	1.167	2.171	19.000	0.368%	Isotropic
2	10	1	1	0.75	15	42.9%	1.33	34	43	3.5	3.5	2.867	0.233	12.286	12.286	2.810%	Anisotropic
3	13	1	2	0.25	15	11.1%	8.00	44	58	27.5	1.75	3.867	1.833	2.109	33.143	0.634%	Isotropic
4	14	1	2	0.75	5	27.3%	2.67	43	65	14.0	1.25	4.333	0.933	4.643	52.000	0.524%	Anisotropic
5	11	1	1.5	0.5	10	25.0%	3.00	39	51	26.0	2.0	3.400	1.733	1.962	25.500	0.462%	Isotropic
6	9	1	1.5	0.5	10	25.0%	3.00	40	48	24.5	2.0	3.200	1.633	1.959	24.000	0.428%	Isotropic
7	20	1	1	0.25	15	20.0%	4.00	33	38	15.5	3.0	2.533	1.033	2.452	12.667	0.945%	Isotropic
8	17	1	1	0.75	5	42.9%	1.33	33	43	2.0	3.0	2.867	0.133	21.500	14.333	4.014%	Anisotropic
9	16	1	2	0.25	5	11.1%	8.00	45	58	27.0	1.5	3.867	1.800	2.148	38.667	0.820%	Isotropic
10	19	1	2	0.75	15	27.3%	2.67	47	58	30.5	2.0	3.867	2.033	1.902	29.000	0.462%	Isotropic
11	15	1	1.5	0.5	10	25.0%	3.00	38	51	24.0	2.25	3.400	1.600	2.125	22.667	0.395%	Isotropic
12	18	1	1.5	0.5	10	25.0%	3.00	40	51	27.5	1.75	3.400	1.833	1.855	29.143	0.588%	Isotropic
13	8	2	0.684	0.5	10	42.2%	1.37	28	30	2.5	3.75	2.000	0.167	12.000	8.000	3.854%	Anisotropic
14	4	2	2.317	0.5	10	17.7%	4.63	48	63	31.5	1.5	4.200	2.100	2.000	42.000	0.811%	Isotropic
15	3	2	1.5	0.092	10	5.8%	16.30	35	46	22.0	2.0	3.067	1.467	2.091	23.000	0.461%	Isotropic
16	2	2	1.5	0.908	10	37.7%	1.65	38	51	4.0	2.5	3.400	0.267	12.750	20.400	3.921%	Anisotropic
17	7	2	1.5	0.5	1.8	25.0%	3.00	38	60	6.0	1.0	4.000	0.400	10.000	60.000	0.740%	Anisotropic
18	5	2	1.5	0.5	18.2	25.0%	3.00	41	51	25.0	2.25	3.400	1.667	2.040	22.667	0.700%	Isotropic
19	1	2	1.5	0.5	10	25.0%	3.00	40	52	24.0	2.125	3.467	1.600	2.167	24.471	0.512%	Isotropic
20	6	2	1.5	0.5	10	25.0%	3.00	37	50	24.5	2.0	3.333	1.633	2.041	25.000	0.361%	Isotropic

Factor levels

Quantities calculated based on factor levels

Quantities measured

Quantities calculated from measured values